

## ABSTRACT

Title of Document: DEVELOPMENT AND INVESTIGATION OF A  
FLAPPING ROTOR FOR MICRO AIR VEHICLES

Brandon Fitchett, Master of Science, 2007  
brandonfitchett@hotmail.com

Directed By: Professor/Advisor, Dr. Inderjit Chopra,  
Department of Aerospace Engineering

This thesis describes the concept, design and testing of a micro air vehicle rotor testbed capable of independently controlled blade rotation and powered blade flapping. The design, dubbed the “Flotor”, combined the benefits of a conventional MAV helicopter rotor with avian based flapping motion. The Flotor was tested as a conventional rotor, a conventional rotor with powered blade flapping, and a torqueless, freely rotating rotor with powered blade flapping. As a conventional rotor with a maximum figure of merit of 0.5, the results from the Flotor were similar to previously published experiments. With conventional rotation plus powered blade flapping at up to 8 per rotor revolution at a reduced frequency of 0.6, the maximum thrust increased by up to 15% due to delayed stall. The torque required at moderate thrust levels was reduced by up to 30%. The results from a 2-D quasi-steady blade element momentum analysis predicted average rotor loads accurately below 20° collective. As the first attempt at a torqueless flapping MAV rotor, the Flotor was capable of producing thrust and blade loadings comparable to flying animals, but less than current MAVs.

DEVELOPMENT AND INVESTIGATION OF A FLAPPING ROTOR  
FOR MICRO AIR VEHICLES

By

Brandon K. Fitchett

Thesis submitted to the Faculty of the Graduate School of the  
University of Maryland, College Park, in partial fulfillment  
of the requirements for the degree of  
Master of Science  
2007

Advisory Committee:

Professor Inderjit Chopra, Committee Chair

Professor Daryll Pines, Department Chair

Professor James Baeder, Associate Professor

© Copyright by  
Brandon K. Fitchett  
2007

## Acknowledgements

My research work and classroom experience was possible due the guidance, organization, and support of my advisor, Dr. Inderjit Chopra. His encouragement and direction has been invaluable. It was an honor to learn from him and the other professors from whom I studied. My experimental research also benefited from the insight of my colleagues, who, by sharing their previous experiences, saved countless hours of my own time. Thanks to Dr. Jayant Sirohi, Benjamin Hein, Dr. Felipe Bohorquez, Dr. Beerinder Singh, Jaye Falls, and Dr. V.T. Nagaraj for passing on knowledge and research methods that can only be learned from experience. Thanks to Peter Copp, Vikram Hrishikeshavan, Moble Benedict, Nitin Gupta, Lynn Gravatt, and Beverly Beasely for their help in the lab whenever I needed it. I apologize to my colleagues who I have not mentioned by name, for it does not mean I owe you any less thanks. Much of this work was made possible by the Army Research Office under the MAV MURI Program (ARMYW911NF0410176).

# Table of Contents

Acknowledgements.....	ii
Table of Contents.....	iii
List of Figures.....	v
Nomenclature.....	ix
1 Introduction.....	1
1.1 Definition and Purpose of Micro Air Vehicles.....	1
1.2 State of the Art: Current MAV configurations.....	2
1.2.1 Fixed Wing.....	3
1.2.2 Rotary Wing.....	4
1.2.3 Flapping Wing.....	9
1.3 MAV Challenges.....	12
1.3.1 Low Reynolds Number Aerodynamics.....	13
1.4 Previous Research.....	17
1.4.1 Conventional Micro Rotors.....	18
1.4.2 Biomimetic Movement.....	19
1.4.3 Bio-Inspired Aerodynamics.....	22
1.4.4 Flapping Rotor Concept.....	26
1.5 Current Research Objectives.....	28
1.6 Outline.....	28
2 Concept and Design.....	30
2.1 Advantages.....	30
2.2 Disadvantages.....	31
2.3 Initial Rotor Design and Sizing.....	31
2.3.1 Thrust.....	32
2.3.2 Blades.....	34
2.3.3 Rotational Speed.....	34
2.4 Flapping.....	35
2.5 Design and Fabrication.....	36
2.5.1 Basic Components.....	37
2.5.2 3-D Solid Model and Construction.....	40
3 Analytical Models.....	41
3.1 Kinematics and Mechanics.....	41
3.2 Aerodynamics.....	46
3.2.1 Rotation.....	47
3.2.2 Flapping and Rotation.....	57
4 Experiment, Results, and Discussion.....	60
4.1 Powered Flapping With Free Hub Rotation.....	60
4.2 Conventional Powered Rotation and Model Validation.....	80
4.3 Powered Rotation with Powered Flapping.....	93
5 Summary and Concluding Remarks.....	116
5.1 Contributions and Conclusions.....	117
5.1.1 Flapping blades with passive hub rotation.....	117

5.1.2	Conventional rotation.....	118
5.1.3	Powered hub rotation with powered blade flapping .....	119
5.2	Future Work Recommendations .....	120
	Bibliography .....	123

## List of Figures

Figure 1: Seiko/Epson $\mu$ FR [1].....	1
Figure 2: BAE/Lockheed Martin Microstar MAV .....	3
Figure 3: Aerovironment “Black Widow” .....	4
Figure 4: University of Maryland Micor .....	5
Figure 5: Precision Heli Micron V2.....	6
Figure 6: University of Maryland “Giant” .....	7
Figure 7: University of Maryland “TiShrov” .....	8
Figure 8: iSTAR at rest and transitioning to forward flight.....	9
Figure 9: Aerovironment “Microbat” .....	10
Figure 10: Insect based flapping.....	11
Figure 11: “Mentor” flapping wing vehicle.....	12
Figure 12: Vehicle Mass vs. Reynolds Number .....	14
Figure 13: $C_L$ vs. $\alpha$ and $C_L$ vs. $C_D$ at different Reynolds numbers [23, 24] .....	15
Figure 14: $C_L$ vs. $C_D$ for three airfoils.....	17
Figure 15: Delayed Stall, Rotational Lift, Wake Capture.....	21
Figure 16: Forces and velocities on a plunging airfoil .....	25
Figure 17: NRL delphinopter.....	26
Figure 18: Forces on flapping blade .....	27
Figure 19: Flotor .....	30
Figure 20: Wingspan vs. body mass for various birds and bats [44].....	33
Figure 21: Wingbeat frequency vs. Body mass for birds [51,52].....	35

Figure 22: Rotor and swashplate components .....	38
Figure 23: Rear and side view of linear actuation mechanism .....	39
Figure 24: Front and Top view of swashplate and rotor .....	40
Figure 25: 3-D model of Flotor.....	41
Figure 26: Simplified blade flapping mechanism.....	42
Figure 27: Swashplate displacement.....	45
Figure 28: Swashplate vertical velocity.....	45
Figure 29: Swashplate vertical acceleration .....	46
Figure 30: Blade and blade element distances and velocities [53] .....	47
Figure 31: Blade element angles, vectors, and forces.....	48
Figure 32: Annulus used for momentum theory analysis [53] .....	49
Figure 33: Cambered plate force coefficients at low Reynolds number [18, 37].....	53
Figure 34: Plunging blade section vector analysis.....	58
Figure 35: Flapping rotor with freely rotating hub .....	61
Figure 36: Flapping rigid flat plate blades.....	62
Figure 37: Flapping flat plate blades flexible about their leading edge.....	64
Figure 38: Blade 1 Dimensions.....	65
Figure 39: Hub RPM vs. Flapping Frequency.....	67
Figure 40: Thrust vs. Flapping Frequency for various collectives .....	68
Figure 41: Hub RPM vs. flapping frequency for 15° collective .....	70
Figure 42: Hub speed ratio vs. flapping frequency for 15° collective.....	71
Figure 43: Thrust coefficient vs. flapping frequency at 15° collective .....	72

Figure 44: Thrust coefficient vs. hub RPM at 15° collective .....	72
Figure 45: Torque vs. Time for 32 Hz Flapping.....	73
Figure 46: Hub rotation vs. flapping frequency at different collectives .....	75
Figure 47: Thrust coefficient vs. flapping frequency at different collectives.....	75
Figure 48: blade loading vs. flapping frequency .....	76
Figure 49: Carbon blade with flexible leading edge hinge .....	77
Figure 50: Hub rotation vs. flapping frequency for different collectives .....	78
Figure 51: Blade loading vs. flapping frequency for different collectives .....	79
Figure 52: Thrust coefficient vs. flapping frequency at different collectives.....	80
Figure 53: Rotation motor mounted with hall sensor .....	81
Figure 54: Thrust vs. RPM and approximate 10 Watt electrical power limit.....	83
Figure 55: Electrical Power vs. Thrust for various collectives.....	84
Figure 56: $C_T$ vs. RPM for collectives between 0° and 25°.....	84
Figure 57: Electrical figure of merit vs. RPM for collectives from 0° to 25° .....	85
Figure 58: Cambered plate airfoil with sharpened leading edge .....	87
Figure 59: Mechanical and electrical figure of merit vs $C_T/\sigma$ .....	88
Figure 60: $C_T/\sigma$ vs. collective for different RPMs and prediction.....	90
Figure 61: FM vs. $C_T/\sigma$ for different RPMs and prediction .....	91
Figure 62: $C_T/\sigma$ vs. collective for experimental data.....	92
Figure 63: Blade loading coefficient vs. collective .....	95
Figure 64: Flapping amplitude vs. flapping frequency ratio.....	98
Figure 65: 660 RPM 2/rev flap results.....	100

Figure 66: 1000 RPM 2/rev flap results.....	101
Figure 67: 660 RPM 4/rev flap results.....	103
Figure 68: 1000 RPM 4/rev flap results.....	104
Figure 69: 660 RPM 6/rev flap results.....	106
Figure 70: 1000 RPM 6/rev flap results.....	108
Figure 71: 660 RPM 8/rev flap results.....	110
Figure 72: Lift and drag vs. angle of attack for cambered plate including maximum and minimum values for $\pm 10^\circ$ $\alpha$ variation .....	111
Figure 73: Flotor blade with $5^\circ$ peak to peak flapping .....	114
Figure 74: $C_T/\sigma$ vs. collective (quasi steady prediction for 4/rev flapping) .....	114
Figure 75: Torque vs. collective (quasi-steady prediction for 4/rev flapping) .....	116

## Nomenclature

$C_{l_a}$	lift curve slope
$\dot{m}$	mass flow
$b$	wingspan
$c$	chord
$C$	crank radius of flapping motor
$C_D$	drag coefficient
$C_L$	lift coefficient
$C_P$	power coefficient
$C_T$	thrust coefficient
$D$	drag
$dC_T$	vertical thrust coefficient contribution from rotor annulus
$dD$	drag on a blade element
$dF_R$	resultant force on a blade element
$dF_X$	horizontal force on a blade element (in the plane of rotation)
$dF_Z$	vertical force on a blade element (normal to the plane of rotation)
$dL$	lift on a blade element
$dQ$	torque for a rotor annulus
$dT$	vertical thrust contribution from a rotor annulus
$dy$	width of blade element and rotor annulus
$ea$	elastic axis
$F$	Prandtl inflow correction factor
FM	figure of merit
$k$	reduced frequency
$L$	length of flapping motor connecting rod
$L$	lift
LE	leading edge
$m$	mass
$N$	normal (vertical) force on airfoil
$N_b$	number of rotor blades
$P$	rotor power
$Q$	rotor torque
$r$	ratio of rotor radius ( $Y/R$ )

$R$	rotor radius
$r_0$	root cutout of rotor
Re	Reynolds number
$S$	wing or blade area
$T$	rotor thrust
$U$	resultant airspeed vector on blade element
$U_P$	vertical airspeed of blade element
$U_T$	horizontal airspeed of blade element
$v$	airspeed
$V_\infty$	forward speed of airfoil
$V_{eff}$	resultant airspeed of airfoil
$V_F$	vertical velocity of blade element due to flapping
$v_i$	induced velocity normal to rotor plane
$v_{sw}$	induced swirl velocity in the direction of blade rotation
$X$	vertical position of linear slide
$y$	distance of blade element from rotor center
$\dot{z}(t)$	vertical “heaving” velocity of airfoil
$z(t)$	vertical position of airfoil
$\Omega$	hub rotational speed
$\alpha$	angle of attack
$\beta$	blade flapping angle
$\delta$	flapping motor angular position
$\phi$	angle between blade element airspeed and horizontal plane
$\lambda$	inflow ratio
$\mu$	dynamic viscosity constant
$\theta$	blade collective angle
$\rho$	density
$\sigma$	rotor solidity
$\omega$	flapping frequency and flapping motor angular velocity

# 1 Introduction



**Figure 1: Seiko/Epson  $\mu$ FR [1]**

## 1.1 Definition and Purpose of Micro Air Vehicles

Micro Air Vehicles, or “MAVs”, are small flying vehicles that are six inches or less in size and carry a sensing payload. An example of a cutting edge MAV is seen in Figure 1, the Seiko/Epson “Micro Flying Robot” [1]. MAV development has been driven in recent years primarily by military needs, with the Defense Advanced Research Project Agency (DARPA) providing most of the initial research impetus. In 1996, DARPA put forward its original goals and general definition for an MAV. Dimensionally, the vehicle should be constrained to 15 cm with a weight of about 100 grams. The endurance goal was encouraged to be one hour and the payload should include a camera or other sensing device. Today, however, some vehicles with a weight of 300 grams or more are still considered MAVs. No published MAV design

with a size of six inches or smaller has apparently reached the goal of one hour endurance.

For the military, an MAV can provide stealthy surveillance into a complex and possibly dangerous situation without much risk. Common environments for usage include urban areas and inside buildings or in complex terrain such as hills, mountains or inside caves. For civilian applications, an MAV can examine an environment that is harmful due to structural, chemical, electrical, or other hazardous concerns. An MAV could carry a video camera or an array of other sensors, such as those to sense heat, chemicals, or radioactivity. The goal for portability of MAVs is for one person to be able to carry the entire system. All of the components, including ground based instruments, should be able to be quickly assembled and disassembled and packed into a backpack. It is expected that an MAV should only require one or two people to transport, assemble, and operate.

## 1.2 State of the Art: Current MAV configurations

While there is no perfect MAV for all situations, most of the small flying vehicles being developed can be divided into three categories. Just like full size aircraft, the two most successful configurations are fixed wing and rotary wing. The third configuration, which imbibes nature, is a flapping wing configuration. While functional fixed wing and rotary wing MAVs are numerous and successful, there are only a few experimental flapping wing MAVs that have not been used in the field.

### 1.2.1 Fixed Wing

Fixed wing MAVs have so far been the most successful at achieving the longest endurance and greatest speed and range. They are relatively simple, fast, and efficient compared to other categories of MAVs. The BAE/Lockheed Martin Microstar, seen in Figure 2, is an example of a typical fixed wing MAV. It incorporates a part of its support systems into its structure, such as the patented circuit board that is built as part of the wing [2]. Due to many innovations to save weight, it has an endurance of about 25 minutes and can fly at speeds of 30 kts while carrying a video camera payload.



**Figure 2: BAE/Lockheed Martin Microstar MAV**

The Aerovironment Black Widow, seen in Figure 3, also incorporates its systems and payload within the wing, providing a large wing area to lift its mass of 80 grams. It has an endurance of up to 30 minutes as a result of optimization of its wing planform and cross section, electrical systems, and direct drive motor and propeller. During testing, a larger propeller was found more aerodynamically

efficient when paired with a combination motor and gearbox. The gearbox efficiency, however, is only 81% because of its small size, which negated the increase in efficiency of a larger diameter propeller [3]. These fixed wing craft have constraint on their minimum airspeed, which is not conducive to flying indoors or in confined spaces. Because of their high minimum airspeed, they are not capable of “hover and stare”, “perch and stare”, or tagging and targeting operations.



**Figure 3: Aerovironment “Black Widow”**

### 1.2.2 Rotary Wing

For very low speed and hover capability, rotary wing MAVs are most frequently utilized. Just like full size helicopters, these vehicles use either a single

main rotor with a mechanism for anti-torque or a coaxial configuration. In the MAV realm, coaxial designs appear attractive because of their inherent compactness. Examples of coaxial MAVs are the Seiko Micro Flying Robot and the Micor, developed at the University of Maryland as seen in Figure 4 [4]. The Micor's rotors are counter-rotating with an equal and opposite torque applied to each rotor to lift the vehicle's 150 gram mass. The vehicle is controlled only by the teetering upper rotor. Through innovations in low Reynolds number blade design and optimized drivetrain, the vehicle is able to hover for up to 20 minutes. The disadvantages of this design include aerodynamic interference between the two rotors and mechanical complexity and added weight of a dual rotor system.



**Figure 4: University of Maryland Micor**

Unlike a coaxial design, single main rotor designs require a separate device for anti-torque. Some concepts are basically scaled down conventional helicopters, with a large main rotor and a small tail rotor, such as the radio controlled "Micron" helicopter seen in Figure 5 [5]. The 57 gram Precision Heli Micron V2 has an 8"

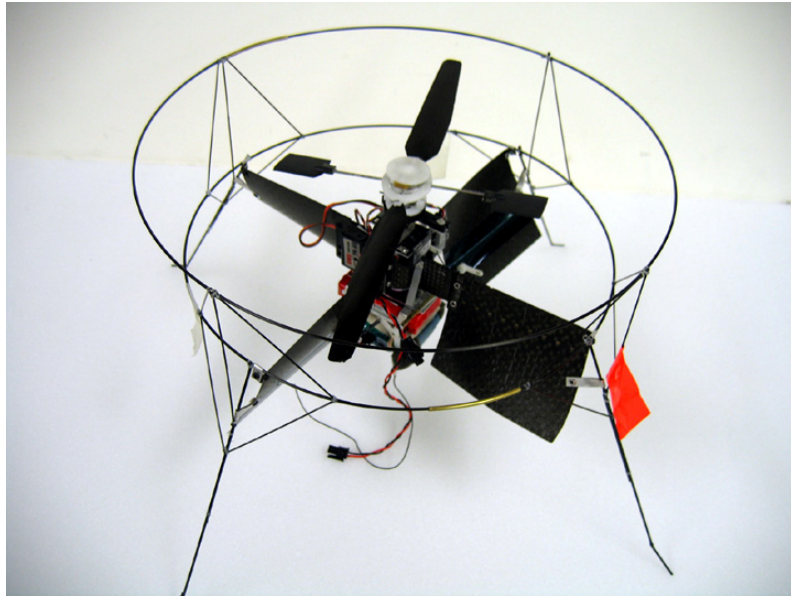
fixed pitch rotor that controls vehicle thrust by varying the rotor RPM and an endurance of about 10 minutes. The benefits of this conventional design are simplicity and familiarity in construction and control. The tail rotor and boom, however, add to the vehicle dimensions and are a detriment to the goal of compactness. Scaling down a conventional helicopter design degrades the efficiency of the vehicle. While the main rotor of a conventional helicopter operates at a figure of merit as high as 0.85, optimized MAV rotors currently operate with a figure of merit of about 0.6 [6].



**Figure 5: Precision Heli Micron V2**

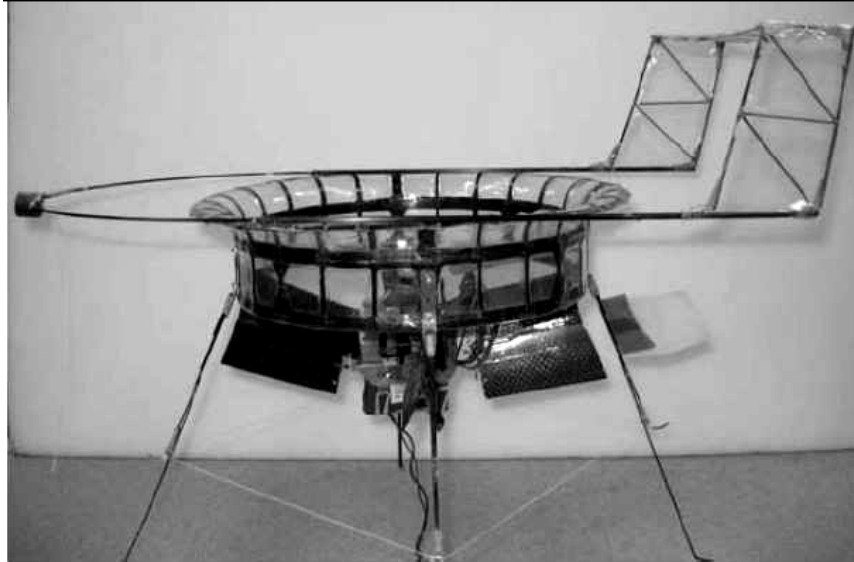
In order to meet the goal of a compact and simple design without the need for two rotors, some MAVs utilize a single rotor with vanes in the downwash to counteract the torque required by the main rotor. As the main rotor torque and thrust increase, the anti-torque from the vanes also increases due to the increased downwash. Three examples of vanes used as a stable method of control and torque counteraction are the Honeywell iSTAR [7] and the Giant and the TiShrov at the University of Maryland [8, 9, 10]. The Giant is seen in Figure 6 and the TiShrov in

Figure 7. The Giant and the TiShrov are similar vehicles, but the TiShrov utilizes a shrouded rotor. The shroud has a curved inlet that increases aerodynamic efficiency by reducing tip losses and providing additional thrust due to the accelerated airflow over the inlet. The thrust benefits of the shroud have not yet exceeded the shroud's weight, so the unshrouded Giant has a greater endurance of about 8 minutes.



**Figure 6: University of Maryland “Giant”**

The Giant incorporates a fixed pitch rotor with a diameter of 135 cm and a Hiller stabilizer bar for control. Two of its vanes have articulated flaps to trim the vehicle with anti-torque and provide yaw control. The vanes on the Giant and TiShrov have been tested to consume approximately 10% of the vehicle's power, which is comparable to the tail rotor on a full scale helicopter. The disadvantage of the current design of the Giant's vanes and the TiShrov's shroud is that they cause more drag than a conventional rotor.



**Figure 7: University of Maryland “TiShrov”**

The Honeywell/Allied Aerospace iSTAR is seen in Figure 8. Like the TiShrov, the iSTAR uses a shroud and vanes in the downwash of its single main rotor to counteract the rotor torque and also for pitch and yaw control. At most, the iSTAR has been tested with a 29” rotor and duct to increase payload and endurance. While most rotary wing MAVs can only be operated at slow speeds and minimal wind, the iSTAR design has the capability to transition to high speed forward flight. The vehicle can tilt almost 90° and gain horizontal airspeed so that its rotor acts like a ducted propeller and the duct acts as a circular wing to provide lift. In order to achieve the amount of control authority necessary to pitch the vehicle for horizontal axial flight, the vehicle has a high vertical center of gravity. The vehicles engine can be seen in Figure 8 mounted above the main rotor to raise the center of gravity. The high center of gravity leads to a difficulty in pitch control, especially at intermediate forward flight speeds [11]. The vehicle also has a high profile drag from its shroud

and a loud noise signature from its piston engine.



**Figure 8: iSTAR at rest and transitioning to forward flight**

### 1.2.3 Flapping Wing

In addition to the fixed wing and rotary wing designs for MAVs, there are also some unconventional designs that utilize flapping wings to generate lift and propulsion. Most of these concepts are based upon nature and simulate the motions of the wings of flying creatures. The two basic types of flapping motion found in nature are avian based and insect based. In pure avian based flapping, the wings stroke in a nearly vertical plane with respect to the body frame. The wing of a bird is intricately woven with muscles for controlling the pitch, camber, and sweep of the wing as well as controlling the orientation of individual feathers depending on the flight condition. In this regard, the performance of avian flight is extremely reliant on active morphing for maximum flight efficiency. For most birds and avian based flight vehicles, hovering is not possible. They usually depend on a forward airspeed to generate lift and utilize flapping to produce a forward thrust. The Aerovironment

Microbat, seen in Figure 9, is only one example of an MAV whose flapping motion is based upon avian flight [12]. The wings of the Microbat do not actively change shape, however. They change shape passively due to inertial and aerodynamic forces. The wings flap simply in a vertical plane to produce thrust and lift. Like most birds of its size, the Microbat requires a horizontal velocity to fly and it cannot hover.

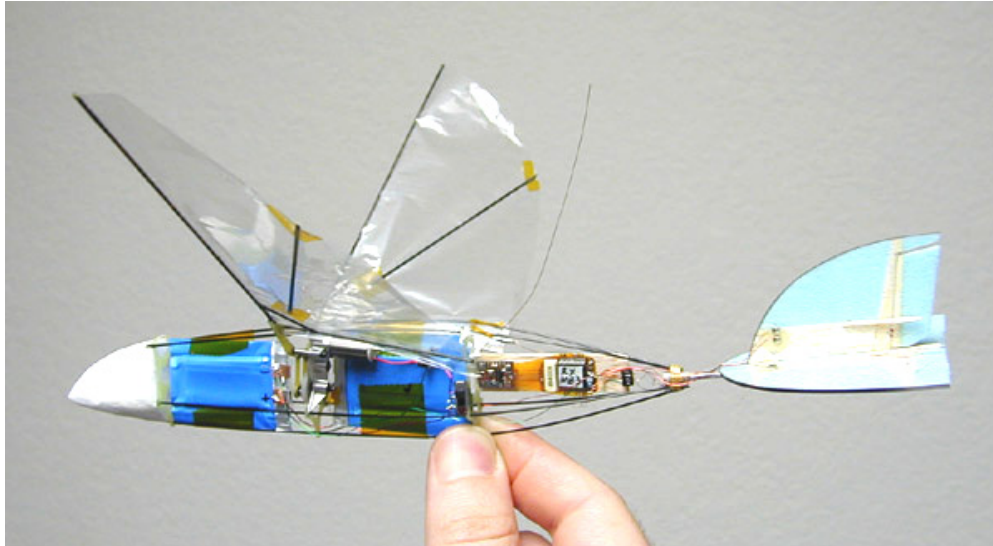


**Figure 9: Aerovironment “Microbat”**

In hover capable insect based flapping, the stroke plane is nearly horizontal, with the wing changing direction with respect to the flowfield from the upstroke to the downstroke, as seen in Figure 10 [13]. The wing pronates and supinates, or inverts, each time it changes directions. The wings create their own freestream velocities and their net force averages to a vertical force during hover when the stroke plane is horizontal. In forward flight, the stroke plane tilts forward, which tilts the net thrust vector forward. Like avian based flapping, the wings change shape depending on flow conditions. Unlike avian based flapping, however, changes in the wing shape occur purely passively due to aeroelastic coupling of inertial and aerodynamic forces.

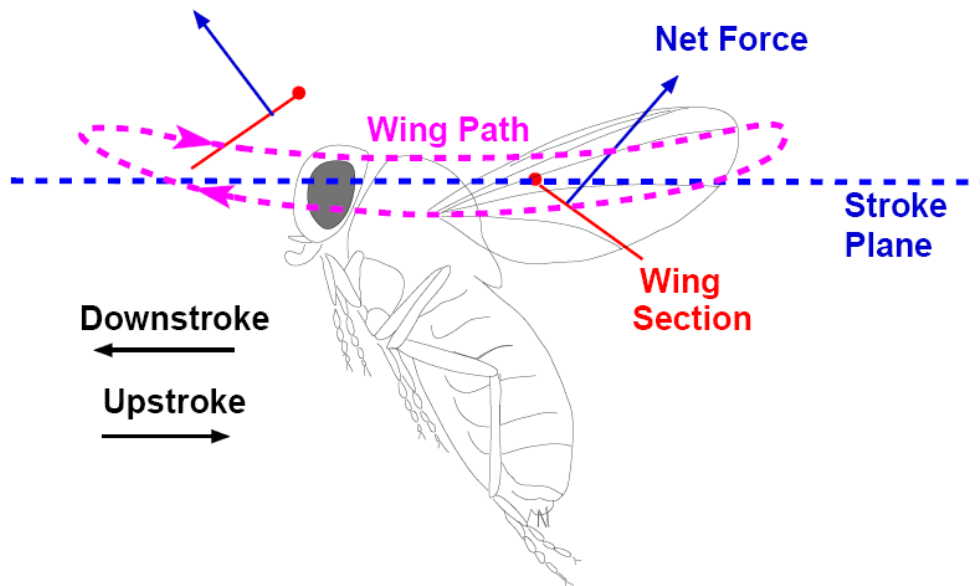


**Figure 10: Insect based flapping**

The Mentor [14], seen in Figure 11, fits the description of insect based flight. With a wingspan of 12” and an endurance of about 10 minutes, it was the first small flapping wing vehicle capable of hovering and transitioning into forward flight. The four wings flap in a horizontal stroke plane and use the “clap-fling” phenomenon presented by Weis-fogh [15]. Clap-fling occurs on the Mentor when the wings are forced together and their leading edges make contact first. The flexible wing membranes squeeze the air in between them, forming an area of high pressure which generates lift. The flexible wings allow the higher pressure air to escape downwards as they clap together. When the wings are pulled apart, the flexible membranes again lag the motion of the stiffer leading edge, forming an area of low pressure on their upper surface. This low pressure region creates lift and also pulls air downwards, generating momentum flow. The negative effects of this configuration include short endurance and a loud noise signature and material fatigue due to the high speed

clapping of the wings. None of the flapping wing MAVs have been successful at achieving the endurance and range of current fixed wing or rotary wing designs.



**Figure 11: “Mentor” flapping wing vehicle**

### 1.3 MAV Challenges

During the past decade, electronic components have become more miniaturized and lightweight. Only recently have they become feasible for MAV use. Even with these recent advancements, no published MAV with a size of six inches or less has reached the endurance goal of one hour sustained flight. One cause of the endurance shortfall is the weight of the payload and electronics for navigation and control. As electronics and MEMS technologies are further miniaturized, MAV payloads will be manufactured lighter, allowing higher performance, reduced size, or increased endurance. Another cause for short endurance is the size and efficiency of the power source and motor. While large electric motors have efficiencies greater than 90%, MAV sized motors have efficiencies on the order of 60% or less, which limit performance [3]. As the motor efficiency and the battery specific energy and

specific power increase, there will be an improvement in endurance. Also to improve endurance, there is an opportunity to optimize the aerodynamic design of MAVs for operation in a low Reynolds number regime. Many of the aerodynamic theories and assumptions applied to full scale aircraft, such as turbulent boundary layers and steady, attached flows, may no longer be valid as the scale of flying vehicles becomes small.

### 1.3.1 Low Reynolds Number Aerodynamics

A defining characteristic of low Reynolds number aerodynamics is laminar flow. As the thrusting and lifting surfaces of a flying vehicle become smaller, they become inherently less efficient. Compared to the pressure forces and inertial forces on the vehicle, the relative fluidic viscous forces become greater as the vehicle size decreases. The ratio of vehicle inertial forces to viscous forces is commonly expressed in terms of Reynolds number. Reynolds number is calculated in terms of fluid density ( $\rho$ ), free-stream velocity ( $v$ ), a reference length of the object ( $L$ ), which is usually chord length of a wing, and a dynamic viscosity constant of the fluid ( $\mu$ ):

$$\text{Re} = \frac{\rho v L}{\mu} = \frac{\text{Inertial force}}{\text{Viscous force}}$$

As seen in Figure 12, the Reynolds Numbers for MAVs can be on the order of 10,000 or even lower [4]. Many previous experiments have shown that airfoils optimized for full scale aircraft and helicopters perform poorly at MAV Reynolds numbers. The detrimental effects of low Reynolds numbers include reduced maximum lift coefficients and increased drag coefficients due to laminar flows and

flow separation. These effects have been measured in wind tunnel experiments by Laitone [16], Schmitz [17], Sunada et al [18], Selig et al [19], Mueller [20, 21] and many others.

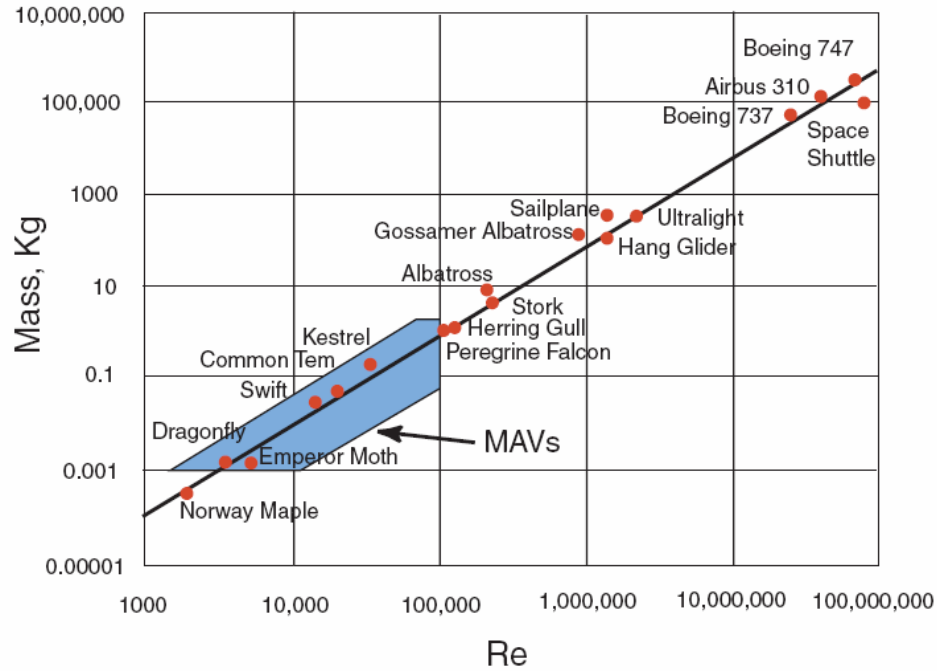


**Figure 12: Vehicle Mass vs. Reynolds Number**

The results show when moving from Reynolds numbers on the order of  $10^6$  down to Reynolds numbers of 20,000 and below, the maximum lift coefficients of conventional airfoils can be reduced by a factor of two. Not only does the lift performance degrade, but the drag coefficients are many times higher. This causes maximum lift to drag ratios of conventional airfoils at low Reynolds numbers to be an order of magnitude less than their values at higher Reynolds numbers. Increased profile drag and induced drag are both responsible for increased drag at low Reynolds numbers. Due to these effects, an MAV rotor requires a profile power that is 50% higher than a full scale helicopter rotor and suffers from lift to drag ratios ranging

from about 2 to 8 [22].

Figure 13 shows well known airfoil data in the form of  $C_L$  vs.  $\alpha$  and  $C_D$  vs.  $\alpha$  for a NACA 4412 airfoil that produces very high lift to drag ratios at full scale [23, 24]. It is obvious that, at Reynolds numbers of 20,000, the performance of this airfoil is drastically different from its behavior at higher Reynolds numbers. The lift to drag ratio is about 100 at Reynolds numbers of  $3 \times 10^6$ , but falls to about 5 at a Reynolds number of 20,000. This is a typical MAV lift to drag ratio and it causes one of the biggest challenges of applying conventional lift and propulsion methods to MAVs.

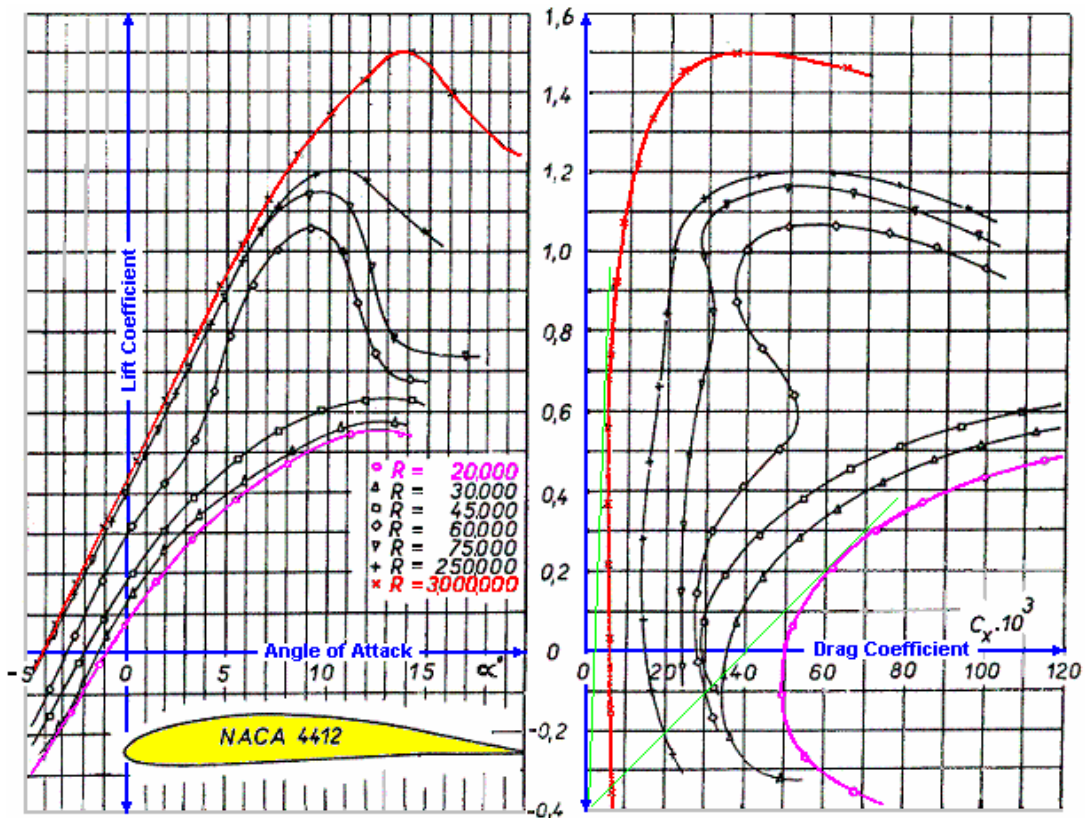
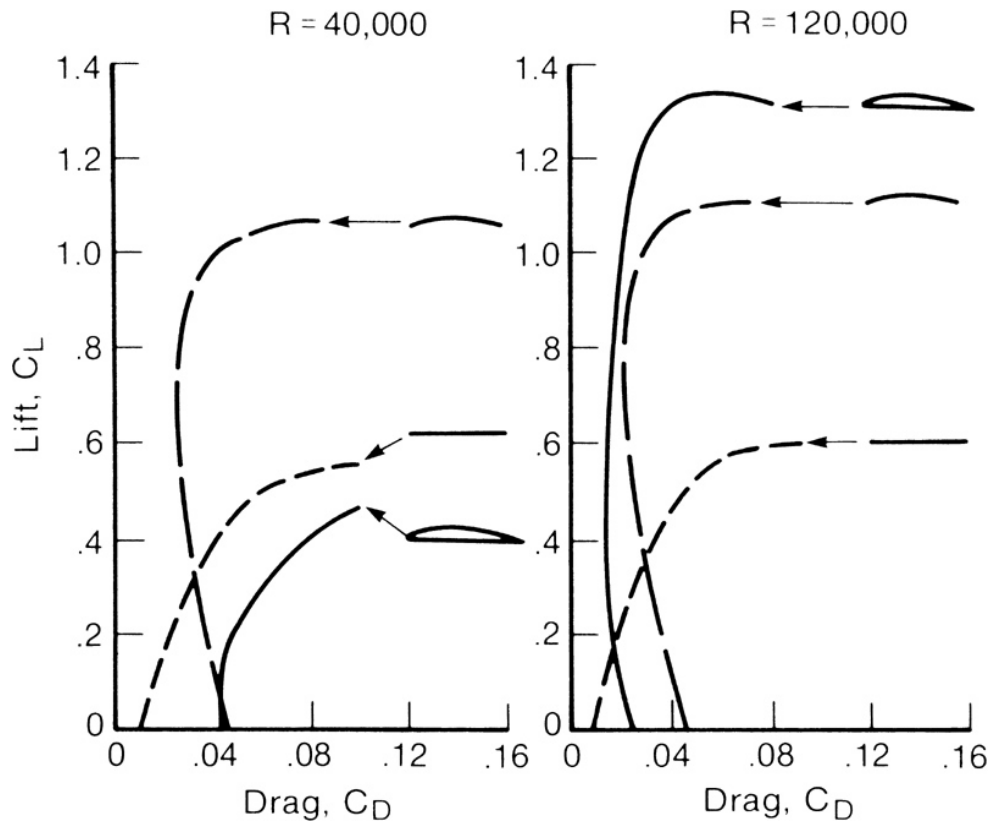


Figure 13:  $C_L$  vs.  $\alpha$  and  $C_L$  vs.  $C_D$  at different Reynolds numbers [23, 24]

Similar Reynolds number effects were found by Schmitz [17], who performed

many tests of common airfoils at Reynolds numbers ranging from 20,000 to 160,000. It was found that, decreasing through this Reynolds number range, maximum lift coefficients can fall by a factor of more than two and minimum drag coefficients can double. A “critical Reynolds number” was identified, which is on the order of 60,000 to 100,000, depending on the airfoil. Above this critical Reynolds number, the flow over the airfoil was found turbulent and the skin friction drag was relatively low. There was laminar flow below the critical Reynolds number, which reduced maximum lift coefficients and increased skin friction drag dramatically. Formulas were presented to predict how drag coefficients increase and lift coefficients decrease as Reynolds number decreases.

Researchers have found that the lift curves of flat plates are relatively unaffected by low Reynolds numbers. While conventional airfoils outperform thin flat plates at high Reynolds numbers, the plates do not suffer the two or threefold reduction in maximum lift coefficients below their critical Reynolds number. Figure 14 shows the lift vs. drag performance of a conventional airfoil, a flat plate, and a cambered plate above and below the critical Reynolds number [25]. At low Reynolds numbers, conventional airfoils will have laminar flow along their surface, which separates readily and stalls the airfoil at low angles of attack. The abrupt and sometimes sharpened leading edge of a flat or curved arc airfoil acts as a boundary layer trip, causing the flow to become turbulent once it passes the leading edge of the airfoil. Even with laminar flow, the lifting performance of flat plate airfoils is not significantly affected by passing below the critical Reynolds number. This is the reason that many current MAVs utilize curved plates or membrane wings.



**Figure 14:  $C_L$  vs.  $C_D$  for three airfoils at Reynolds numbers of 40,000 and 120,000 [25]**

#### 1.4 Previous Research

Whether applying low Reynolds number airfoil designs to small helicopter rotors or studying phenomena from nature for lift and propulsion, the previous research presented had a common goal of optimizing and understanding small scale flight. The nature based research fits into two categories. The first category is “biomimetic”, which means imitating the motions and planforms found in nature. The second category is “bio-inspired” and it usually utilizes oscillating wings in a slightly different manner than in nature.

### 1.4.1 Conventional Micro Rotors

It is now well established that optimal designs for conventional airfoils for full scale aircraft are not optimal designs for MAVs. Recent research into micro rotor performance has verified past findings of low Reynolds numbers airfoil designs, which show that the performance of thin cambered plates exceeds that of conventional airfoils at low Reynolds numbers [16, 17, 19]. With a decrease in Reynolds numbers, the lift coefficients of thin plates are relatively unchanged, while the lift capability of conventional airfoils is reduced significantly.

At the University of Maryland, there has been much research accomplished on aerodynamic performance improvements and optimization of airfoils and blade planforms for MAV rotors. Bohorquez and Pines [4] studied effects of rotor solidity, airfoil selection, blade twist and planform shape on MAV rotor efficiency while using simple and consistent manufacturing methods. The study began with an 8.8” diameter two-bladed rotor from a flying MAV spun at speeds between 1333 and 3500 RPM, which resulted in tip Reynolds numbers on the order of 20,000 - 40,000. The first blades tested were rectangular flat plates and resulted in a figure of merit of 0.35. Through experimental improvements of the blade design, the final micro rotor had a figure of merit up to 0.65. The experimentally optimized blades incorporated a linear asymmetric taper ratio of 2:1 starting at 60% of the rotor radius and gave the rotor a solidity of 0.12. The final airfoils used were 2.5% thick plates cambered by 9%, which is a drastic change from the 10-12% thick airfoils commonly used on full scale helicopters.

Hein and Chopra [26] also focused on improving micro rotor performance at low Reynolds numbers. They studied different blade planforms, twist distributions, and airfoil shapes on a 6" diameter MAV rotor with tip Reynolds numbers between 25,000 and 40,000. The rotor performance was improved by increasing the solidity above that of full scale rotors to a thrust weighted solidity of 0.16. It was found that rotor efficiency was only marginally improved with moderate amounts of blade twist or taper. The focus shifted to improving the airfoil shapes used in rotary wing MAV blades. A 2.75% thin rectangular plate cambered 7% with a sharpened leading edge provided far superior results to conventional airfoils at this scale. Using this blade, the test rotor achieved a figure of merit of 0.55, which, while outstanding for low Reynolds numbers, is not close to matching the efficiency of full scale rotors. Flow visualization showed large tip vortices, a very non uniform inflow, including a blocked flow near the blade roots, and higher induced velocities near the blade tips compared to full scale rotors.

## 1.4.2 Biomimetic Movement

When conventional steady aerodynamic analysis is applied to the wings of a bumblebee, the results show that the bumblebee wings cannot lift its weight. In order for the flight of many animals to be possible, they achieve greater lift coefficients than can be explained by conventional steady aerodynamics. Some researchers are concentrating on the aerodynamics and exact wing motions of animal flight. Through examinations of live insects in flight, Ellington [27, 28] and Dickinson [29] have carefully studied the kinematics of the creatures and observed the different

aerodynamic techniques used in nature to achieve high vertical lift despite low Reynolds numbers.

The simplest and most common phenomena used by all hovering creatures are delayed stall, rotational lift, and wake capture. A diagram from Dickinson [30] in Figure 15 shows how these three aerodynamic mechanisms are used together in insect flight. The black line segment represents a wing section. The red arrows show the wing motion and the black curved arrows show the motion of the air around the wing. The blue arrows show the resultant force on the wing section, which includes lift and drag. This figure shows the motion of a simple flat wing section moving from right to left in steps 1-3 and then reversing direction and moving from left to right in steps 4 and 5. In step 1, when the wing first starts translating at a high angle of attack, the wing does not stall. Instead, the pressure above the wing remains low due to the leading edge vortex. Lower pressure at the tips causes spanwise flow that gradually sheds the vorticity of the leading edge vortex. Before the vortex can shed, the wing translation slows and simultaneously rotates in steps 2 and 3, as if to a higher angle of attack. Adding circulation to the flow generates lift, and the wing rotation in steps 2 and 3 generates more circulation than translation alone. Finally, the wing reverses direction and the viscous wake from the previous stroke interacts with the wing, thereby increasing its lift. Utilizing such mechanisms in flight, insects are able to create much higher average lift coefficients than steady aerodynamics might imply. A fruit fly, for example, produces an average lift coefficient of about 1.4 over the complete cycle of its stroke [30]. Even the maximum lift coefficients of optimized airfoils cannot match the average lift coefficients that insects produce at this triple

digit Reynolds number.

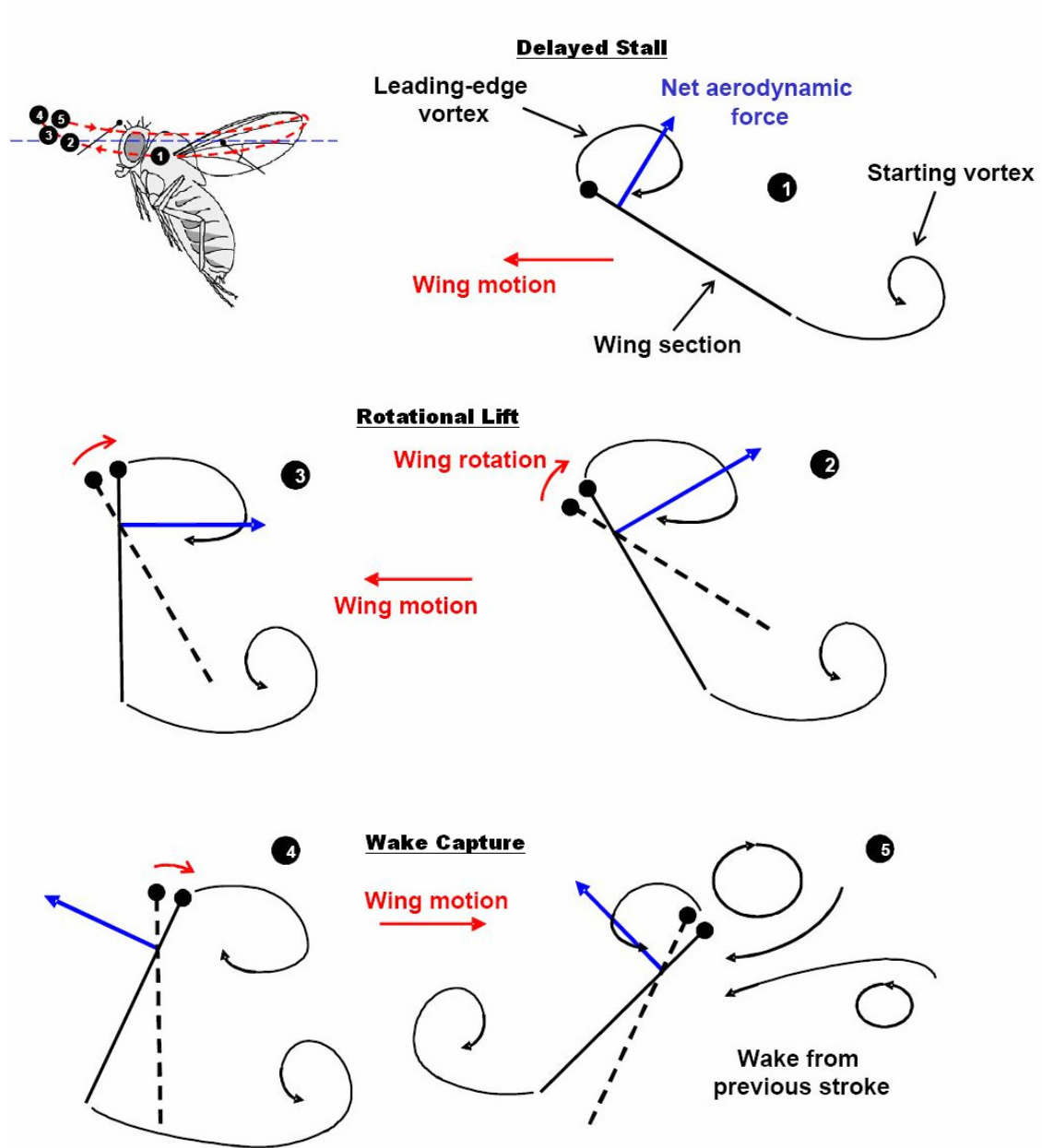


**Figure 15: Delayed Stall, Rotational Lift, Wake Capture**

Once the kinematic motions of flying creatures were understood, researchers began simulating the motions with mechanical apparatuses in the lab. Some hoped to build a flying vehicle, but the most useful research has been through flapping models

used to better understand the aerodynamics. In these mechanical models, forces are measured directly and the flow can be carefully scrutinized. The leading edge vortex that delays stall and allows higher angles of attack has been verified and shown to be a stable phenomenon. It remains attached even under steady translation, because it spirals out toward the lower pressure region near the wingtip, where it combines with the wingtip vortex [31, 32]. The leading edge vortex remains attached due to spanwise flow. It has been suggested through theory and experiment that the spanwise flow and stable leading edge vortex occurs only over a range of Reynolds numbers on the order of  $10^2 - 10^5$  [31, 33]. MAVs normally operate within this range.

### 1.4.3 Bio-Inspired Aerodynamics

Some of the same researchers that are simulating insect wing motion are also using simpler methods and models to study the aerodynamic phenomena associated with flapping motion. Testing fixed wings of hover capable flying creatures in a wind tunnel does not provide accurate results, because it subjects the entire wing to a uniform freestream velocity [34]. Each wing section of a hovering animal is not subjected to the same freestream velocity because the wing is flapped while it is fixed at the root. The velocities at the tip will therefore be higher, just like a helicopter blade. The steady aerodynamics that occur during mid-stroke can be observed by rotating the wings on a hover stand, visualizing the flow, and measuring the forces.

Many rotating animal wing experiments have been performed by Usherwood and Ellington [34, 35] and Altshuler, Dudley and Ellington [36] at low Reynolds

numbers ( $<10,000$ ) with actual wings and scale models of wings from different insects and birds. The researchers used a rotating hover stand because the spanwise flow that stabilizes the leading edge vortex is weak in a conventional wind tunnel test. The rotating wing experiments have shown a stable leading edge vortex and spanwise flow during steady rotation. Due to the stable leading edge vortex, angles of attack reached upwards of  $40^\circ$  without excessive flow separation and stall. In fact, the lift curve slopes during these experiments remained linear up to and above  $30^\circ$  angle of attack and maximum lift coefficients were about 1.3 for most of the wings tested. Actual hummingbird wings showed the highest maximum lift to drag ratio of 10, while the rest of the wings tested produced lift to drag ratios of about 5. Most insects in hover achieve average lift coefficients higher than the lift coefficients that their wings can produce in steady motion, whether rotation or translation. Therefore, other unsteady mechanisms, such as delayed stall and rotational lift, are clearly at work.

There have literally been dozens of studies and experiments completed on the subject of dynamic and delayed stall of translating and rotating wings and airfoils. Since most of these studies were conducted to understand full size helicopters and aircraft, relatively few have been done that focus on low Reynolds number delayed stall. One low Reynolds number study by Okamoto and Azuma focuses on heaving and feathering oscillations of wings in a wind tunnel at a Reynolds number of 8000 [37]. Instantaneous and average forces were measured while the wings were operating both steadily and oscillating at a reduced frequency of 0.32 in heaving, feathering, or a combination of heaving and feathering. Flat plates, cambered plates, and corrugated plates were tested, all of which are known to perform well at low

Reynolds numbers.

The flat plates showed evidence of stall under steady conditions at  $8^\circ$  angle of attack and a lift coefficient of 0.7. While undergoing heaving motion at a reduced frequency  $k$  of 0.32, the maximum lift coefficient increased to 1.1 at an average angle of attack of  $26^\circ$ . That is an increase in average maximum lift coefficient of over 50%. A curved plate with 9% camber, which generally achieves one of the highest lift coefficients in this flow regime, was also tested. In steady state, it achieved a maximum lift coefficient of 1.2 at an angle of attack of  $12^\circ$ . During periodic heaving motion, the maximum average lift coefficient increased about 20% to 1.4. With an optimal combination of heaving and feathering at a phase difference of  $90^\circ$ , these wings produced positive thrust coefficients.

The idea of plunging wings creating a propulsive force is not new. As early as 1909 and 1912, Knoller and Betz, respectively, independently theorized that a wing can produce thrust when it plunges periodically with respect to a freestream velocity [38, 39]. They were investigating the method for avian propulsion. In 1922, the Knoller-Betz effect was experimentally verified by Katzmeyer with wind tunnel measurements [40]. The idea behind the effect is quasi-steady in nature and is seen in the simplified diagram in Figure 16.

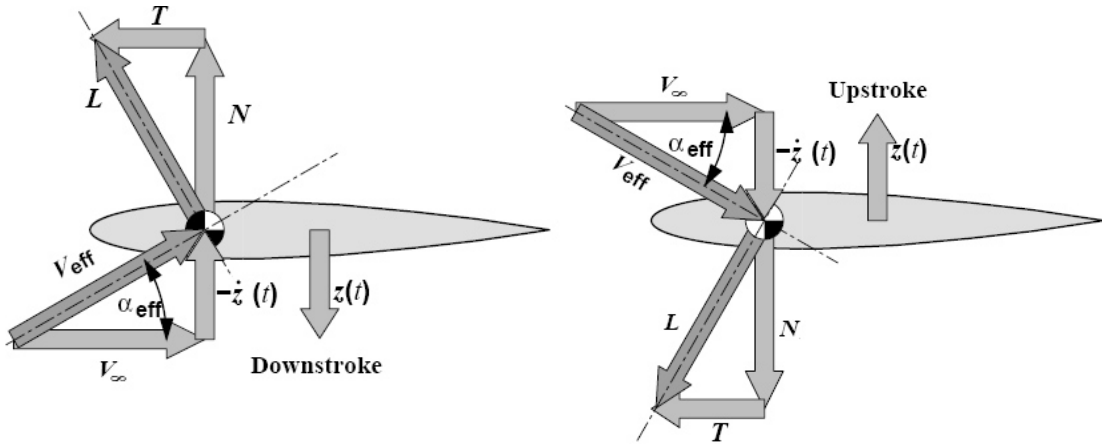


**Figure 16: Forces and velocities on a plunging airfoil**

The plunging airfoil's vertical position is defined by  $z(t)$ . The vertical velocity of air induced on the airfoil is in the opposite direction of the airfoil's vertical velocity and is shown as  $-\dot{z}(t)$ . When the vertical air velocity  $-\dot{z}(t)$  combines with the freestream velocity  $V_\infty$ , the resultant freestream velocity is  $V_{eff}$ , which causes an effective angle of attack  $\alpha_{eff}$ . The lift  $L$  acts perpendicular to  $V_{eff}$ , which means the lift tilts in a forward direction. The lift force here is broken down into two forces on the airfoil: the normal force  $N$  and the thrust force  $T$ . If the lift is great enough, the plunging airfoil can produce a useful thrust. The drag in this figure is assumed small with respect to the lift.

Recently, the Naval Research Lab has examined plunging and pitching wings as a primary propulsion method for MAVs. Their vehicles, such as the "delphinopter" in Figure 17, have been some of the most successful flying vehicles of any scale that utilize this propulsion method. The delphinopter produces thrust with its plunging and pitching rear wing and produces lift with its fixed front wing [41].

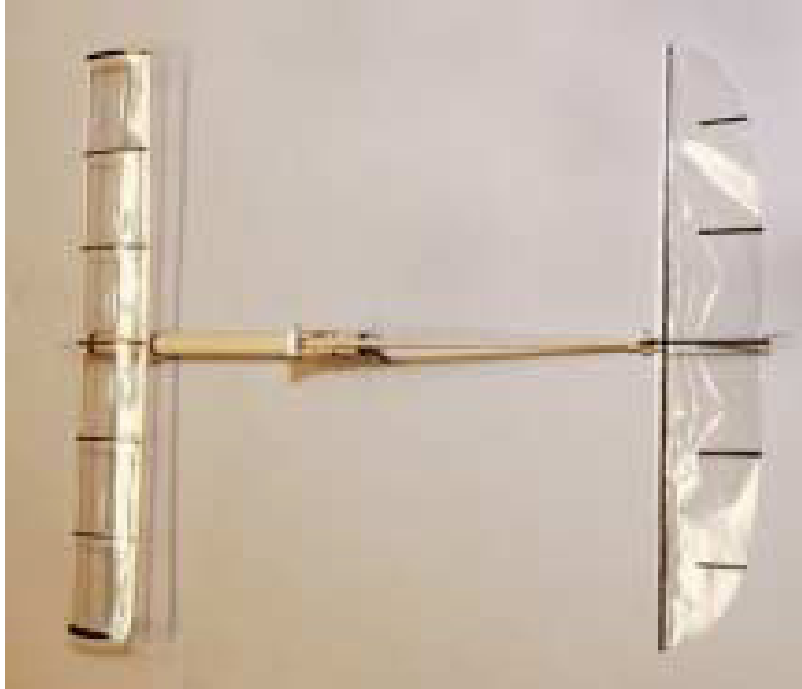


**Figure 17: NRL delphinopter**

#### 1.4.4 Flapping Rotor Concept

If flapping wings can be the propulsion mechanism for birds and aircraft, then flapping blades should be able to power the rotation of a helicopter rotor as well. This is the expectation of a research group at Delft University of Technology [42]. They have developed a flapping rotor system that flaps its blades once per revolution at an amplitude of  $12^\circ$ . The amplitude is enough for the lift vector of the blades to tilt forward and produce a propulsive force in the direction of rotation. While flapping the blades at zero collective can obviously supply a rotational force, the group at Delft has shown that blade flapping eliminates the need for torque into a helicopter rotor at positive collectives as well. At a blade element level, the effect of zero collective and positive collective is shown in Figure 18 (a) and (b), respectively. The

first case (a) produces zero net lift but a large forward thrust. This is simply the Knoller-Betz effect. The second (b) demonstrates positive net lift and positive thrust, where average thrust equals the average drag. It is in this regime where there is no torque required into the rotor shaft. The “Ornicopter” may be the only flapping rotor previously tested in a scientific environment. Because of the large structural forces of helicopter blades flapping at high amplitudes, this idea may be better applied to an MAV.

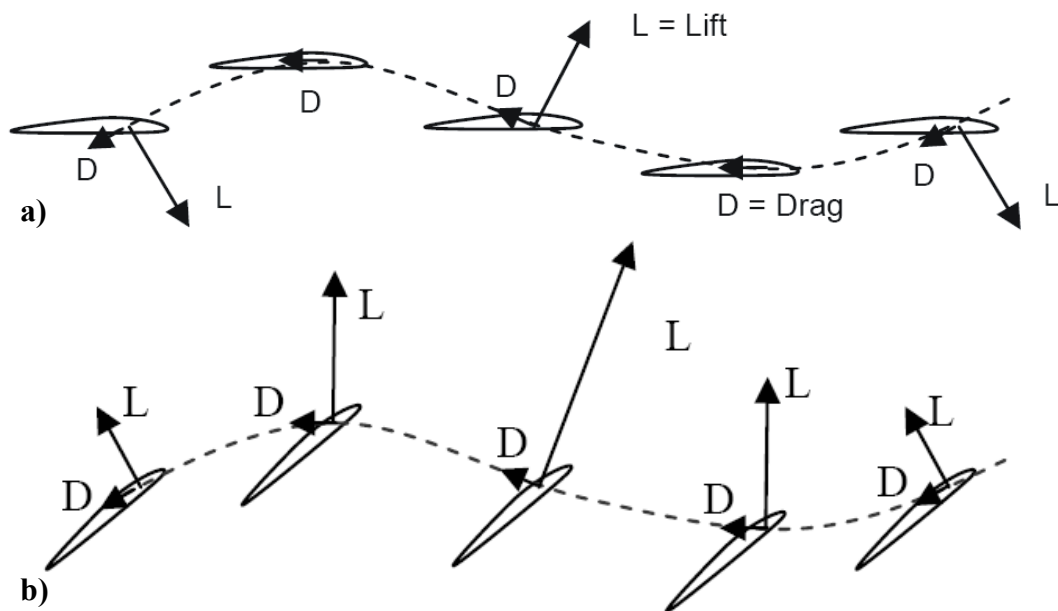


**Figure 18: Forces on flapping blade**  
**at: a) zero collective and b) positive collective**

A micro rotor with blades that can independently flap, pitch, and rotate was developed and patented by Bohorquez and Pines [43], but it was not tested with high frequency flapping. It was tested in pitching to a frequency of two flaps per rotor revolution. It was found that higher maximum thrust coefficients and slightly reduced power coefficients were possible with active high frequency blade pitching.

## 1.5 Current Research Objectives

Methods developed in nature for high levels of lift and thrust at low Reynolds numbers can also be applied to MAVs. Biologically inspired methods, such as flapping wings, can increase the thrust of MAVs while potentially reducing their power required to fly. An increase in thrust and a simultaneous reduction in power would lead to an increase in payload, a more compact design, and an increase in endurance.

The objective of the current research project is to utilize a combination of conventional rotation plus avian based flapping motion to increase the performance of an MAV rotor. Through avian based blade flapping in conjunction with passively flexible blades, this flapping rotor should be able to reduce or even eliminate the torque necessary to rotate its blades and produce thrust. This MAV flapping rotor should harness delayed stall and rotational lift. These methods should be introduced one at a time into a well documented system in order to understand and measure their individual effects. This dissertation will describe in detail the design and testing of a flapping rotor system for an MAV.

## 1.6 Outline

To fully understand the problems and methods, this thesis is organized as follows. In the first chapter, performance goals for an MAV are defined. An overview of state of the art technology in this area is presented, along with

advantages and disadvantages of each configuration. Prior related research and relevant results have been used to describe aerodynamic challenges. Some potential methodologies by other researchers for overcoming these challenges are presented.

Chapter two describes a proposed solution, which is a small flapping rotor system dubbed the “Flotor”. The advantages and disadvantages of such an idea are discussed. The design process is described step by step and compared to empirical trends from nature. The initial sizing and motion requirements are presented, followed by the design and fabrication of the actual research test bed.

In chapter three, the design is analyzed. The geometry and kinematics of the mechanism are described graphically and mathematically. The aerodynamic analysis is developed using quasi-steady approximations and theoretical calculations are discussed.

Chapter four presents the experimental techniques and data gathered with the test bed. The experimental parameters, constraints, and assumptions are described and the results are presented.

In chapter five, conclusions are drawn from the results and apparent anomalies are explained. This final chapter concludes the development of the Flotor flapping rotor concept for micro air vehicles. The future of this research project is discussed in terms of improvements and the next steps for demonstrating the concept viability for a flying vehicle.

## 2 Concept and Design

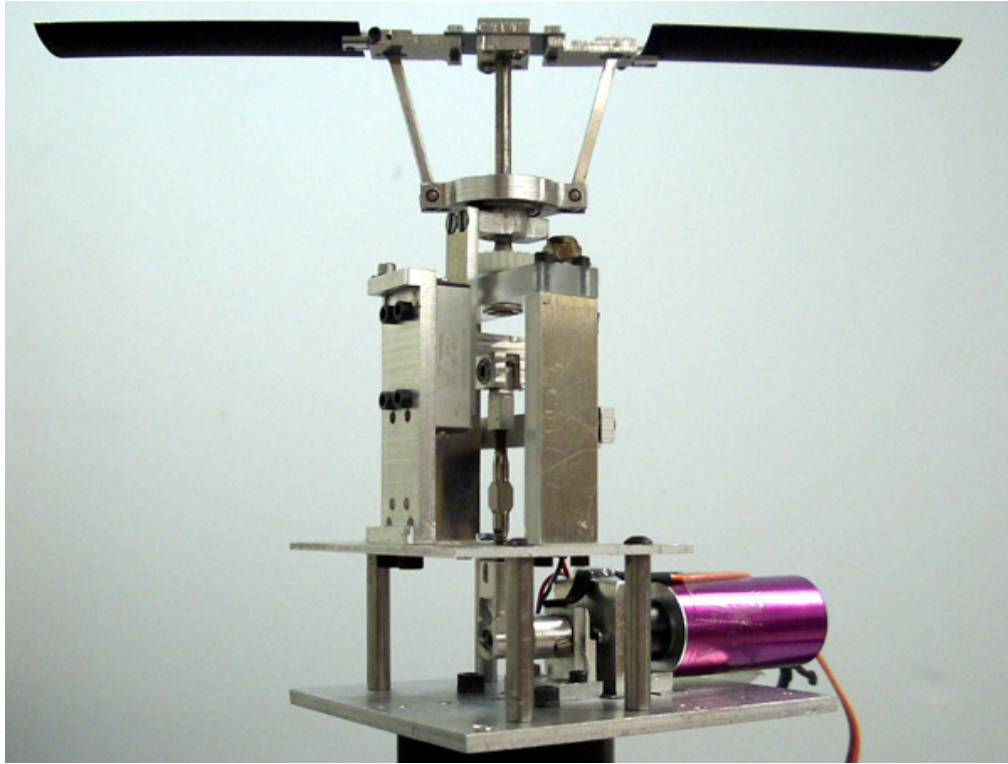


**Figure 19: Flotor**

The Flotor, seen in Figure 19, is a micro rotor test stand that is used to demonstrate the effects of high frequency blade flapping on average rotor forces. It is capable of independent flapping and rotating motion and it can rotate freely due to the aerodynamic forces caused by blade flapping.

### 2.1 Advantages

The Flotor concept combines the advantages of an avian based flapper and a conventional rotor. Like an insect, the maximum airspeed of the blades is at the blade tips and the blades flap about a root with near zero airspeed. The Flotor could

produce higher thrust coefficients than a conventional rotor due to a combination of unsteady and conventional aerodynamic mechanisms, delayed stall and rotational lift. Like an avian based flapper, the blades of the Flotor could generate their own propulsive force in the chordwise direction, as in Figure 18. The propulsive force from flapping will cause rotation about a central hub. The Flotor can utilize the freestream velocity from rotation to generate lift, like a bird in forward flight. To maintain a vertical force, the blade angles on the Flotor do not need to be as carefully trimmed as on an insect or avian flapper. The benefit of constant blade rotation about a central hub is that the aerodynamic forces are easily averaged into a vertical thrust vector, resulting in a hover capable device.

## 2.2 Disadvantages

Some disadvantages of the Flotor are also similar to the disadvantages of flapping wing vehicles. The mechanism for blade flapping is more complex than a conventional rotor and the flapping efficiency is not well established. There are periodic inertial forces that are directly proportional to the mass of the blades. Since the blades in this case flap vertically, the inertial forces oscillate in a vertical direction. Aerodynamically and structurally, the blades must be more carefully optimized than blades on a conventional rotor.

## 2.3 Initial Rotor Design and Sizing

The basic blade length was constrained to be on the order of three inches in order to fit within the accepted size range for an MAV. The rotor diameter should be

on the order of six inches. Starting with the size constraint, the remainder of the initial design was compared to similar size flying creatures. Birds, insects, and bats all fit tight trends of sizing and performance parameters such as mass, wing span, aspect ratio, wing loading, flight speed, and flapping frequency. The parameter relations can usually be fitted to an equation of the form  $y = am^\beta$  [44,45], where  $y$  is the parameter in question,  $m$  is the mass of the flying creature, and  $a$  and  $\beta$  are constants fitted to the data with a least squares fit.

### 2.3.1 Thrust

In nature, creatures with a wingspan of six inches are generally birds or bats, so the thrust of the Flotor can be compared to the thrust of birds and bats of similar size. Figure 20 [44] shows the correlation between mass and wingspan for flying creatures in nature as well as the DARPA goal for an MAV. While the MAV goal is 15 cm span and 100 grams of vehicle mass, flying creatures with a span of 15 cm have a mass of 10 grams at the most. The relationship between the mass ( $m$ ) and wingspan ( $b$ ) of small bats fits the equation  $b = 1.3m^{0.34}$ , which corresponds to a mass of about 4 grams for a span of 6 inches [44]. According to a compilation of sizing parameters for all birds (excluding hummingbirds) [46,47,48], the relationship emerges of  $b = 1.17m^{0.39}$ . This corresponds to a bird mass of 8 grams for a span of 6 inches. The sizing parameters for hummingbirds show the relationship  $2b = 2.24m^{0.53}$ , also corresponding to a mass of about 8 grams [49].

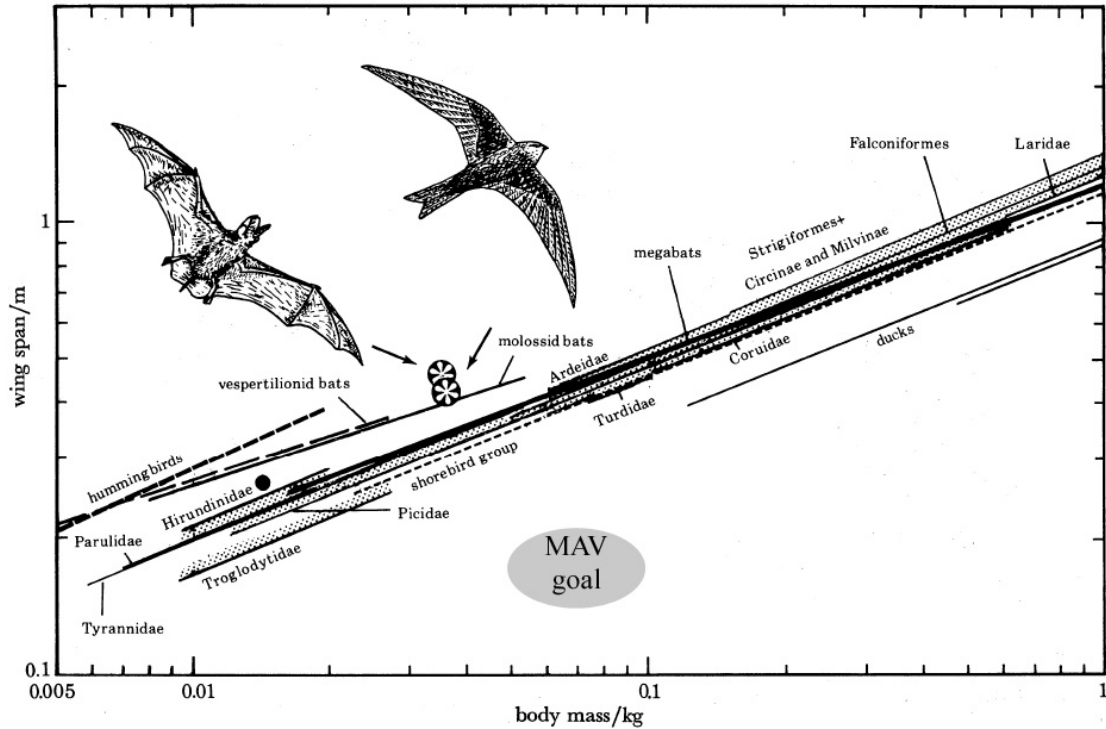


**Figure 20: Wingspan vs. body mass for various birds and bats [44] and sizing goal for MAVs.**

Some flying creatures can produce thrust considerably greater than their weight. Some bats, for example, can carry their young in flight and experiments have shown that they will willingly take off and fly even when loaded with over 70% of their bodyweight on their backs [50]. In constant forward flight, they would be able to carry considerably more. For such reasons, the Flotor should be able to produce more thrust than just the weight of similarly sized flying creatures. The high thrust goals compared to biological flyers requires a combination of higher wing loadings, higher lift coefficients, and higher flight speeds, therefore requiring more power and possibly reduced endurance [22].

### 2.3.2 Blades

The first blades manufactured for the Flotor were sized to imitate the wings of flying creatures of similar size. Their shape and scale are similar to the wings of small birds or bats and their structure is similar to that of a bat. Based on mass, the aspect ratio relationship for bats is  $b^2/S = 11m^{0.11}$  [44] and for birds is  $b^2/S = 8.56m^{0.06}$  [46]. According to this relationship, bats of this size have wings with an aspect ratio of about 6.5, and birds have wings with an aspect ratio of about 6.6. In nature, as the mass decreases, so does the aspect ratio.

Since the total blade span, the aspect ratio, and the thrust are relatively constrained, the blade area and blade loading can be directly calculated and also compared to trends in nature. With a blade span of 16 cm and an aspect ratio of 6.5, the blade area will be 40 cm<sup>2</sup>. With a thrust of about 20 grams force, the wing loading is 0.5g/cm<sup>2</sup>. This level of wing loading is about two times higher than that of flying creatures of this size [48]. In general, larger flying creatures attain higher wing loadings, but they also fly at higher airspeeds.

### 2.3.3 Rotational Speed

In general, avian flight requires a forward airspeed for the wings to generate lift. Except for hummingbirds, birds and bats utilize forward flight for their most efficient flight. The empirical models for the small bird group “Passeriforms” show that the speed for maximum range follows the trend  $8.63m^{0.14}$ . Bats flying long distances tend to fly at a velocity based on their mass of  $11.8m^{0.21}$  [45]. For a flying creature in the size regime with the Flotor, these empirical relations point to a forward

flight speed ( $V$ ) of 5 or 5.2 m/s, respectively. For comparison, the reference airspeed of the Flotor blades is calculated at  $\frac{3}{4}$  of the rotor radius. Since the Flotor radius ( $R$ ) is 0.08m, the Flotor should rotate its blades at approximately

$$\Omega = \frac{V}{\frac{3}{4}R} = \frac{5.1\text{m/s}}{0.06\text{m}} = 85\text{rad/s}, \text{ or } 811 \text{ RPM.}$$

## 2.4 Flapping

The flapping frequency and flapping amplitude of biological flyers generally decreases with increased size. Relationships comparing flapping frequency with body mass are seen in Figure 21 and show a great deal of scatter [51,52]. The predicted upper and lower flapping frequency limits for a creature with a mass on the order of 10 to 20 grams is in the range of 10 to 50 Hz. Since this parameter has such a wide range of variation in nature, it will be one of the main variables in the analysis and experiment.

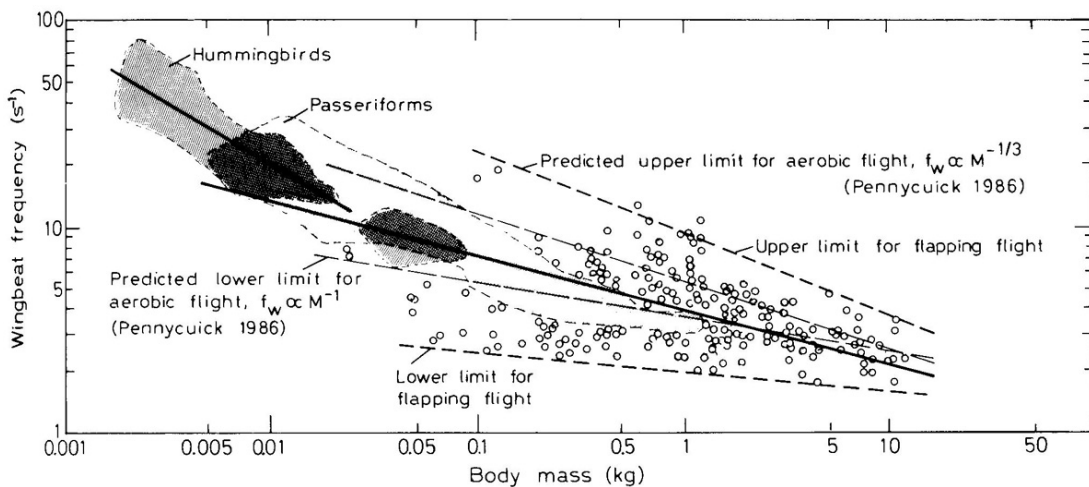


**Figure 21: Wingbeat frequency vs. Body mass for birds [51,52]**

Flapping provides propulsion in forward flight, but, at higher frequencies, it

also introduces unsteadiness into the airflow. The measure of this unsteadiness is commonly referred to as “reduced frequency”,  $k$ , where  $k = \frac{\omega c}{2U}$ . The flapping frequency is  $\omega$ , the wing chord is  $c$  and the airspeed is  $U$ . The flow is assumed steady when  $k < 0.05$ . When  $k > 0.2$ , the flow is so unsteady that the time varying airloads can no longer be accurately predicted by conventional steady or quasi-steady aerodynamics [53]. Biological flyers in the size range of the flotor operate completely in the unsteady regime. The general reduced frequency trend in nature can be estimated with the parameters that have already been provided. For a creature of the size of the Flotor with a wingspan of 0.16 m and a total area of 0.004 m<sup>2</sup>, the average wing chord is about 0.025m. The forward flight speed is 5.1m/s. The range of flapping frequencies is between 10 and 50 Hz, or 63 and 314 rad/s. These parameters mean the reduced frequency for flying creatures in this regime generally lies between 0.15 and 0.77, excluding hummingbirds. Some hummingbirds flap their wings even faster. Thrush Nightingales, for example, are a bird with a mass of about 30 grams. They fly with a reduced frequency of 0.19 when in fast forward flight and 0.53 when in slow flight [54]. The Flotor is designed to operate in this range.

## 2.5 Design and Fabrication

The Flotor was designed as an experimental test bed capable of independently flapping and rotating its blades. The mechanism was designed to be a robust platform with predictable movement and easily adjustable motions. It was configured in order to accurately measure the aerodynamic forces created during experiments. It was not

designed for efficiency of flapping or minimum weight. Because low weight was not a priority, the safety factor of most parts is an order of magnitude higher than it would be for a flying vehicle. Most of the Flotor was constructed with aluminum due to its easy machinability and relatively high strength and rigidity. Off the shelf components were utilized when possible to reduce the time for manufacture.

### 2.5.1 Basic Components

The blade flapping actuation of the Flotor is based on blade pitch actuation in full scale helicopters. A ball bearing swashplate is utilized to transfer loads from the fixed frame to the rotating frame. Instead of actuating the blade pitch, the swashplate directly actuates the blade flapping collectively. Moving the swashplate vertically causes the blades to flap in phase in the same direction. The rotor and swashplate assembly is shown in Figure 22.

The links from the swashplate to the blade grips are attached along the blade chordwise center of mass so that the periodic forces from the links do not cause any flap-feather coupling. The swashplate link ends, which are hidden inside the blade grips, contain ball bearings to sustain the flapping load with minimum friction. The lower end of the links are attached to the swashplate with a pin, since that connection rotates only a small amount. The swashplate and rotor shaft operate concentrically and without contact. The swashplate is constrained to linear vertical motion with a low friction Tusk BX2-1 linear slide.

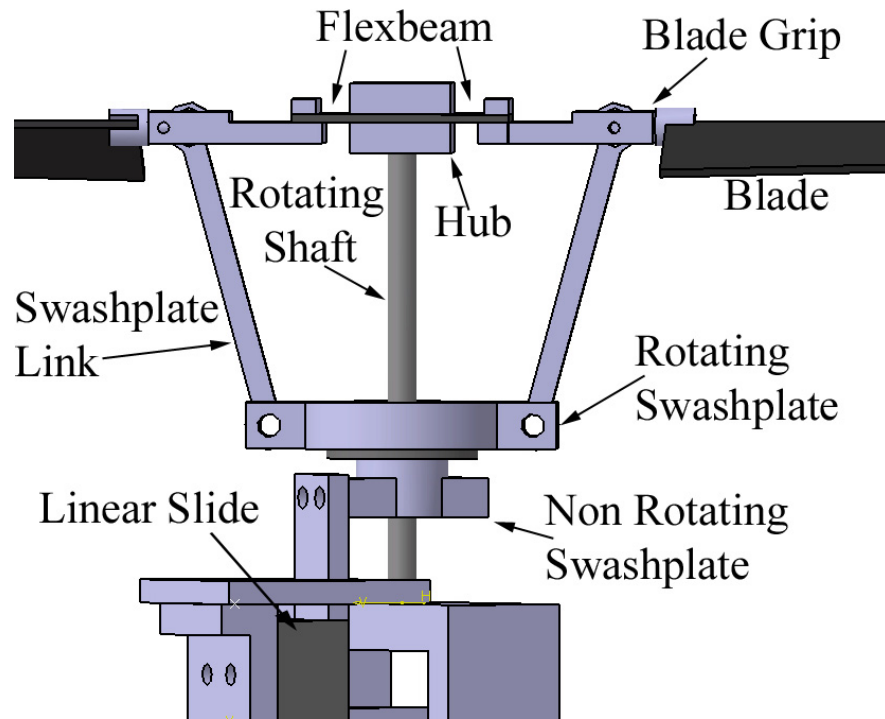


**Figure 22: Rotor and swashplate components**

A two view diagram of the linear actuation design is shown in Figure 23. The non-rotating swashplate is fastened onto the linear slide with screws, making a firm cantilever connection. Also attached to the linear slide is a bracket that secures a connecting rod with ball bearings, making a pin connection. The other end of the connecting rod is also a ball bearing pin connection. It rotates about an offset pin on the flywheel of a Hacker brushless motor, which is called the flapping motor. The mechanism allows a rotary motor to produce linear actuation with very little friction.

When the swashplate is actuated, the flapping motion of the blades is allowed by a spring steel flexbeam. The flexbeam is sandwiched by the two-piece hub in the center and by the blade grips on both ends. The clamping force for the hub and the blade grips comes from two screws that pass through the flexbeam at each attachment

point. With a blade length of 3 inches, this configuration causes a hinge offset of 5% and a root cutout of 25%, as seen in the drawing in Figure 24.

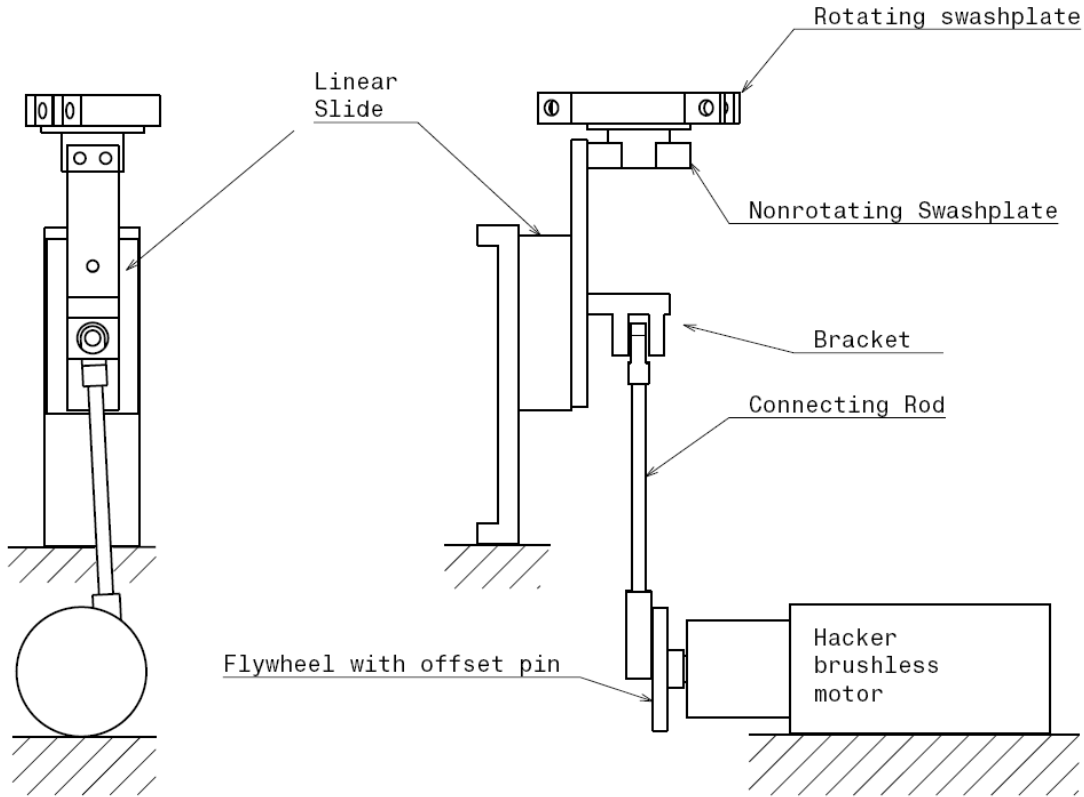


**Figure 23: Rear and side view of linear actuation mechanism**

The shaft of the rotor has two ball bearings at its base, which constrain its axis of rotation. The rotor can be operated with or without a motor to power the shaft rotation. Without a motor in contact with the shaft, the rotor can freely rotate, experiencing aerodynamic drag and minimal ball bearing friction. In the freely rotating configuration, aerodynamic forces from the flapping blades are the only forces that can cause the rotor to rotate. To better control the rotation speed of the shaft, a Firefly coreless DC motor with 4:1 planetary gearhead is used to power the shaft rotation in most cases. This is called the rotation motor. The rotation motor

gearhead output shaft drives the rotor shaft with a 1:1 ratio gear. The 1:1 gear ratio was limited by size constraints of the design.

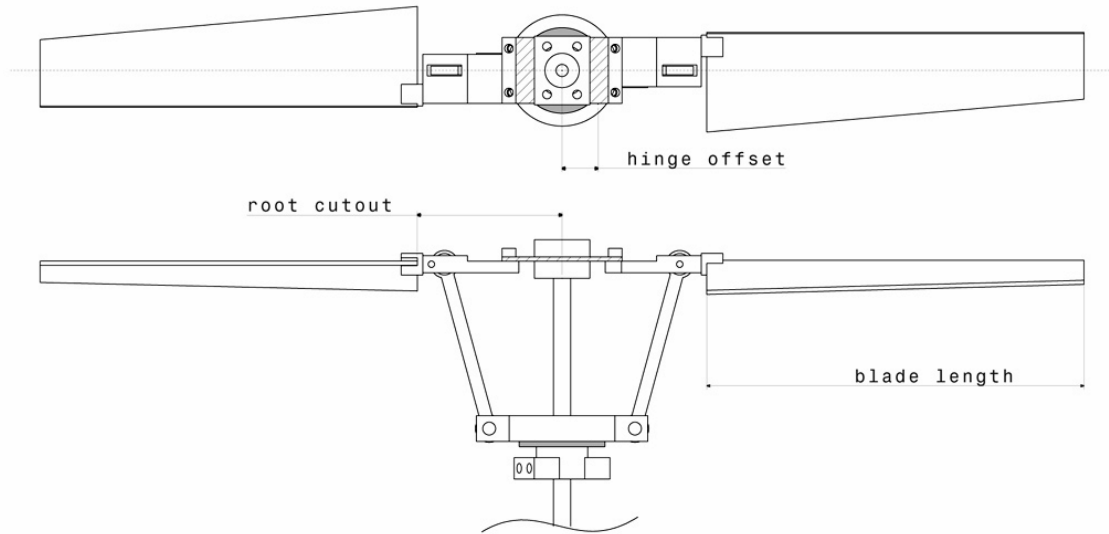


**Figure 24: Front and Top view of swashplate and rotor**

### 2.5.2 3-D Solid Model and Construction

Before a single piece was constructed, the entire flotor went through multiple iterations of 3-D solid modeling. CATIA was chosen for its ease of operation and accessibility. Each part was designed along with its neighboring parts and assembled in 3-D computer workspace to ensure an exact fit. The parts were then machined in-house using a miniature lathe and a three axis milling machine, both with CNC capability. The CNC was primarily utilized on the mill for accurately cutting 2-D profiles to different depths. Figure 22 shows an iteration of part of the 3-D model. The completed 3-D model is shown in Figure 25. The cylinder on the rear of the flapping motor is a device to measure torque. A catalog of parts is kept for posterity

in the Alfred Gessow Rotorcraft Center graduate student office.

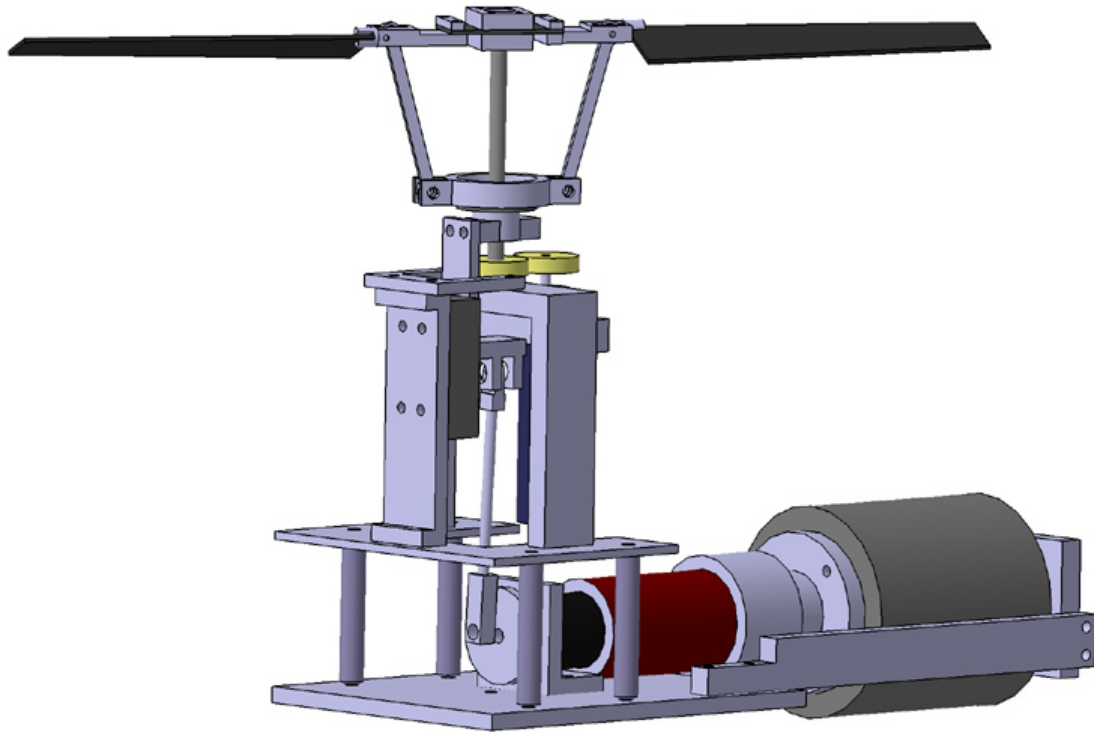


**Figure 25: 3-D model of Flotor**

### 3 Analytical Models

Prior to its operation, the kinematics of the Flotor were planned and modeled. The kinematic model was used to predict the blade motion, which was used to predict aerodynamic forces. From the forces, the overall thrust, power, and figure of merit can be predicted.

#### 3.1 Kinematics and Mechanics

The kinematics of the Flotor can be analyzed by breaking it down into more abridged components. First, the flapping mechanism will be analyzed, starting with

the flapping motor and flywheel with offset pin. The mechanism has been simplified in Figure 26. The swashplate has not been modeled as a separate part, because, for the purpose of this simplified model, the swashplate is rigidly attached to the linear slide. This simplification is for predicting the flapping motion, so the swashplate rotation is not included in this diagram.

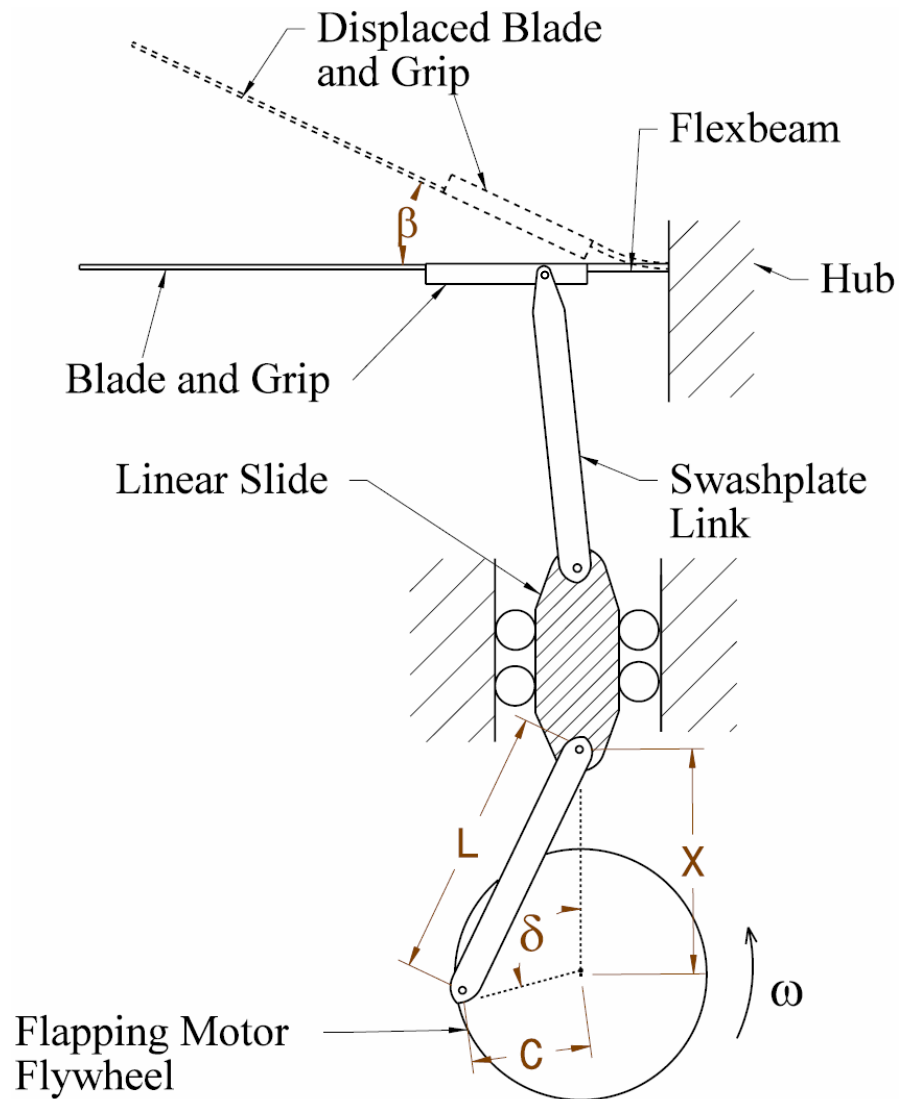


**Figure 26: Simplified blade flapping mechanism**

The flapping motor flywheel rotates at an angular velocity  $\omega$ . The connecting rod of length  $L$  is pinned to the flywheel at a distance  $C$  from the flywheel center. The connecting rod has a pin-pin connection to the flywheel pin and to the linear slide, so the force through the connecting rod is only in tension or compression. The force through the connecting rod drives the linear slide, which rolls linearly on ball bearings. The position,  $X$ , of the linear slide above the flywheel center depends on the angular position of the flywheel,  $\delta$ .

The swashplate link is also a pin-pin connection, with one end pinned to the swashplate and the other end pinned to the blade grip. Because of very small angular deflections of the swashplate link, the vertical distance from the linear slide to the pin connection at the blade grip can be assumed constant. When the linear slide moves vertically, the swashplate link is assumed to move vertically by the same amount and carry the forces. The axial force through the swashplate link causes a moment in the flexbeam. This moment bends the flexbeam and causes the rigidly modeled blade and blade grip to deflect at an angle  $\beta$  with respect to horizontal. The motion of these parts will now be described and simplified.

First, the vertical swashplate motion will be described. The linear mechanism that drives the swashplate has motion much like a piston in an internal combustion engine and actually has the same equations of motion [55]. The equation for swashplate position is solved through simple trigonometry. The vertical velocity and acceleration of the swashplate is then found by differentiating the position equation with respect to time.

$$\text{Displacement} \quad X = C \cos \delta + \sqrt{L^2 - C^2 \sin^2 \delta}$$

$$\text{Velocity} \quad \dot{X} = \left( -C \sin \delta - \frac{C^2 \sin \delta \cos \delta}{\sqrt{L^2 - C^2 \sin^2 \delta}} \right) \omega$$

$$\text{Acceleration} \quad \ddot{X} = \left( -C \cos \delta - \frac{C^2 (\cos^2 \delta - \sin^2 \delta)}{\sqrt{L^2 - C^2 \sin^2 \delta}} - \frac{C^4 \sin^2 \delta \cos^2 \delta}{(\sqrt{L^2 - C^2 \sin^2 \delta})^3} \right) \omega^2$$

From the equations alone, it can be seen that the vertical motion of the swashplate is not sinusoidal. In the case of the Flotor, the connecting rod length  $L$  is 2 inches and the crank radius  $C$  is variable. The ratio of  $C/L$  is referred to as the “crank ratio”. One cycle of swashplate motion is plotted in the following figures for two different values of crank ratio. The swashplate displacement is shown in Figure 27. In this case, the motion of the swashplate for a crank ratio of 0.1 is nearly indistinguishable from sinusoidal motion. The larger crank ratio of 0.5, however, causes an obvious variation from sinusoidal motion that appears to be a shift in phase.

The variation from sinusoidal motion becomes even more obvious when examining the vertical velocity and acceleration of the swashplate. The velocity is shown in Figure 28 and the acceleration is shown in Figure 29 for two different crank ratios. This type of movement will be apparent in any mechanism that relies on a crank and connecting rod to actuate a linear motion. It is important to take into account this motion when analyzing MAV flapping mechanisms, which sometimes utilize large crank ratios in the interest of compactness.

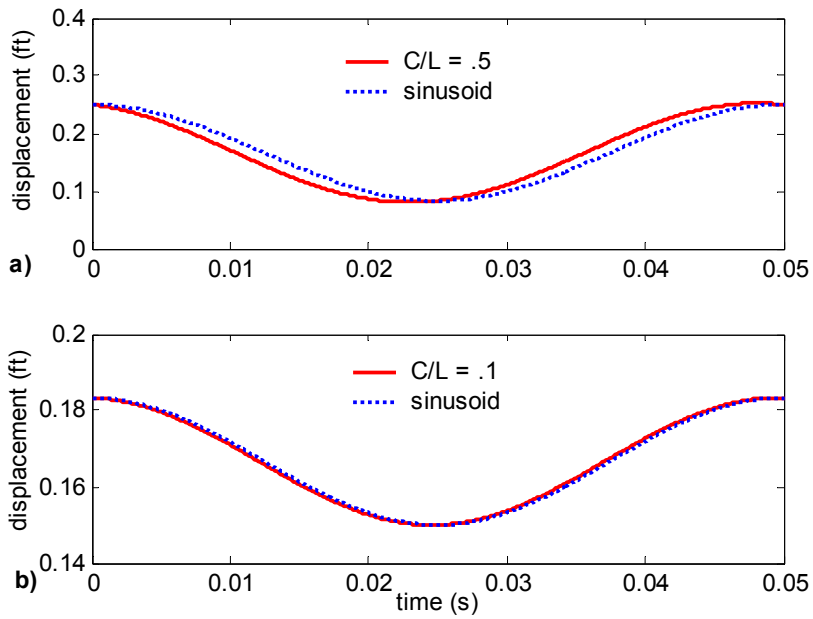


**Figure 27: Swashplate displacement for crank ratios of a) 50% and b) 10%**

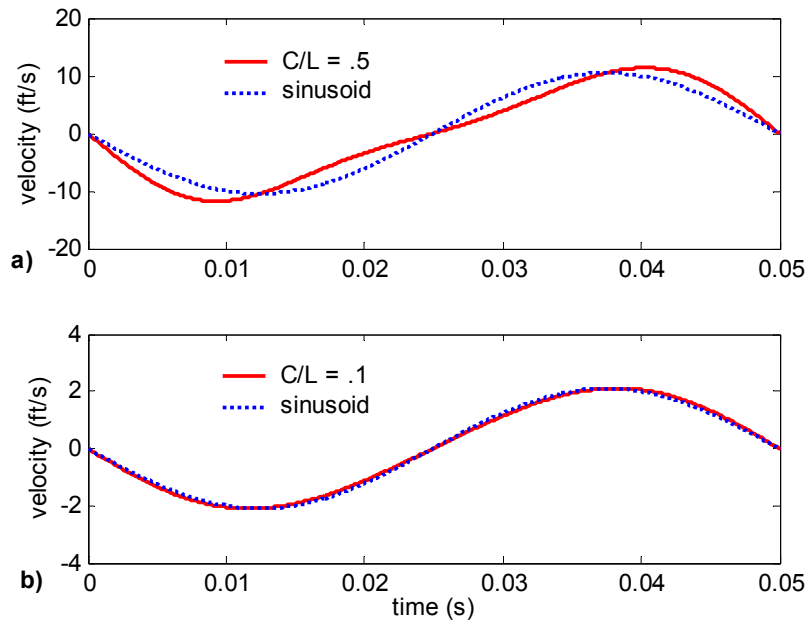


**Figure 28: Swashplate vertical velocity for crank ratios of a) 50% and b) 10%**

Since the Flotor mechanism was not designed with a strict goal of miniaturization, it can utilize a small crank ratio with a relatively long connecting rod. The crank distance  $C$  on the Flotor is never more than 10% of the connecting rod length  $L$ , so  $C/L=0.1$  demonstrates a worst case scenario for the Flotor's variation from sinusoidal motion. Except for very large amplitudes, the flapping motion of the Flotor can be modeled as sinusoidal.

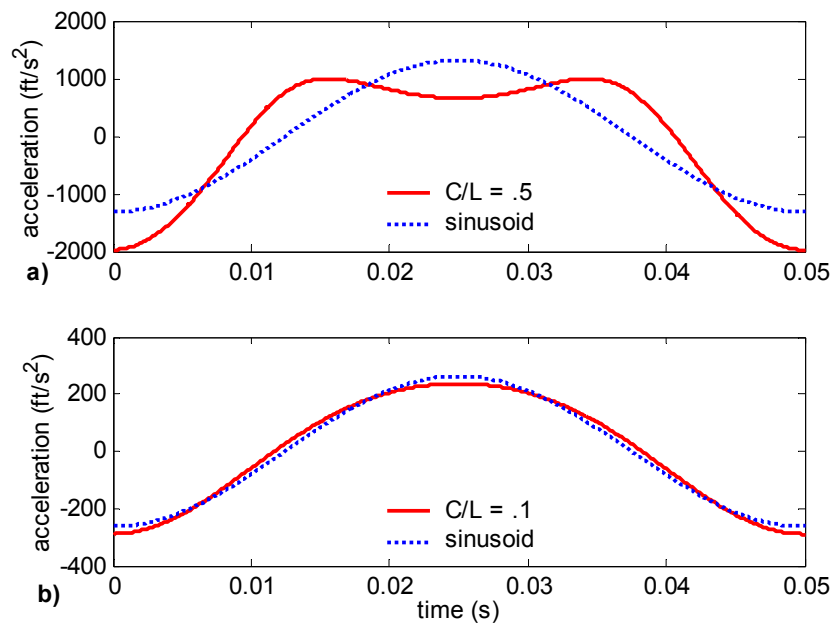


**Figure 29: Swashplate vertical acceleration for crank ratios of a) 50% and b) 10%**

### 3.2 Aerodynamics

The aerodynamic analysis of the Flotor uses conventional helicopter theories with some modifications for low Reynolds number effects and high amplitude flapping. The first analytical model was for a conventional MAV rotor. The second model introduces flapping into the quasi-steady model.

### 3.2.1 Rotation

In a blade element analysis, the blade is broken into sections and each section is analyzed individually. The aerodynamic forces from each element are then summed to obtain the overall forces on the rotor. This analysis is performed at each collective angle from  $0^\circ$  to  $36^\circ$  in steps of  $2^\circ$ . The basic radial distances and in plane velocities on a helicopter blade element are shown in Figure 30.

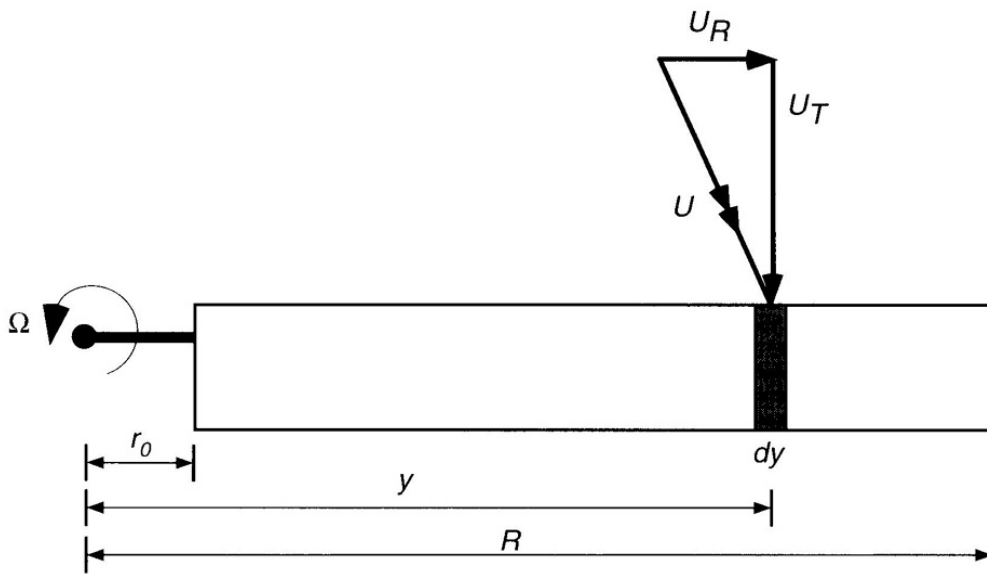


**Figure 30: Blade and blade element distances and velocities [53]**

The overall rotor radius is  $R$  with a root cutout of  $r_0$ . The blade is rotating with an angular velocity of  $\Omega$  radians per second. The blade element width is  $dy$  and is located a distance  $y$  from the rotor center. The in-plane wind velocity due to rotation is  $\Omega y$ . In hover, it is assumed that the radial component of the velocity,  $U_R$ , is zero. A cross section of the blade element and the aerodynamic vectors and forces acting upon it are shown in Figure 31.

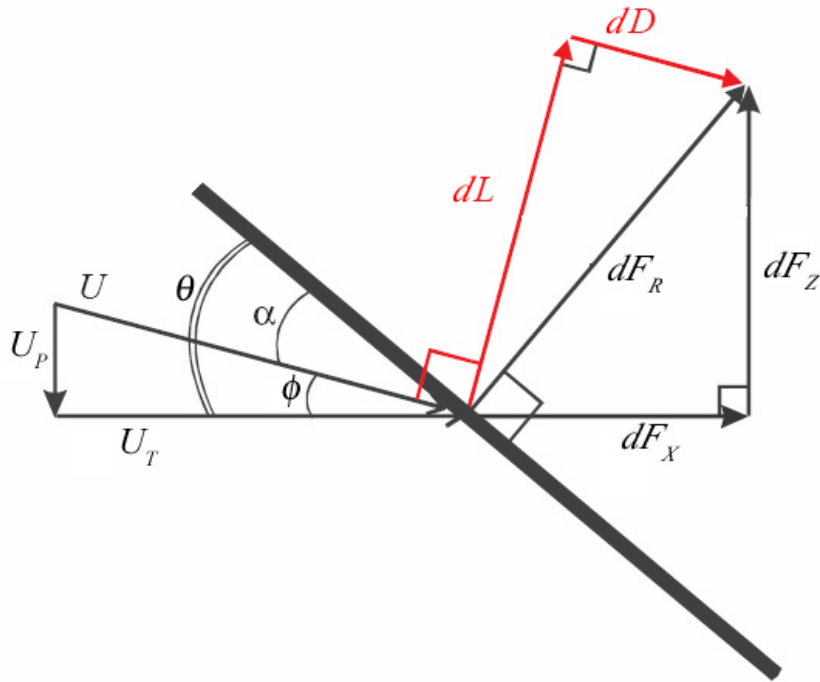


**Figure 31: Blade element angles, vectors, and forces**

$U_T$  is the airspeed of the blade section in the plane of rotation.  $U_P$  is the average inflow velocity normal to the plane of rotation. The total resultant velocity experienced by the blade section is  $U = \sqrt{U_P^2 + U_T^2}$ .  $\theta$  is the collective angle of the blade section.  $\phi = \tan^{-1} \frac{U_P}{U_T}$  is the inflow angle and  $\alpha = \theta - \phi$  is the blade section angle of attack. From these vectors of wind velocities, the lift,  $dL$ , and drag,  $dD$ , vectors on each blade section can be estimated and added to get the resultant force  $dF_R$ . The horizontal and vertical forces,  $dF_X$  and  $dF_Z$ , are derived from breaking the resultant force vector into two orthogonal components.

For full scale helicopter blade element analysis, three simplifying assumptions are usually made. First, the inflow velocity  $U_P$  is assumed much smaller than  $U_T$ , so that  $U$  is approximated equal to  $U_T$ . Second, the induced inflow angle  $\phi$  is assumed

small, so that  $\phi \approx U_p/U_T$ ,  $\sin \phi \approx \phi$ , and  $\cos \phi \approx 1$ . Third, the drag is at least one order of magnitude smaller than the lift, so the vertical contribution due to drag,  $dD\sin\phi$ , is negligible compared to the vertical contribution due to lift [53]. In order to achieve an accurate model of rotor forces from blade element analysis, an assumption must be made for the inflow distribution. The initial estimate of inflow will utilize the previous three assumptions.

The blade element momentum theory combines the blade element theory and the momentum theory to predict inflow and load for each blade element. This type of analysis can be utilized to predict an inflow distribution for any rotor geometry. During the blade element momentum model used for the current analysis, the rotor disk is broken up into 20 concentric annuli, such as the one shown in Figure 32, and the blades are analyzed as 20 corresponding elements.

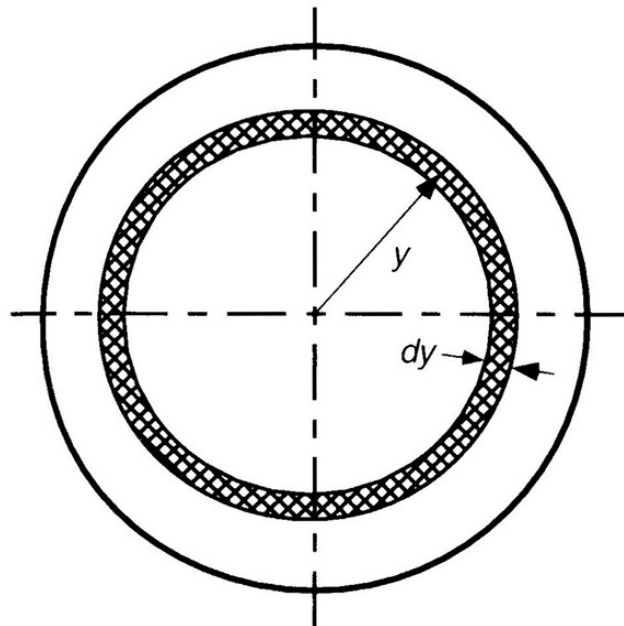


**Figure 32: Annulus used for momentum theory analysis [53]**

The thrust on each element and annulus is described separately by blade element theory and by momentum theory. The rotor has  $N_b$  number of blades with a chord of  $c$ . In blade element theory, the thrust,  $dT$ , and thrust coefficient,  $dC_T$ , are based on the equation for blade element lift,  $dL$ . The blade section is operating at a lift coefficient of  $C_l$ . Using the simplification  $r = \frac{y}{R} = \frac{U}{\Omega R}$  and incorporating solidity  $\sigma = \frac{N_b c}{\pi R}$ , the basic equation for the thrust coefficient in the blade element theory is derived:

$$dL = \frac{1}{2} \rho U^2 c C_l dy$$

$$dT = N_b dL = N_b \frac{1}{2} \rho U^2 c C_l dy$$

$$dC_T = \frac{N_b \frac{1}{2} \rho U^2 c C_l dy}{\rho (\pi R^2) (\Omega R)^2}$$

$$dC_T = \frac{1}{2} \sigma C_l r^2 dr$$

The momentum theory solution for thrust is the change in momentum flow through each rotor annulus. The change in momentum flow across each rotor annulus is the mass flow,  $d\dot{m}$ , multiplied by the induced velocity,  $v_i$ , multiplied by two. The factor of two is due to the rotor wake contraction, which causes the axial flow in the free wake to be two times the axial inflow at the rotor disk [53, 56]. The inflow ratio is  $\lambda = v_i / (\Omega y)$ , where  $v_i = U_P$  in a steady state with no blade flapping. The derivation of the thrust coefficient in hover proceeds as follows:

$$\begin{aligned}
d\dot{m} &= 2\pi\rho v_i y dy \\
dT &= 2v_i d\dot{m} \\
dT &= 4\pi\rho v_i^2 y dy \\
dC_T &= \frac{4\pi\rho v_i^2 y dy}{\rho\pi R^2 (\Omega R)^2} \\
&= 4 \frac{v_i^2}{(\Omega R)^2} \left(\frac{y}{R}\right) d\left(\frac{y}{R}\right) \\
&= 4\lambda^2 r dr
\end{aligned}$$

The inflow for each rotor element is estimated by equating the two interpretations for  $dC_T$  from the blade element model and the blade element momentum model. With the identity  $\lambda = \phi r$  and recalling  $\alpha = \theta - \phi$ , and  $C_l = C_{l_a} \alpha$ , the two equations can be combined into a quadratic equation and solved as follows:

$$\begin{aligned}
dC_T &= \frac{1}{2} \sigma C_l r^2 dr = \frac{\sigma C_{l_a}}{2} (\theta r^2 - \lambda r) dr \\
dC_T &= 4\lambda^2 r dr \\
4\lambda^2 r dr &= \frac{\sigma C_{l_a}}{2} (\theta r^2 - \lambda r) dr \\
4\lambda^2 &= \frac{\sigma C_{l_a}}{2} (\theta r) - \frac{\sigma C_{l_a}}{2} (\lambda)
\end{aligned}$$

$$\lambda^2 + \frac{\sigma C_{l_a}}{8} (\lambda) - \frac{\sigma C_{l_a}}{8} (\theta r) = 0$$

$$\lambda(r) = \frac{\sigma C_{l_a}}{16} \left( \sqrt{1 + \frac{32}{\sigma C_{l_a}} \theta r} - 1 \right)$$

The only unknown in this solution is the lift curve slope,  $C_{l_a}$ . In a full scale

helicopter rotor analysis, the lift curve slope is 5.7/rad. For Reynolds numbers on the order of  $10^4$ , however, the lift curve slope is generally about 10% less, verified by CFD data and experimental data of airfoils and wings [16, 17, 18, 20]. Utilizing the lift curve slope to estimate the inflow is a method that is only valid below stall, where the lift curve is linear. Especially when the angle of attack of the blade element reaches into the nonlinear region of the lift curve, the inflow model depends on the actual element vertical force.

The vertical and horizontal forces on each blade element are calculated by finding the angle of attack and corresponding lift and drag. The lift and drag coefficients for a specific airfoil are most accurately found directly from a table of the airfoil data. For this particular hover analysis, it only makes sense to choose an airfoil that performs well at this Reynolds number, such as a thin cambered plate. Lift and drag data from Sunada et. al. [18] and Okamoto and Azuma [37] for thin cambered plates at low Reynolds numbers are compiled in Figure 33. The separate data both describe a 5% thick plate cambered 9%. The test labeled “Azuma” was completed at a Reynolds number of 7600 in a wind tunnel. The test labeled “Sunada” was done in a water tunnel at a Reynolds number of 4000. The solid lines are a piecewise fit, utilized by the present rotor analysis so that the lift and drag are both calculated as functions of angle of attack.

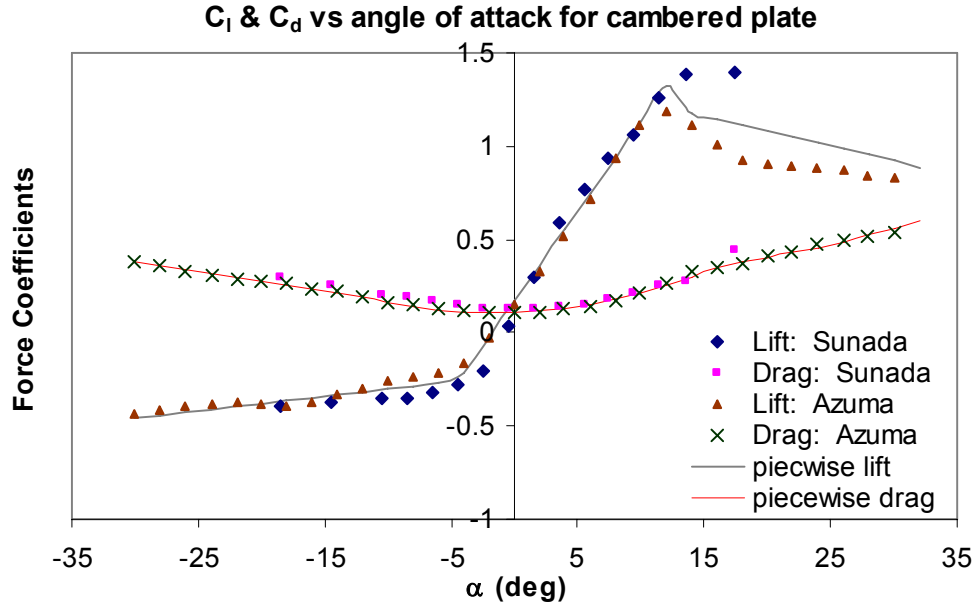


**Figure 33: Cambered plate force coefficients at low Reynolds number [18, 37]**

From this point forward, when calculating the thrust, drag, and inflow of the rotor elements, the forces and velocities are resolved into vertical and horizontal forces as shown in Figure 31. The vertical component of the drag is taken into account in the thrust calculation, even though it is usually neglected in full scale predictions. The forces on each blade element are multiplied by the number of blades, to get the total vertical force,  $dF_Z$  and the total horizontal force,  $dF_X$ , for each rotor section:

$$dF_Z = N_b (dL \cos \phi - dD \sin \phi)$$

$$dF_X = N_b (dL \sin \phi + dD \cos \phi)$$

This is where the current prediction differs from conventional rotor analysis. Using a part of momentum theory usually applied to the analysis of a propeller, there is also an angular velocity component of the inflow,  $v_{sw}$ , which is a direct result of the

torque of the rotor. The torque required for each rotor section,  $dQ$ , is equivalent to the change in angular momentum through the rotor annulus multiplied by the annulus radius. The angular momentum of the inflow at the rotor disk is half of its value in the far wake downstream of the rotor, just as the vertical inflow at the rotor disk is half the far wake value [57, 58]. This leads to the momentum theory results for the swirl velocity and the torque. The torque can also be described in terms of the horizontal force,  $dF_X$ , multiplied by the element radius,  $y$ . The equation relating  $dF_X$  and swirl velocity then simplifies to the same form as the relationship between the thrust and the vertical inflow:

$$dQ = 2v_{sw} y d\dot{m} = 4\pi\rho v_i v_{sw} y^2 dy$$

$$dF_X = 4\pi\rho v_i v_{sw} y dy$$

$$\frac{dF_X}{4\pi\rho v_i v_{sw} y dy} = \frac{dF_Z}{4\pi\rho v_i^2 y dy}$$

The momentum theory determines that the square of the vertical inflow velocity,  $v_i^2$ , is directly proportional to the vertical force on each rotor annulus,  $dF_Z$ . Likewise, the swirl velocity multiplied by the inflow velocity,  $v_{sw}v_i$  is directly proportional to the horizontal force,  $dF_X$ . The swirl velocity can then be calculated in terms of the inflow velocity:

$$\frac{v_i}{dF_Z} = \frac{v_{sw}}{dF_X}$$

$$v_{sw} = v_i \frac{dF_X}{dF_Z}$$

When analyzing full scale rotors, the swirl velocity is easily neglected because

it is at least an order of magnitude less than all other wind velocities. For MAV rotors with lower tip speeds, lower lift to drag ratios, and higher thrust coefficients, the swirl velocity can perceptively reduce the blade element velocity due to rotation,  $U_T$ . For the case of the current MAV rotor prediction,  $U_T$  is directly reduced by the swirl velocity, so that:

$$U_T = \Omega y - v_i \frac{dF_x}{dF_z}.$$

The vertical force for each rotor element is used to recalculate the vertical inflow and the horizontal force is used to calculate the swirl inflow based upon the momentum theory result. The inflow velocities are then used to recalculate the blade element forces. This iterative process is repeated until the inflow estimate changes less than 2% from one iteration to the next. The values for vertical inflow, swirl velocity, thrust and torque usually converge within a few iterations.

After the inflow is finalized for each rotor annulus, a tip loss factor is introduced. The tip loss factor accounts for some of the 3-D effects near the rotor tips, which are dominated by tip vortices. This correction factor has the effect of increasing the inflow velocity near the blade tips without increasing the rotor thrust. The equations utilized for tip loss calculations were described by Prandtl and Betz [59], later modeled by Goldstein [60] and Lock [61] and further simplified by Leishman [53] for helicopter applications. The inflow “correction factor”,  $F$ , decreases as the blade element radial position increases.  $F$  is a function of the inflow and the radial position of each blade element. Since the inflow depends on  $F$  and vice versa, the calculation is carried out iteratively as follows:

$$f = \frac{N_b}{2} \left( \frac{1-r}{r\phi} \right)$$

$$F = \left( \frac{2}{\pi} \right) \cos^{-1} e^{-f}$$

$$\lambda = \frac{\sigma C_{l_\alpha}}{16F} \left[ \sqrt{1 + \frac{32F}{\sigma C_{l_\alpha}} \theta^*} - 1 \right]$$

The inflow is derived from equating the thrust from blade element theory to the thrust from momentum theory. The inflow estimate and tip loss factor are functions of the lift curve slope, which means this estimate is less accurate at high angles of attack. Only for the purpose of the tip loss estimation, the inflow is artificially limited to a maximum value. As the collective increases, if the thrust of the blades is no longer increasing, the tip loss does not increase. The series of equations converges within a few iterations. The final step is adding the forces of the blade elements to calculate the total rotor thrust, torque, and figure of merit. These calculations are done for each collective angle.

$$\begin{aligned} \text{Thrust } T &= \sum_{n=1}^{20} dF_{z_n} \\ \text{Torque } Q &= \sum_{n=1}^{20} dF_{x_n} y_n \\ \text{Power } P &= \Omega Q \end{aligned}$$

$$\begin{aligned} C_T &= \frac{T}{\rho A (\Omega R)^2} \\ C_P &= \frac{P}{\rho A (\Omega R)^3} \end{aligned}$$

$$\text{Figure of Merit } FM = \frac{\text{ideal power}}{\text{actual power}} = \frac{C_T^{\frac{3}{2}}}{C_P \sqrt{2}}$$

### 3.2.2 Flapping and Rotation

For adding flapping motion, a time component,  $t$ , is introduced into the model. The total time period of analysis is equivalent to one blade flapping cycle, broken into 100 steps. The blade flapping is assumed sinusoidal at a frequency of  $\omega_F$  radians per second and an amplitude  $\beta_{\max}$ , so that the flapping angle is  $\beta = \beta_{\max} \sin \omega_F t$ . Each blade section has a vertical position and velocity due to flapping:

$$\begin{aligned} h_F &= y \sin \beta_{\max} \sin(\omega_F t) \\ V_F &= \omega_F y \sin \beta_{\max} \cos(\omega_F t) \end{aligned}$$

The vertical velocity is also called the heaving velocity. A downward heaving velocity causes an upward wind velocity, which increases the blade section angle of attack. Under the conditions seen in Figure 34, the resultant force on the blade section tilts in a forward direction and the drag force contributes to the vertical force. At this instant of downward heaving, the blade section is producing a propulsive force

and is producing a vertical force that is greater than the sectional lift. With high frequency blade flapping, the heaving motion is an order of magnitude larger than the inflow velocity, so the inflow velocity is not shown separately in this figure. The inflow velocity is not ignored in the calculations, however. The vertical velocity component becomes  $U_p = v_i + V_F$ . This change propagates throughout the model, starting with  $\phi = \tan^{-1} \frac{U_p}{U_T}$ .

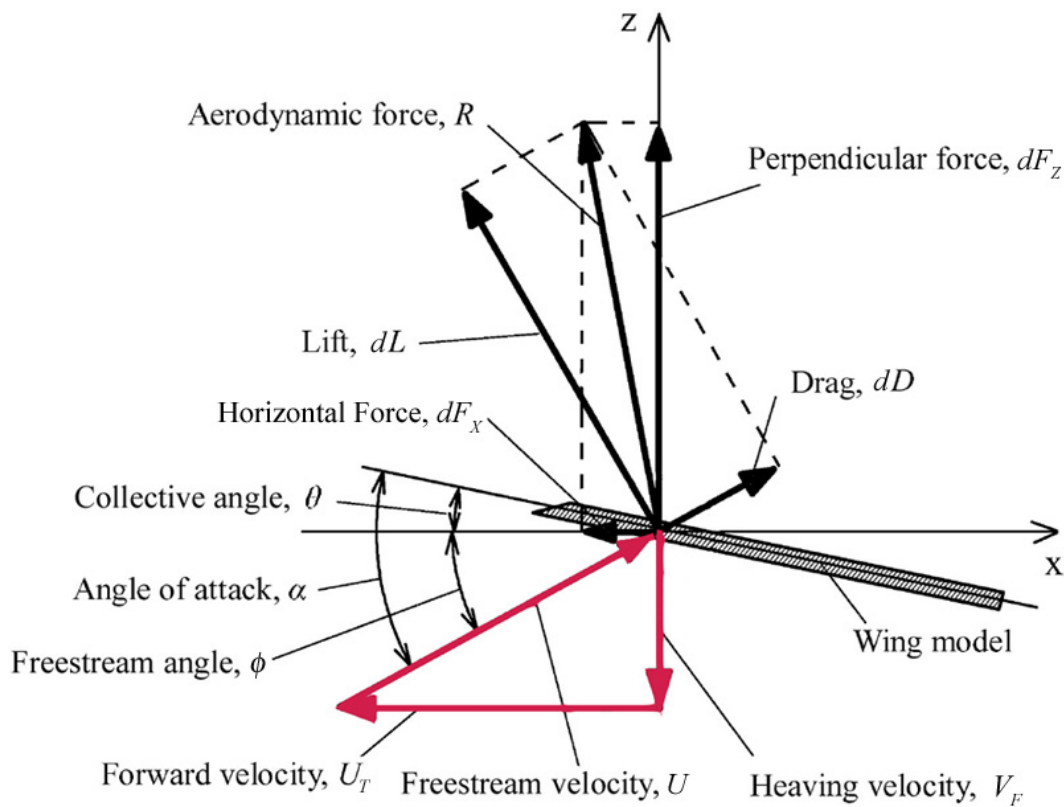


**Figure 34: Plunging blade section vector analysis**

Making a couple of interim assumptions, it can be shown that the freestream angle variation and therefore the angle of attack variation is approximately constant across the span of the blade. The maximum and minimum freestream angle occurs

when the heaving velocity is also at its maximum and minimum. The heaving velocity is approximately  $V_F = \omega_F y \sin \beta_{\max} \cos(\omega_F t)$ , so the maximum heaving velocity is  $V_{F_{\max}} = \omega_F y \sin \beta_{\max}$ . Ignoring the swirl velocity, the forward velocity is approximately  $U_T = \Omega y$ . The maximum freestream angle becomes:

$$\phi_{\max} = \tan^{-1} \frac{V_{F_{\max}}}{U_T} = \tan^{-1} \frac{\omega_F y \sin \beta_{\max}}{\Omega y}$$

$$\phi_{\max} = \tan^{-1} \frac{\omega_F \sin \beta_{\max}}{\Omega}$$

Therefore, the approximate maximum freestream angle depends only on the flapping frequency, the flapping amplitude, and the hub rotation speed. It should remain relatively constant across the span of the blades.

There is an option in the model so that the blades can be fundamentally modeled as flexible. A “twist factor” is introduced that alters the blade element angle of attack depending on the blade element load. Since the blade element forces depend directly on the angle of attack, the angle of attack simply becomes a fraction of its previous value, depending on the twist factor.

The blade element analysis of the forces, velocities, and angles are calculated the same as the conventional rotation case except for the inflow. The inflow velocity,  $v_i$ , for each blade element and collective angle is borrowed from the non-flapping case and is assumed constant with time. Since the forces from this flapping case are time varying, they are averaged to compare them with the results from the conventional rotation case.

## 4 Experiment, Results, and Discussion

The experiments with the Flotor exploited three types of independently controlled motion. The first motion tested was powered flapping motion of flexible blades with a freely rotating main rotor shaft. The second motion was conventional powered rotation, which could be compared with previously published data from similar experiments. The third and final group of tests combined simultaneous powered rotation and powered flapping motions of stiff blades. Because of the many variables and configurations possible with the test apparatus, the variables were narrowed by applying rational constraints to hold constant as many variables as possible. Each set of tests is presented with its own variables and constraints.

### 4.1 Powered Flapping With Free Hub Rotation

In the tests utilizing flapping with free shaft rotation, the variables included blade design, flapping frequency, and flapping amplitude. The hub rotation speed was purely a function of these three variables as it trimmed itself for a constant speed with zero rotor torque. The first tests with the Flotor were conducted with the apparatus in the configuration as seen in Figure 35. The only motor in this configuration was the flapping motor, which was a Hacker B20 26L brushless motor with 4:1 planetary gearhead. The brushless design required the use of an electronic speed controller. To control the speed of the flapping motor, the speed controller was input a pulse signal from a GWS adjustable pulse generator and servo tester. The

flapping motor speed was varied manually by modulating the pulse width output from the GWS pulse generator. The amplitude of flapping was fixed by the distance of an offset pin in the flywheel of the flapping motor. For this test, the amplitude of flapping was  $\pm 17^\circ$ , which does not include blade flexibility.

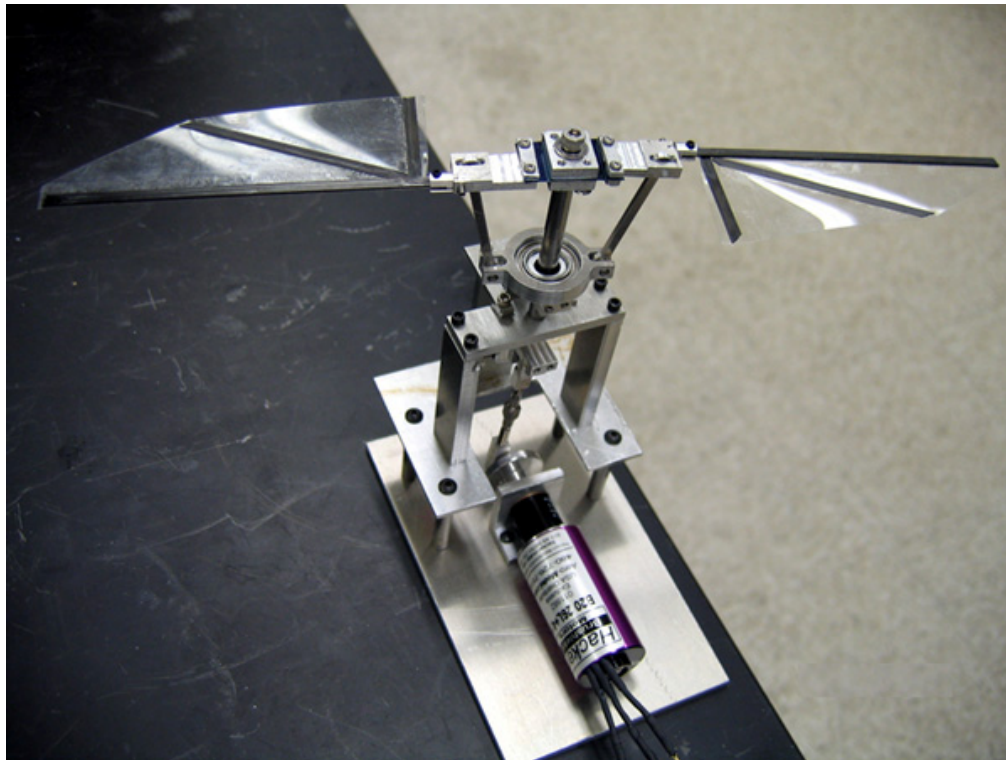


**Figure 35: Flapping rotor with freely rotating hub**

For the free rotation of the rotor to be self-starting, it was necessary for the blades to pitch into the relative wind when they started flapping. Therefore, the blades had to be flexible with the elastic axis located in front of the aerodynamic center of pressure. There are four basic cases that can be used to demonstrate the necessity for this type of flexibility: rigid blades at zero collective, rigid blades at positive collective, flexible blades at zero collective, and flexible blades at positive collective. All of the cases show the forces on a flat plate blade element assuming

the rotor is not rotating and the only motion is blade flapping.

The first two cases of rigid blade flapping with zero and positive collective are shown in Figure 36. The actual velocity of this blade element due to flapping is  $V_F$ , which means the only wind velocity is  $-V_F$  in a vertical direction. The blade element is shown at the point of maximum velocity during the downstroke and upstroke of flapping, assuming that the rest of the blade motion is symmetric. At zero collective, the angle of attack on the blade is  $90^\circ$  during the downstroke and the upstroke. A flat plate at  $90^\circ$  angle of attack produces only a drag force. The drag force during the downstroke and the upstroke is equal and opposite and therefore averages to zero. In an inviscid fluid, there is no force in the plane of rotation during the upstroke or downstroke at zero collective.

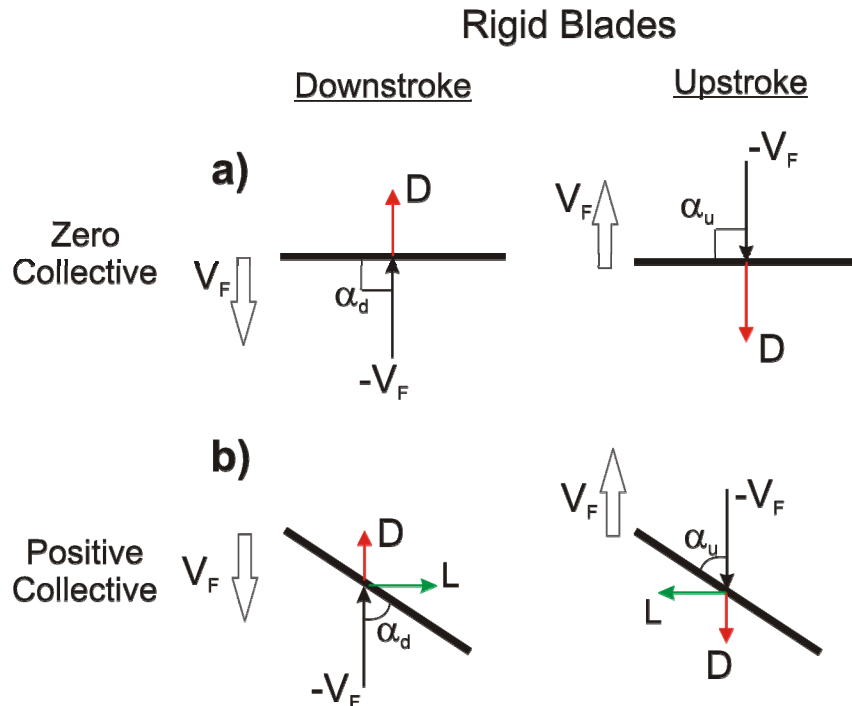


**Figure 36: Flapping rigid flat plate blades at a)  $0^\circ$  collective and b) Positive collective**

At positive collective, the rigid blade has an angle of attack less than  $90^\circ$  during the downstroke, producing a lift force in the plane of rotation. The lift force on the upstroke and the downstroke is equal and opposite, however, and averages to zero. The drag forces are also equal and opposite. Therefore, flapping rigid flat blades at any collective angle should not produce a net force in any direction and should not cause the rotor to start rotating.

The example of blades flexible about their leading edge is shown in Figure 37. These blades are assumed to have their elastic axis, marked “ea”, at their leading edge, which ensures that aerodynamic forces cause the blade to pitch into the relative wind during flapping. With zero degrees average collective, the aerodynamic force pitches the blade so that it has an equal angle of attack during the upstroke and the downstroke. The drag force during the upstroke and downstroke is equal and opposite and therefore averages to zero net vertical force. The lift force, however, is in the same direction during the downstroke and upstroke, producing a net force in the plane of rotation. This net force accelerates the rotation of the rotor. At a positive collective angle with flapping flexible blades, the angle of attack on the downstroke is always greater than the angle of attack on the upstroke. In the figure, the downstroke is shown with nearly  $90^\circ$  angle of attack, producing no lift in the plane of rotation, but producing a high vertical drag force. During the upstroke, the blade pitches to a much more acute angle of attack, producing a high lift in the plane of rotation and relatively little drag in the vertical direction. In this case, the lift averages to a net force in the plane of rotation while the drag averages to a net vertical thrust.

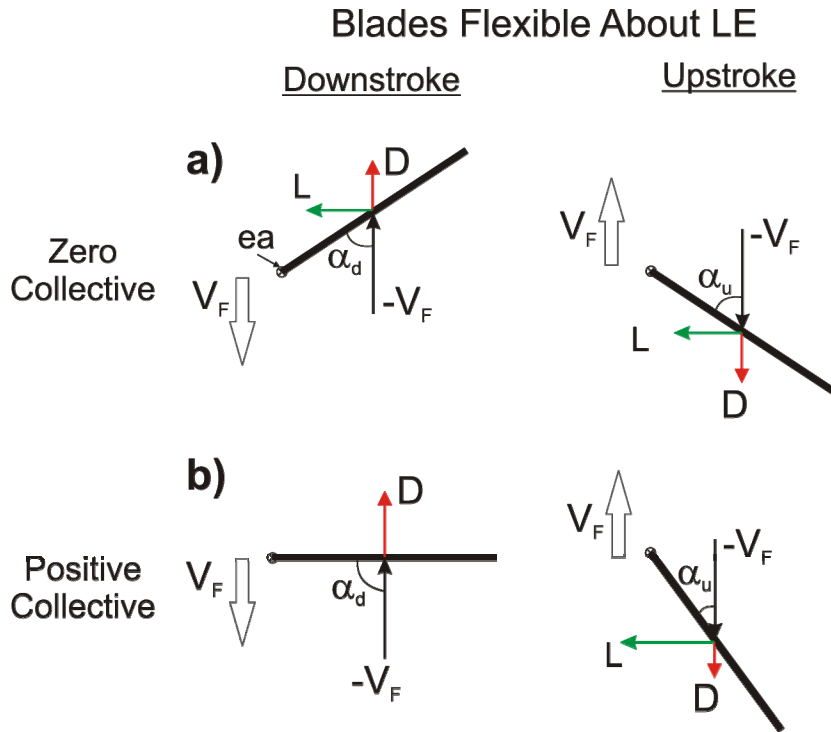


**Figure 37: Flapping flat plate blades flexible about their leading edge at a) 0° collective and b) Positive collective**

To ensure the forward location of the elastic axis, the blades for the experiment were manufactured with a leading edge spar that is an order of magnitude stiffer than the rest of the blade. The blades, shown in Figure 38, were manufactured out of three beams of pre-cured unidirectional carbon/epoxy composite bonded to a 0.25 mm thick sheet of mylar. The carbon beams have fibers running in their lengthwise direction. The leading edge spar is the stiffest beam, with a length of 8.35 cm, thickness of 0.65 mm and a width of 2.95 mm. The root end of the leading edge spar is attached to the hub by securing 0.45 cm of material into the blade grips. The two supporting element beams are more flexible due to their reduced dimensions of 0.25 mm thick and 2.9 mm wide. The supporting element perpendicular to the leading edge spar is 2.85 cm long. The diagonal supporting element is positioned at

an angle of  $22^\circ$  from the leading edge and extends to the trailing edge at 60% blade span.

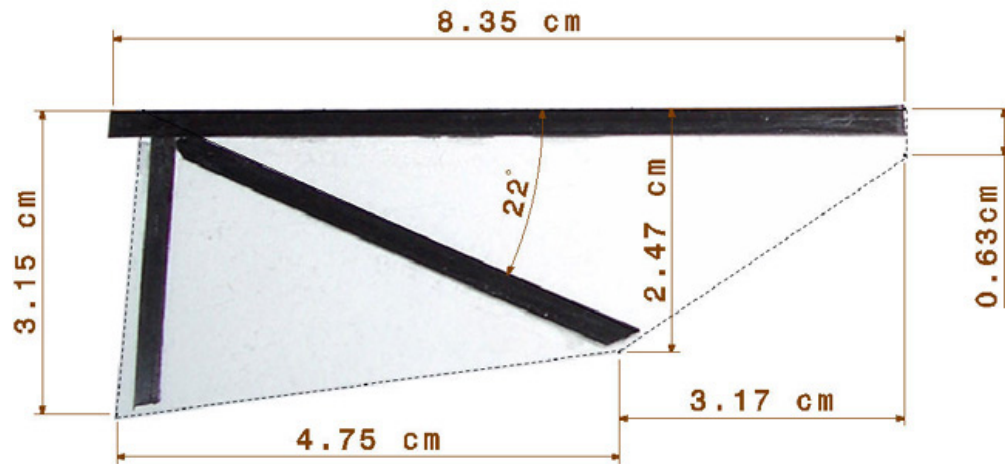


**Figure 38: Blade 1 Dimensions**

The blades used for this test have a lifting surface with a length of 7.92 cm. Including the root cutout, which is 30% in this case, the rotor radius is 10.95 cm. There are two linear taper ratios incorporated into the blades. The first taper ratio is 14% and extends from the root to 60% span. The second taper ratio of 55% extends from the 60% span to the tip, which gives the blades a shape representative of a bat of similar size [44]. The root chord of a blade is 3.15 cm, the chord at 60% span is 2.47 cm, and the chord at the tip is 0.63 cm. The total area of both blades is  $39.5 \text{ cm}^2$ , or  $0.00395 \text{ m}^2$ , which does not include the root cutout of the rotor.

The purpose of the first test was only to demonstrate the concept of passive hub rotation with powered flapping. The variables in this test were blade collective angle and the blade flapping frequency. The collective angle and flapping amplitude were measured with a bubble type inclinometer. The flapping amplitude was

measured by manually positioning the flywheel for maximum positive and negative deflection and taking measurements at each position. The flapping amplitude was fixed at  $\pm 17^\circ$ , or  $34^\circ$  peak to peak. In the first test, the collective was varied from  $0^\circ$  to  $15^\circ$  to  $30^\circ$ .

The speed of the flapping motor was varied between 26 and 43 Hz, or 1600 and 2600 RPM. The rotational speeds of the hub and flapping motor were both measured with a Monarch Instruments light sensitive tachometer. Two strips of reflective tape were placed  $180^\circ$  apart on each rotating part. The tachometer works by emitting a beam of light pointed at the reflective tape, which reflects back to the tachometer. The tachometer was calibrated to count two pulses of light for each rotation to display the proper rotational speed.

This first set of results proved that the hub can rotate freely due to the aerodynamic forces of the flapping blades, even when the blades are at high collective angles. The results gathered during this proof of concept test were preliminary and are shown in Figure 39. At  $0^\circ$  collective, the hub rotation varies from 170 to 525 RPM as the flapping varies from 28 to 43 Hz. At  $15^\circ$  collective, the hub rotation varies from 190 to 500 RPM as the flapping speed varies from 27 to 43 Hz. At  $30^\circ$  collective, the hub rotation varies from 290 to 550 RPM as the flapping speed varies from 27 to 43 Hz. The ratio of hub rotation speed to flapping speed is not constant. With the blades at  $15^\circ$  collective, the ratio of hub rotation to flapping speed increases with increased flapping speed at every data point. At  $0^\circ$  and  $30^\circ$  collective, the ratio increases at all but the highest flapping speed. At  $30^\circ$  collective, the hub rotation speed is highest for every flapping frequency.

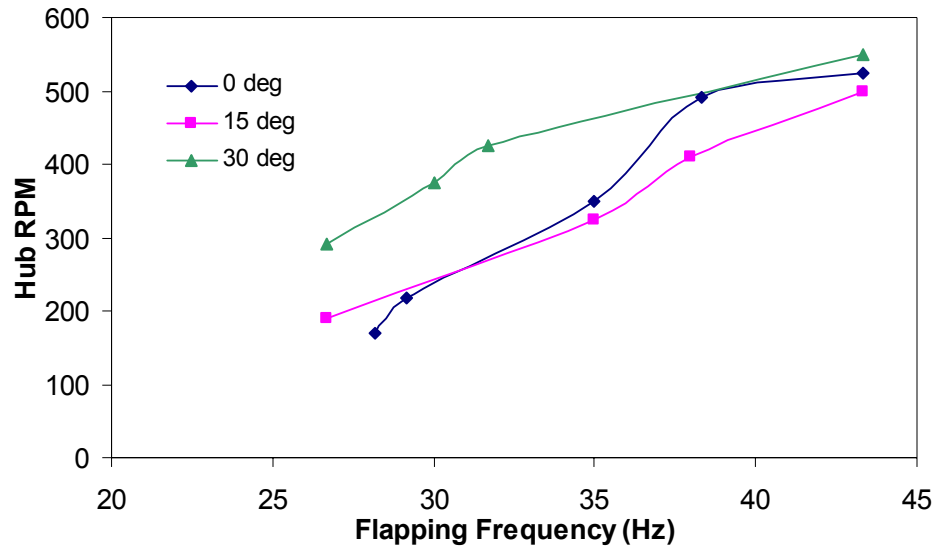


**Figure 39: Hub RPM vs. Flapping Frequency**

At the highest rotational speeds of 550 RPM, the  $\frac{3}{4}$  chord of the blades is reaching airspeeds of approximately 4.5 m/s. Compared to similarly sized flying creatures, the blade velocity in this configuration falls short of its target. The obvious trend in this data shows that increasing flapping frequency is related to increasing the hub rotation speed. The flapping frequency in this case was limited by the forces of the reciprocating parts on the measurement equipment. The test stand was mounted upon a thrust cell which had a maximum capacity of 1 kg, so the total calculated inertial forces of all reciprocating parts was kept below 1 kg force.

The first average data from the thrust cell is shown in Figure 40. The data was gathered to ensure all components of the Flotor as well as the instrumentation for data acquisition functioned properly. Although preliminary, these results showed increasing thrust with increasing flapping frequency at every data point. The thrust increases with increasing collective up to 30°, but beyond 30° no further thrust increase occurred.

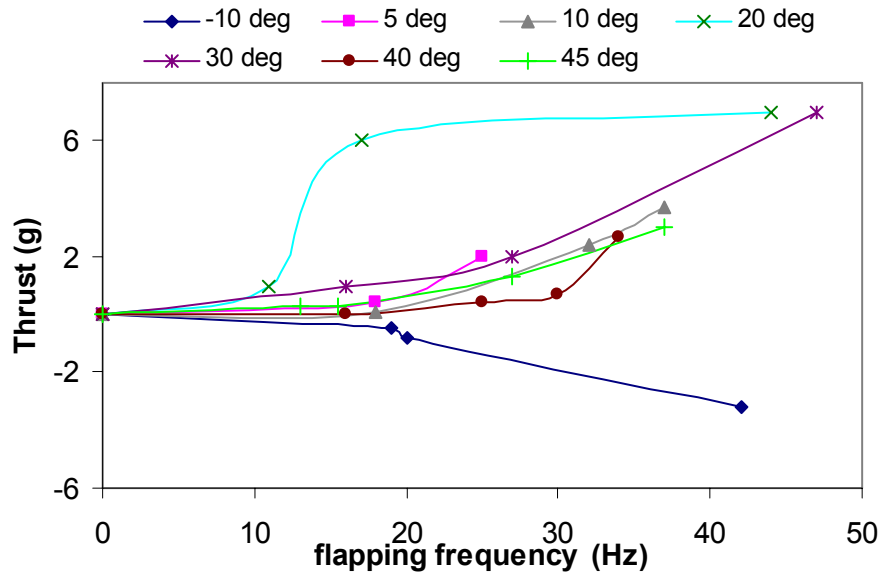


**Figure 40: Thrust vs. Flapping Frequency for various collectives**

In order to measure the vertical forces from the rotor, multiple configurations to gather the time varying thrust data were attempted but none were successful. Since the inertial loads due to flapping are orders of magnitude greater than the aerodynamic forces, it is a very difficult task to differentiate the instantaneous aerodynamic loads from inertial forces. However, since the average inertial forces are nearly zero, an average signal will contain only the aerodynamic force. Therefore, only the average forces were measured during the remainder of the experiments. To measure the average thrust, the test stand was mounted to an Ohaus Explorer digital balance. The balance incorporates a feature which uses a low pass filter while averaging the force for five seconds to display the result. It eliminates the periodic flapping forces. This feature, which is normally used for measuring the weight of active live animals, has proven very useful and accurate for measuring the average aerodynamic forces of the Flotor.

Instead of a manual tachometer, the flapping motor and rotor hub were instrumented with sensors to monitor their rotation. The RPM data was gathered with National Instruments hardware and software. The signals from the sensors were fed through SCC modules in a SC-2345 Carrier. The carrier provided power to the modules and also interfaced with a computer through a 6062E data acquisition card. The computer ran LabVIEW software for data acquisition. This setup monitored inputs and provided power output. The power output in this case was also used to power the sensors that monitor rotational speeds.

To ensure low friction, a system of magnets and hall sensors was devised so that no contact with the rotating parts is necessary to measure their speed. Because of the small size of the rotating parts, the magnets had to be small and relatively powerful to activate the hall sensors. Neodymium rare earth magnets were selected with a length and width of 1/8" and a depth of 1/16". Two of the magnets were bonded 180° apart on the flapping motor flywheel and two were mounted 180° apart on the rotor hub. Honeywell SS443A hall effect sensors were mounted close enough to the rotating magnets so that the magnets passed within a few millimeters of the face of the sensors. This model of sensor is unidirectional, so it was important that the proper pole of each magnet faced the sensor as it passed. The sensor was powered by a constant 10 V from the data acquisition module. The output from the sensor is a "sinking" output, so the LabVIEW software was written to count one rotation for every two drops in voltage from the sensor output.

The next test was the first that simultaneously incorporated measurements of hub speed, flapping speed, and thrust. The rotor was operated in this case at a fixed

collective of  $15^\circ$ , which previously showed relatively high thrust levels and hub rotation with the aforementioned blades. The flapping frequency was varied between 17 and 38 Hz.

Similar to the previous test, the hub RPM again increased non-linearly with blade flapping frequency. Figure 41 shows the hub rotating speed compared to the blade flapping frequency. As the flapping frequency increased from 16 to 38 Hz, the rotor hub speed nearly quadrupled from 150 RPM to 550 RPM. Figure 42 shows the ratio of hub to flapping speed versus the flapping frequency. This shows that as the flapping frequency doubled, the ratio of hub rotation to flapping frequency nearly doubled as well.

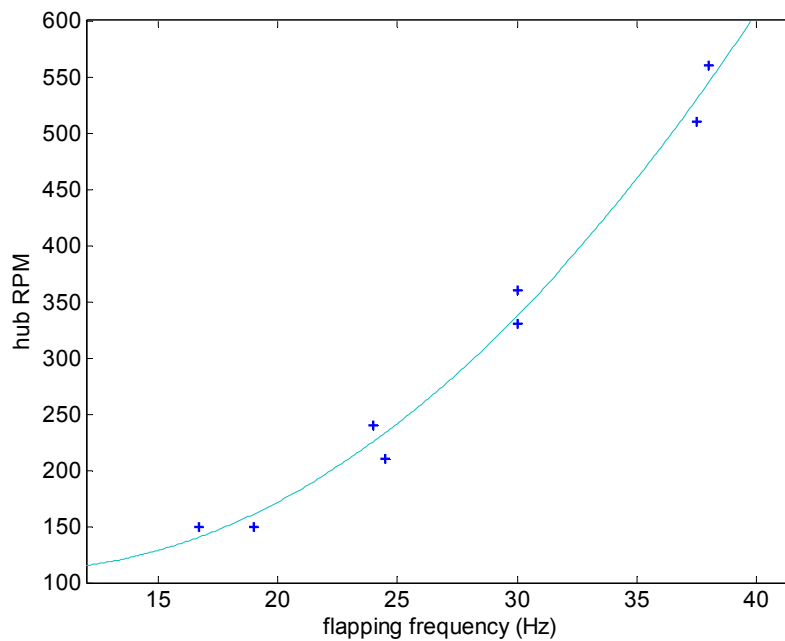


**Figure 41: Hub RPM vs. flapping frequency for  $15^\circ$  collective**

Figure 43 combines the thrust and hub RPM into a thrust coefficient, which is plotted versus flapping frequency. The thrust coefficient increases by 40% from 16 to

32 Hz flapping frequency. At higher flapping frequencies, the thrust coefficient  $C_T$  levels off and even decreases slightly at the highest flapping frequency. These thrust coefficients are on the order of two times as much as the thrust coefficients on a full scale rotor.

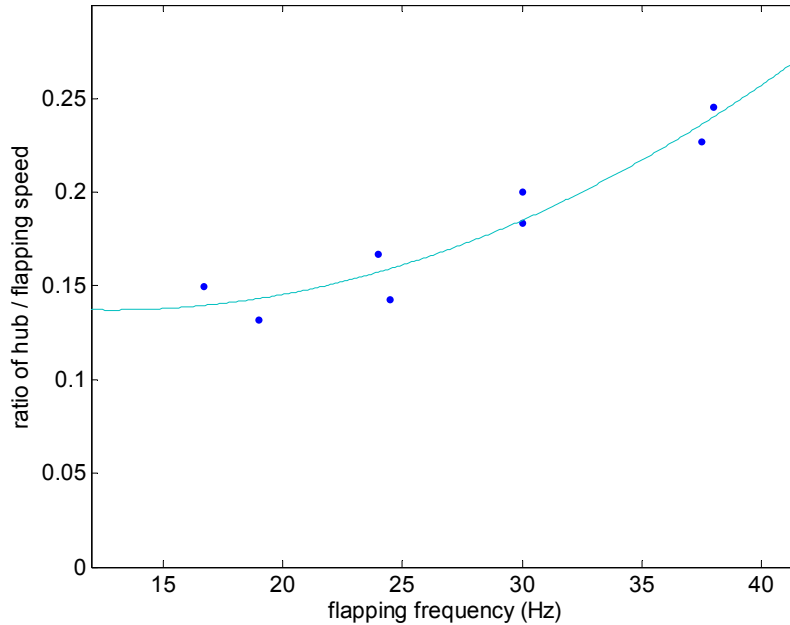


**Figure 42: Hub speed ratio vs. flapping frequency for 15° collective**

Increased flapping frequency also increases the rotational speed of the rotor hub. Increasing the rotation speed of a conventional rotor at a certain collective has no effect on the thrust coefficient. In this case at 15° collective, however, the thrust coefficient increases with increasing rotational speed, as seen in Figure 44. This increase shows that the blades are achieving vertical thrust by means other than steady hub rotation. This thrust due to flapping increases the total thrust as flapping frequency increases.

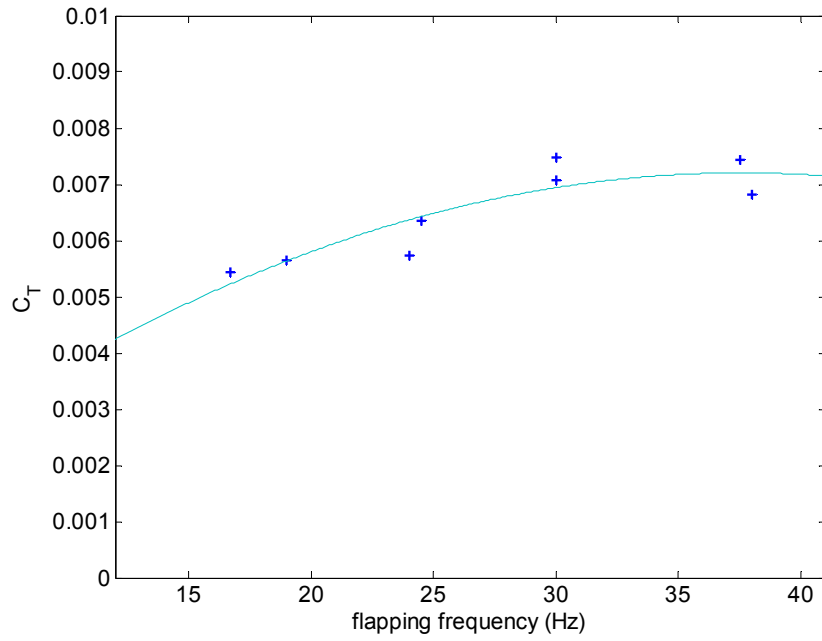


**Figure 43: Thrust coefficient vs. flapping frequency at 15° collective**

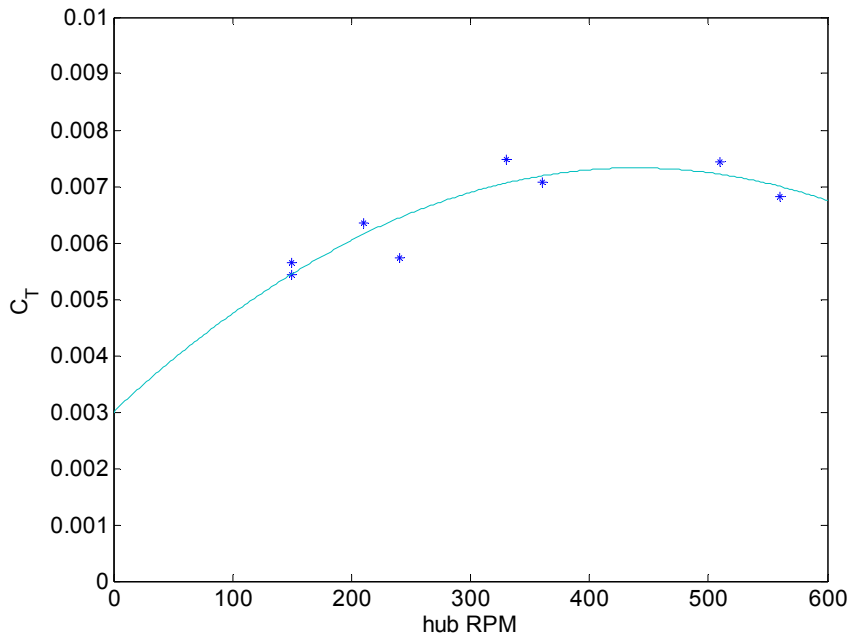


**Figure 44: Thrust coefficient vs. hub RPM at 15° collective**

Because of the low tip speeds of the Flotor and most MAVs, the average blade

loading of the Flotor is far below that of full scale helicopters. The highest thrust during this test was about 4 g, corresponding to a blade loading of about  $10 \text{ N/m}^2$ , which falls exactly in the range of bats of similar size [45].

During the previous test, a torque cell was added to measure the instantaneous torque of the flapping motor. The rear of the torque cell was mounted rigidly and the front of the torque cell was mounted to the flapping motor, which was suspended by ball bearings. Any torque produced by the flapping motor was transferred through the torque cell, then recorded by the data acquisition system. The torque for a case with 32 Hz flapping is shown in Figure 45. For each flapping cycle, there should be two torque peaks, one while accelerating the flapping mechanism upward and one while accelerating the mechanism downward. The torque peak during the upward acceleration should be greatest, since it is opposite in direction from gravity. This explains the largest peaks in the torque signal. The aerodynamic contribution to the torque signal at this frequency and amplitude is on the order of  $0.001 - 0.01 \text{ Nm}$ . This magnitude is barely distinguishable in the total torque reading. In any case, the aerodynamic torque should peak  $90^\circ$  after the mechanical torque because the aerodynamic forces vary with flapping velocity while the mechanical torque varies with flapping acceleration.

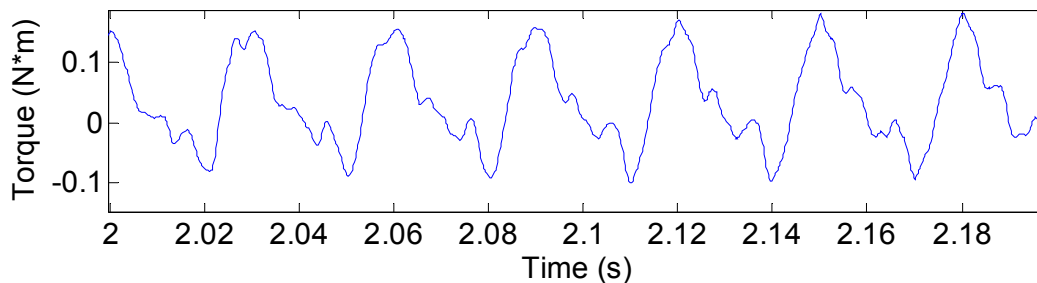
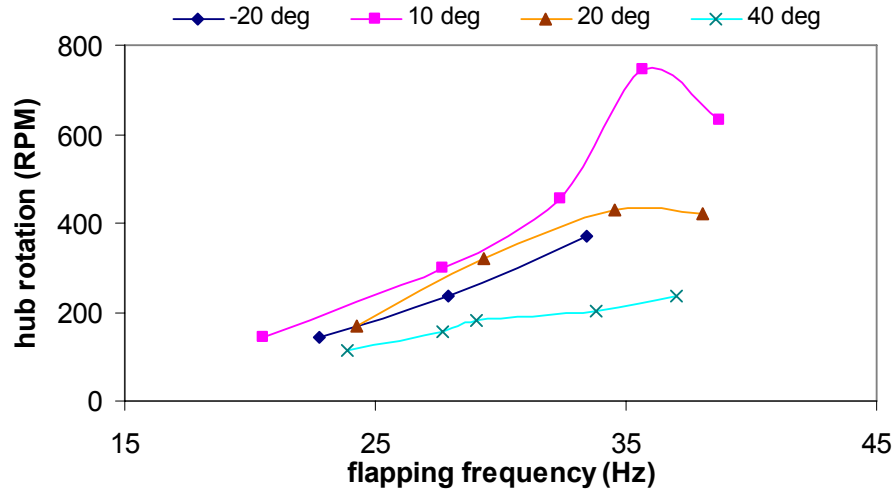


**Figure 45: Torque vs. Time for 32 Hz Flapping**

During the next test, the hub configuration was changed slightly to reduce friction. The single ball bearing that was previously mounted in the hub was replaced with two ball bearings. Even so, the two bearings were difficult to align since they were pressed into holes in two separate parts. After this test, the bearings were relocated to the base of the shaft, where their outer rings were pressed into opposite sides of a single hole and the shaft pressed through the center.

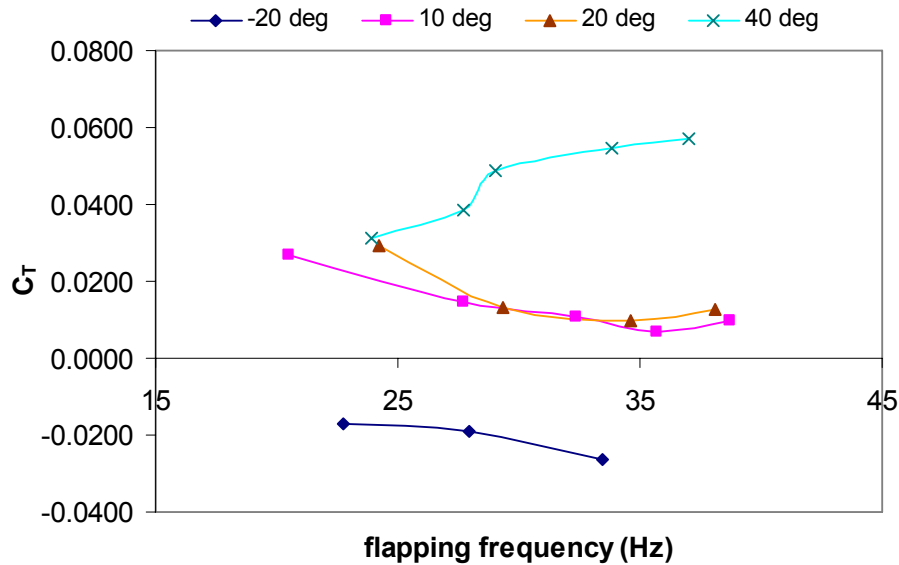
The flapping frequency was varied from 20-39 Hz at collective angles of  $-20^\circ$ ,  $10^\circ$ ,  $20^\circ$ , and  $40^\circ$  and the shaft was free to rotate. In order to determine the thrusting of the blades with zero rotation, two tests were done with the shaft rotation locked. One test was done at  $20^\circ$  and another at  $40^\circ$  with only vertical flapping and no other motion. In these tests, the blades flapped in a vertical plane with the same range of frequencies. The flapping amplitude was  $34^\circ$  peak to peak.

Each data point shown in this test is an averaged data point of five tests of the same conditions. Rotation speed data from the test with blade flapping and free hub rotation is shown in Figure 46. The hub rotates the fastest at  $10^\circ$  collective at all flapping frequencies. The hub rotation with the blades at  $-20^\circ$  collective is very similar to the hub rotation with the blades set at  $20^\circ$  collective. At  $40^\circ$  collective, the rotation speed is the slowest at every flapping frequency. The hub rotation again increases at a greater rate than the flapping speed except at the highest flapping frequencies.



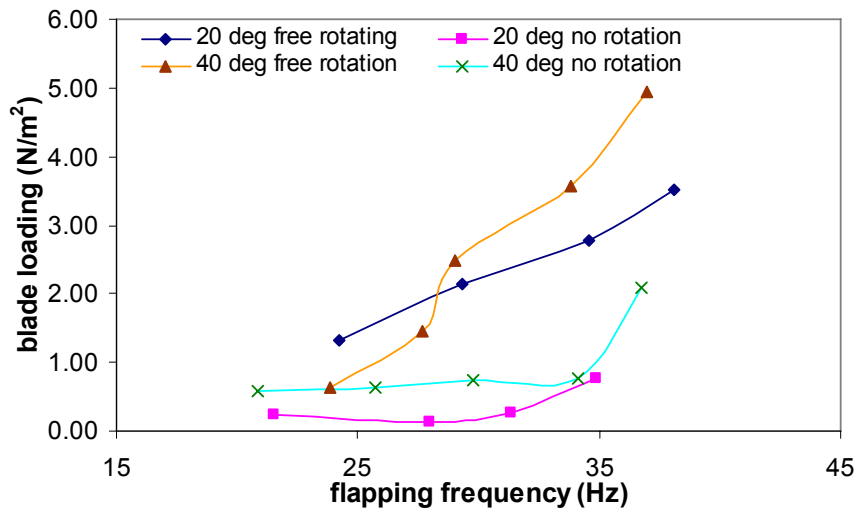
**Figure 46: Hub rotation vs. flapping frequency at different collectives**

Figure 47 shows the thrust coefficient versus flapping frequency for different blade collectives. At moderate collective angles, the thrust coefficient decreased with flapping frequency because of its inversely proportional relationship to the square of hub rotation. The absolute thrust increased, however, due to the increased hub rotation and because a portion of the thrust was produced by blade flapping.



**Figure 47: Thrust coefficient vs. flapping frequency at different collectives**

Even though the thrust coefficients may decrease with increased flapping frequency, the absolute thrust values increase with increased flapping frequency. The absolute values of thrust are shown in terms of blade loading, which is plotted against flapping frequency in Figure 48. In the data labeled “no rotation”, the thrust is due to only flapping with the shaft rotation locked. The results help to explain why, in the previous figure, the 40° collective thrust coefficient increases with increased flapping frequency. The thrust from flapping without rotation at 40° collective is up to 40% of the thrust of flapping with free rotation. In the 20° collective case, however, less than 20% of the overall thrust can be attributed to the blade flapping. The majority of the thrust in the moderate collective cases comes from hub rotation.



**Figure 48: blade loading vs. flapping frequency with rotation and with no rotation at 20° and 40° collective**

The results in all of the previous tests maintained clear trends at all but the highest flapping frequencies. When the flapping frequency reached well above 30 Hz, it was observed that the blades were undergoing extreme deformations. Apparent trends that appeared at lower frequencies, such as increased hub rotation and

increased thrust with increased flapping frequency, changed as the flapping frequency reached above 35 Hz. It was thought that stiffer blades would produce a more predictable behavior at higher flapping frequencies.

The composition of the next blades can be seen in Figure 49. There is a leading edge spar and a rectangular blade section attached to the spar with a clear mylar hinge. The material chosen for the leading edge spar was the same unidirectional carbon epoxy as the previous blades. The leading edge hinge behaves like a spring during flapping. The blade material itself was constructed to be relatively stiff compared to the previous blades while maintaining light weight. The blade surface is made of 2 layers of carbon epoxy prepreg weave laid at  $\pm 45^\circ$  with respect to the leading edge. This gives the blade fairly stiff properties in both the spanwise and chordwise direction as well as high torsional stiffness. The blade has a length of 7.62 cm and a chord of 1.78 cm, giving the two blades a total blade area of  $27.1 \text{ cm}^2$ , or  $0.0021 \text{ m}^2$ . The blades give the rotor a total radius of 10.2 cm.

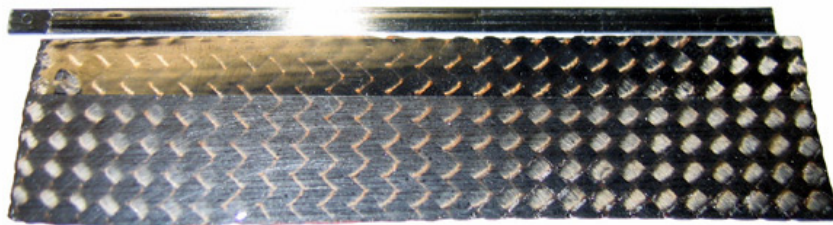
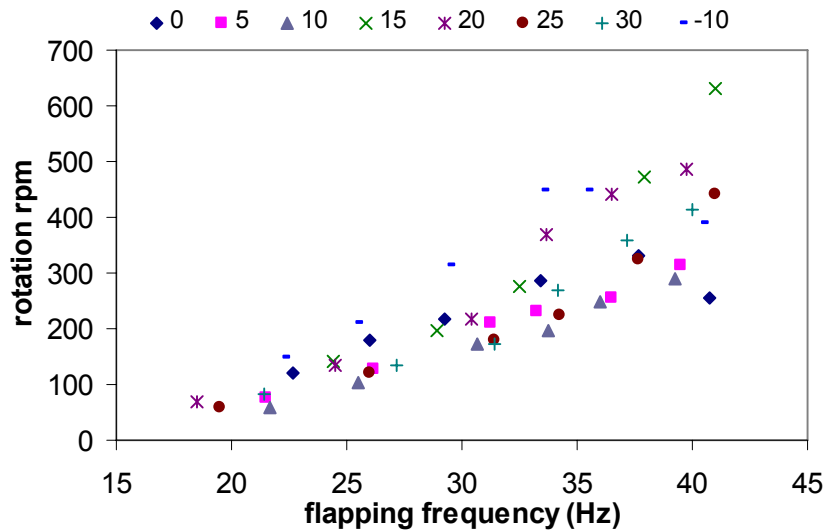


**Figure 49: Carbon blade with flexible leading edge hinge**

These blades were tested at collective angles ranging from  $-10^\circ$  to  $30^\circ$  and at flapping frequencies from 19 to 41 Hz. The collective was varied in steps of  $5^\circ$  between  $0^\circ$  and  $30^\circ$  and was also tested at  $-10^\circ$  to verify negative thrust readings. The flapping amplitude was the same as the earlier tests at a peak to peak value of  $34^\circ$ .

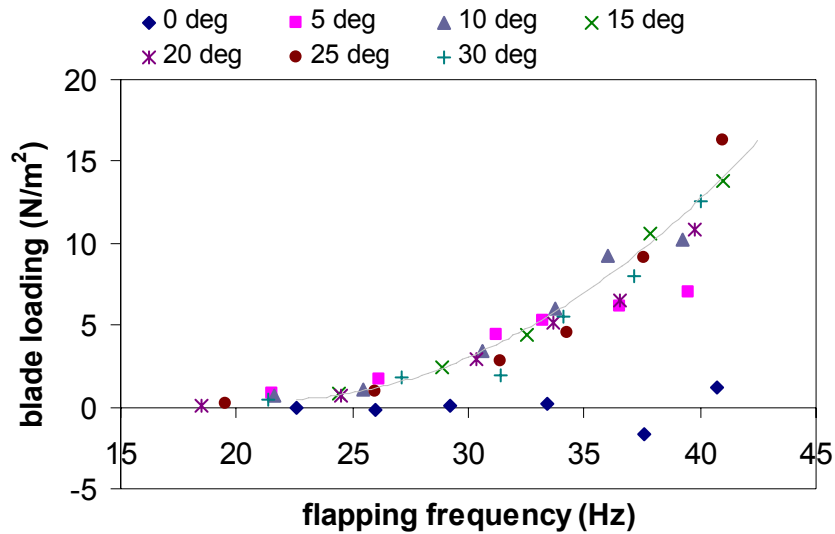
Like the previous test, each data point shown here is an average of at least three tests at the same conditions. Even with vastly different blade constructions, the results were similar to the results from the previous blade design.

Figure 50 is a compilation of the results of hub rotation speed versus flapping frequency at all collective angles. Once again, the blades reached a maximum rotation speed at 15° collective, with similar results at 20° collective. The rotation speed again increased at a faster rate than the flapping frequency. For each collective angle from 5° to 30°, the trend of increasing hub rotation rate could be described with a quadratic polynomial fit. The quadratic trends for each collective angle fit the data with a least squares fit between 0.98 and 0.999, except for 0° and -10° collective. The quadratic trend does not fit the highest flapping frequencies for 0° collective and -10° collective, because the hub rotation slowed with increasing flapping frequency at those points. For all other data points, it was a good fit.



**Figure 50: Hub rotation vs. flapping frequency for different collectives**

The absolute thrust of the Flotor is shown in Figure 51 in terms of blade loading. The thrust of the blades is highest at the maximum flapping frequency and 25° collective, even though the rotation speed at 25° collective is not the fastest. At 25° collective and 41 Hz flapping, the blades produced 18% more thrust despite rotating 30% slower than at 15° collective and 41 Hz flapping. During steady rotation without flapping, the rotor thrust varies with the square of rotation speed and is approximately proportional to blade collective angle. The rotation speed at 41 Hz flapping and 15° collective was 630 RPM. At 41 Hz and 25° collective, the rotation speed was 443 RPM. Rotating steadily without flapping at these two respective speeds, the thrust at 25° collective should be less than the thrust at 15° collective if a linear lift curve slope is assumed. Under the conditions in this test, however, the thrust at 25° collective is much greater, which means that much of the thrust at high flapping frequency and high collective has its source in blade flapping.



**Figure 51: Blade loading vs. flapping frequency for different collectives**

The thrust coefficient versus flapping frequency for all of the collective angles is shown in Figure 52. The thrust coefficient trends for 5°, 10°, and 15° collective show a decrease with increasing flapping frequency. This points to a decreasing fraction of the thrust coming from flapping as flapping frequency is increased. At low collectives and higher flapping frequencies, much of the flapping energy is going towards the rotation of the blades. At higher collective angles, however, the trend of thrust coefficient remains constant or even increases with flapping frequency. With increasing flapping frequency at higher collectives, an increasing fraction of the thrust can be attributed to blade flapping.

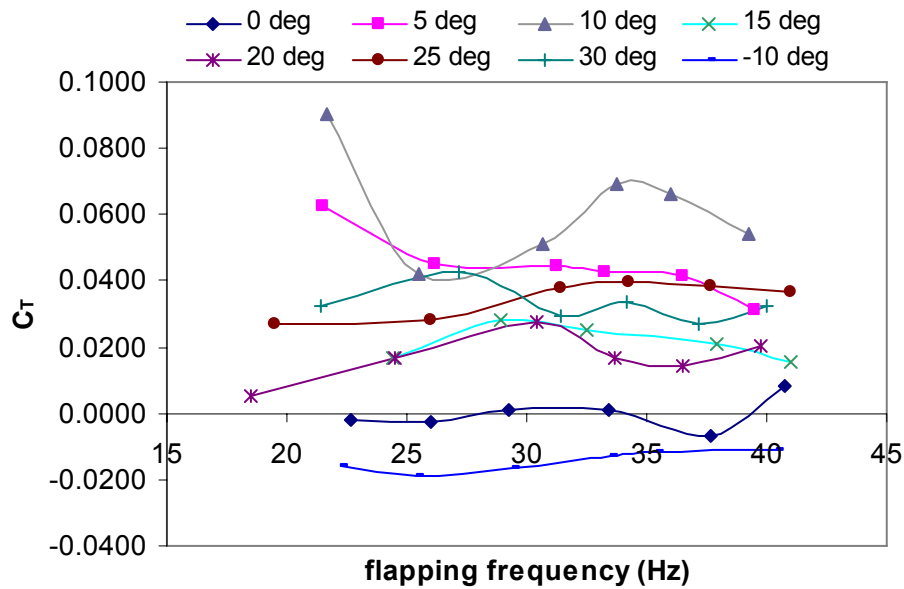
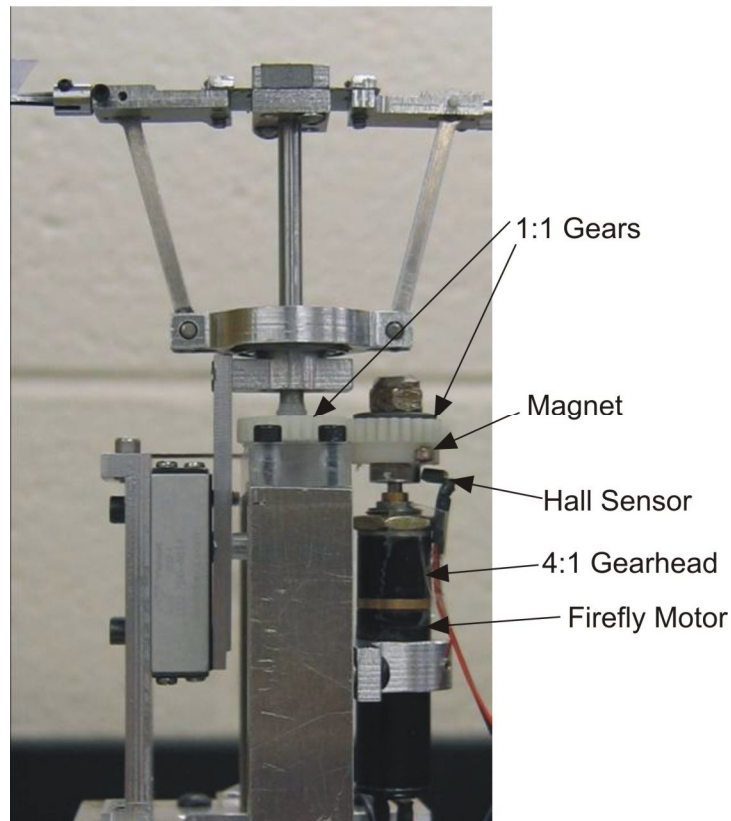


Figure 52: Thrust coefficient vs. flapping frequency at different collectives

## 4.2 Conventional Powered Rotation and Model Validation

The objective of the next set of tests was to evaluate the system efficiency of the Flotor operating as a conventional MAV rotor and compare the results to other

published micro rotor data. The first experiment was conducted utilizing powered shaft rotation. The flapping motor was not used for these tests. The rotation motor is an Astro Flight Firefly coreless DC motor with a 4:1 planetary gearhead. The output shaft from the motor gearhead drives a 1:1 gear, which drives the rotor shaft. The motor speed was monitored with the same hall sensor described earlier, which is mounted below the rotation motor output gear in Figure 53. The speed of the motor is manually controlled by varying the motor voltage from a Sorensen power supply. The power supply has a data output for current and voltage which is fed to the data acquisition system in order to monitor the electrical power consumed by the rotation motor. There was not yet a mechanism in place for measuring mechanical power, so any references to power or figure of merit in the results are based on electrical power.



**Figure 53: Rotation motor mounted with hall sensor**

The blades used for this test were carbon plates with a thickness ratio of 3%, which were molded with a camber of about 7%. Their shape was rectangular with a chord of 2 cm and a span of 8.1 cm. The rotor had a total radius of 10.8 cm. This type of blade is used in flying rotary wing MAVs because of its good performance at low Reynolds numbers. The data measured in this experiment was the hub rotation speed, the electrical power input to the system, and the vertical thrust output. The variables were the hub rotation speed and the collective angle. The collective angle was varied in steps of 5° between 0° and 25°. The hub rotation was tested from 600 to 3000 RPM in steps of 200 RPM, unless the electrical power capabilities of the motor were exceeded. For short periods, the motor was tested beyond its manufacturer recommended power limit of 10 Watts.

The results for thrust versus RPM are shown in Figure 54. The maximum recommended power of the motor is shown as a dotted line. As expected, the value of thrust increases approximately with the square of the rotor RPM. There is a small positive thrust at 0° collective because the blades are cambered and the airfoil sections produce lift even at 0° angle of attack. The greatest thrust occurred at 15° collective, but exceeded the power recommendations of the motor. If constrained to 10 Watts of power into the motor, the thrust was approximately 55 grams at 10°, 15°, and 20° collective while rotating at 2900 RPM, 2400 RPM, and 2200 RPM, respectively.

Figure 55 shows the measured electrical power compared to the rotor thrust at all of the collective angles. The collective angles of 10°, 15°, and 20° all follow a

very similar trend and all have a similar maximum thrust that is limited by the power constraint of the motor.

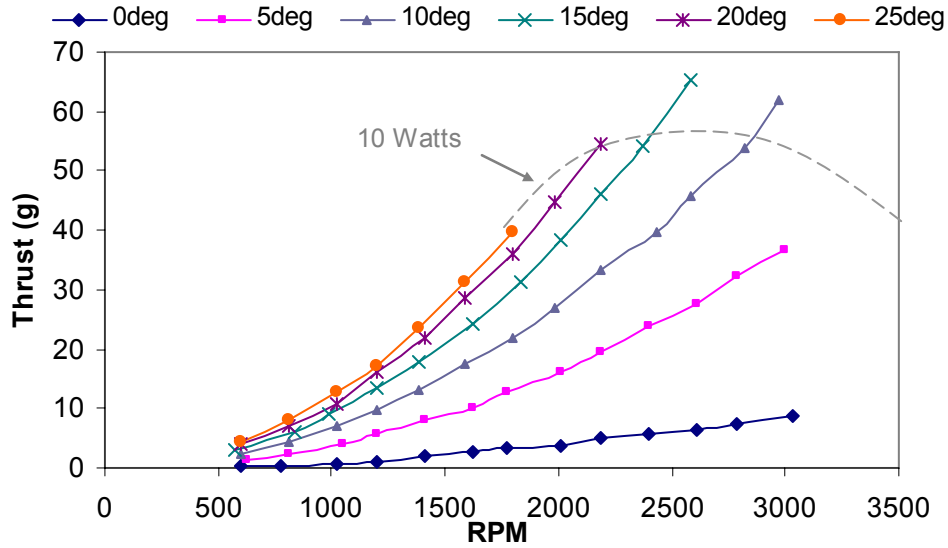


**Figure 54: Thrust vs. RPM and approximate 10 Watt electrical power limit**

At high thrust levels, the  $10^\circ$  collective case had the highest electrical power loading, since it required the least power for a given amount of thrust. To produce 54 grams of thrust at  $10^\circ$  collective, the motor required 8.8 Watts of power. To produce the same thrust at  $15^\circ$  and  $20^\circ$  collective, however, the motor required 9.6 W and 10.3 W, respectively.

The trend of thrust coefficient versus RPM is shown in Figure 56. There is a very slight increase in thrust coefficient with increasing RPM. This can be attributed mainly to Reynolds number effects, such as an increase in lift curve slope and a decrease in viscous effects with increasing rotor speed. For the most part, the thrust coefficient does not vary appreciably with RPM, therefore, the rotor speed should also not have an obvious effect on the aerodynamic figure of merit.

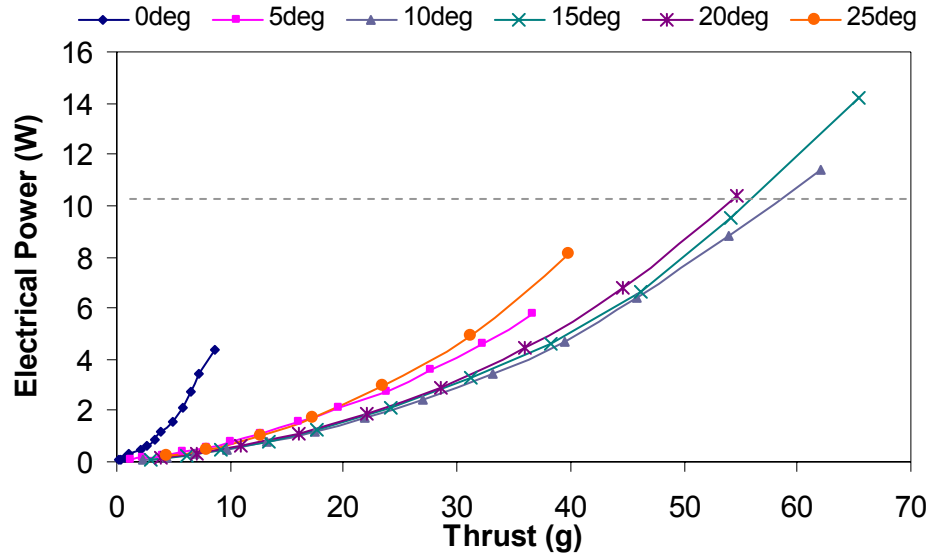


Figure 55: Electrical Power vs. Thrust for various collectives

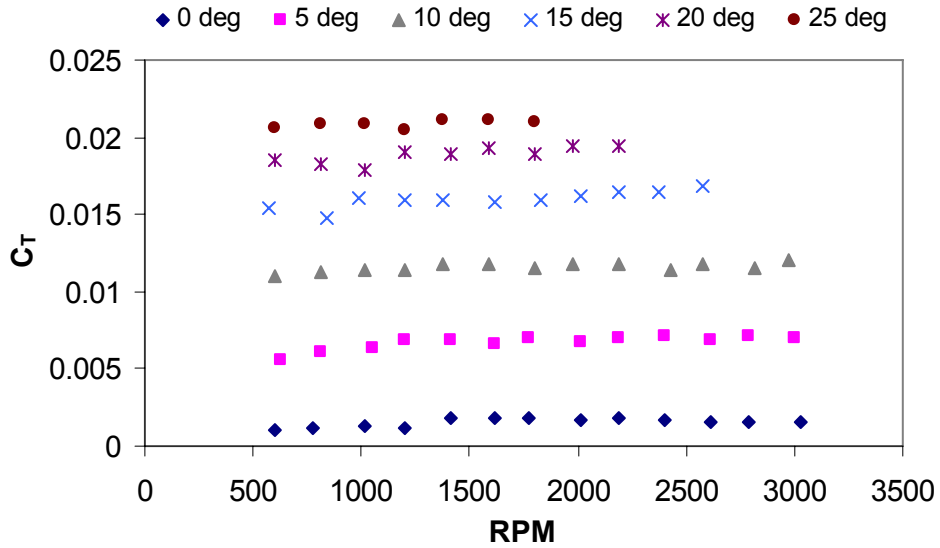
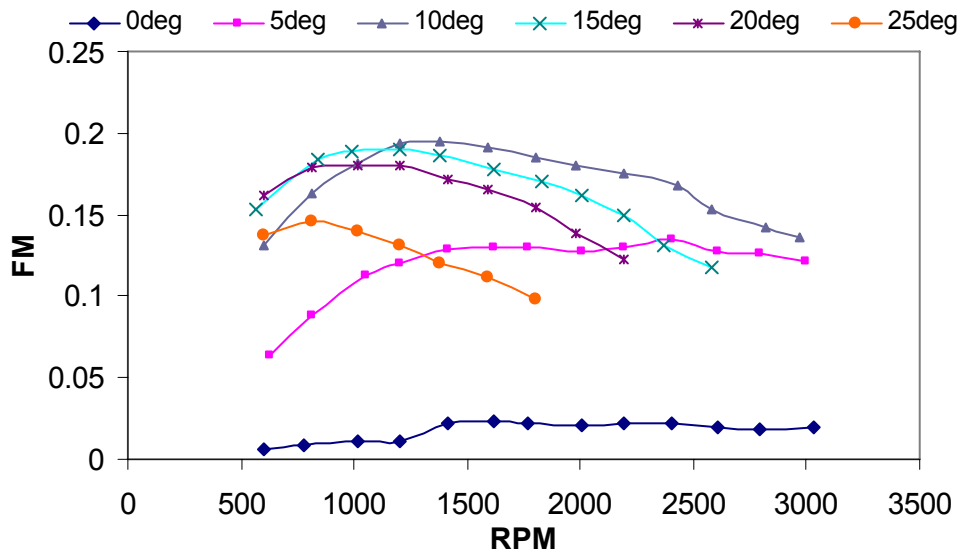


Figure 56:  $C_T$  vs. RPM for collectives between 0° and 25°

The figure of merit measured in this experiment is the total system figure of merit based on electrical power input, which is the ratio of ideal power to actual electrical power. The electrical power input into the motor includes all losses such as motor efficiency, transmission efficiency, and aerodynamic efficiency. The ideal

power is the ideal aerodynamic power based on the measured rotor thrust coefficient. At this scale, electric motors can have a maximum efficiency of about 70%, but only when operated at an ideal torque and RPM. Their efficiency under normal operating conditions is usually less. Their transmissions are about 80% efficient at this size, depending on design and reduction ratio [62]. Aerodynamically, a figure of merit of 0.6 is considered good for an MAV rotor [22, 26]. In this case, the ratio of electrical power to ideal power does not exceed 0.2. Figure of merit is plotted versus RPM in Figure 57.



**Figure 57: Electrical figure of merit vs. RPM for collectives from 0° to 25°**

For a given collective, it has already been shown that the thrust coefficient remains relatively constant with changes in RPM. As a result, the trends for each collective angle in Figure 57 can be assumed to be trends of constant thrust coefficient. The change in figure of merit with RPM is therefore not due to a change in thrust coefficient. The change in figure of merit with RPM can only be attributed

to the changing mechanical and electrical efficiency of the entire system. This particular MAV system is most efficient when rotating between 1200 and 1500 RPM with the blades at a collective angle of  $10^\circ$ , which produces a thrust of between 9 and 13 grams. In this range, the figure of merit reaches a maximum value of 0.195. At  $15^\circ$  collective, the figure of merit reaches a maximum of 0.19 when the blades are rotating between 1000 and 1200 RPM, which also produces a thrust between 9 and 13 grams. When utilized in an actual MAV, the blades are usually rotated faster to produce as much thrust as possible. At maximum power and maximum thrust, the figure of merit falls to about 0.14 at  $10^\circ$  collective, 0.13 at  $15^\circ$  collective, and 0.12 at  $20^\circ$  collective. With 10 Watts of input power, all three of these collectives produce a very similar thrust of about 55 grams at 2850, 2400, and 2180 RPM, respectively. The lower tip speeds may be desirable to reduce aerodynamic noise, but require greater torque.

The next set of tests was done to verify and compare conventional rotation results of the Flotor with previously published MAV rotor results. Since aerodynamic power measurement was part of the previously published results, a sensor was added to the Flotor test stand to measure aerodynamic torque. The sensor was a Transducer Techniques RTS-25 torque cell that was mounted directly to the base of the test stand along the axis of the rotor shaft. The full bridge circuitry of the torque cell is easily integrated into the data acquisition system through a SCC-SG04 module, which incorporates its own excitation voltage and signal conditioning amplification.

The measurements for this test included hub rotation speed, vertical thrust,

rotor torque, and voltage and current into the rotation motor. The variables for this test were RPM and blade collective angle. The blade collective was varied from  $2^\circ$  to  $36^\circ$  in steps of  $4^\circ$ . The collective sweep was completed at 660, 1000, and 1500 RPM. The thrust data was again gathered with the digital balance. The other measurements were collected with the data acquisition system, which collected data at a rate of 1000 points per second for two seconds and stored the average values to an output file. Each value shown in a plot is an average of at least three of the 2-second averaged data points.

The blades used for this trial were previously tested by Hein and Chopra [26] to perform well in low Reynolds number rotor tests. The blade cross section can be seen in Figure 58. They were 3% thick aluminum plates with 7% camber. Their leading edge was sharpened at an angle of  $15^\circ$  down with respect to the upper surface. The blades have a rectangular planform with a chord of 2 cm and a span of 6.2 cm. The total rotor radius is 8.95 cm, which sweeps a total rotor area of  $25.2 \text{ cm}^2$ .

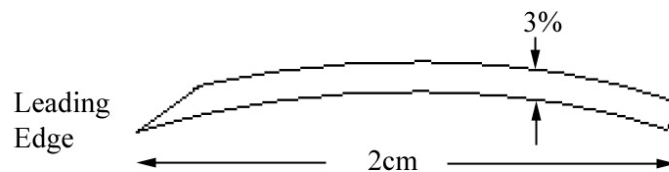


**Figure 58: Cambered plate airfoil with sharpened leading edge**

The results from the experiment are summarized in Figure 59. The previous test is from Hein and Chopra, who tested the same blades on a slightly smaller rotor with a 15.2 cm diameter. The tip Reynolds number of the Hein and Chopra test was on the order of 40,000, while the maximum tip Reynolds number during this test was

about 20,000 at 1500RPM. The thrust coefficients during these tests were at least twice as high as full scale helicopters. Part of the reason for the high thrust coefficients is that the solidity of these micro rotors is twice as high as many full scale helicopters. The effect of solidity is negated by comparing these rotors at different blade loading coefficients, or  $C_T/\sigma$ .

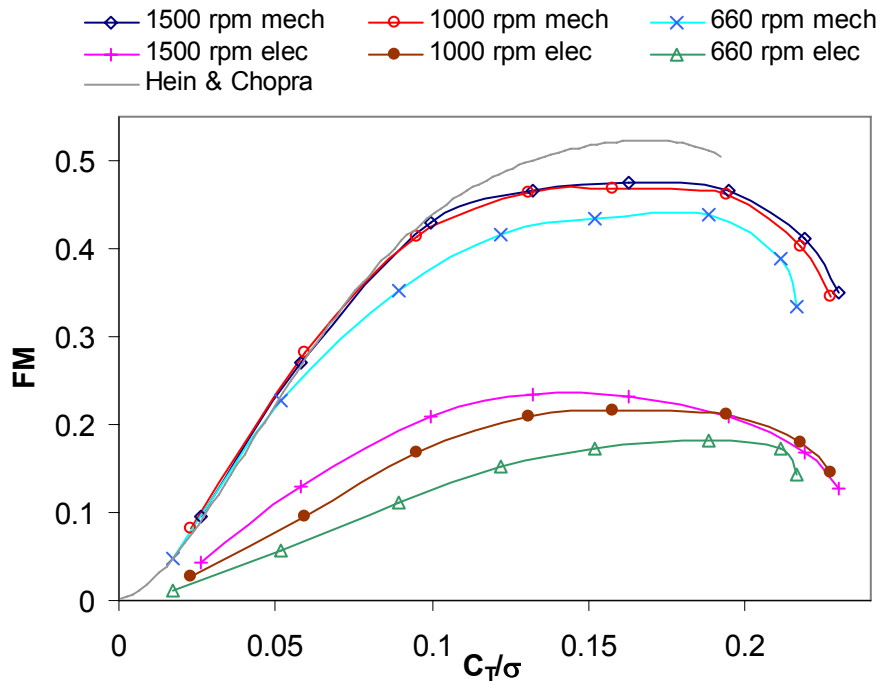


**Figure 59: Mechanical and electrical figure of merit vs  $C_T/\sigma$  compared to previous experiment**

At blade loading coefficients above 0.05, the difference in performance with varying RPM is obvious. The maximum figure of merit at 660 RPM is 0.44. The maximum figure of merit at 1000 RPM is 0.47 and the maximum in these tests is 0.48 at 1500 RPM. The maximum figure of merit reached in the tests by Hein and Chopra was 0.52. The lower figure of merit in these tests can be attributed to a couple of causes. First, the Reynolds number range of the current tests is only  $\frac{1}{4}$  to  $\frac{1}{2}$  of the

Reynolds number of the tests from Hein and Chopra. This decrease in Reynolds number causes lower maximum lift coefficients and higher drag on the blades. Secondly, the rotor hub and blade grips in these tests were designed as part of a robust flapping mechanism and they were not as streamlined as the rotor hub utilized by Hein and Chopra. Although all instruments were carefully calibrated and are accurate to within 1%, there are still differences in calibration constants that could account for a small difference between the two tests. The electrical figure of merit in these tests showed a slightly different trend than the aerodynamic figure of merit. The maximum electrical figure of merit was shifted to slightly higher blade loading coefficients. The maximum electrical figure of merit of 0.23 occurred at 1500 RPM over a range of blade loading coefficients from 0.13 to 0.16. At 1000 RPM, the electrical figure of merit peaks at a value of 0.21 at a slightly higher blade loading coefficient range from 0.16 to 0.19. The electrical figure of merit at 660 RPM has the lowest peak value of 0.18, but peaks at the highest range of blade loadings from 0.19 to 0.21.

The experimental rotor data can now be compared to the MATLAB code described earlier for predicting micro rotor performance. The blade element momentum code is based on lift and drag data for a thin cambered plate without a sharpened leading edge. This airfoil data and piecewise fit used by the code was presented earlier in Figure 33. The airfoil for the blades in the current experiment was similar, but the current blades have a sharpened leading edge. The sharpened leading edge may cause slightly less drag than the code predicts.

The experimental and predicted thrust versus collective angle is shown in

Figure 60. The rotor spinning at 660 RPM produces a slightly lower thrust coefficient at all collectives than when spinning at 1000 or 1500 RPM. The code prediction fits the experimental data extremely well at 660 RPM rotation and below 20 degrees collective, possibly because the 660 RPM test is closest in Reynolds number to the airfoil data used in the prediction.

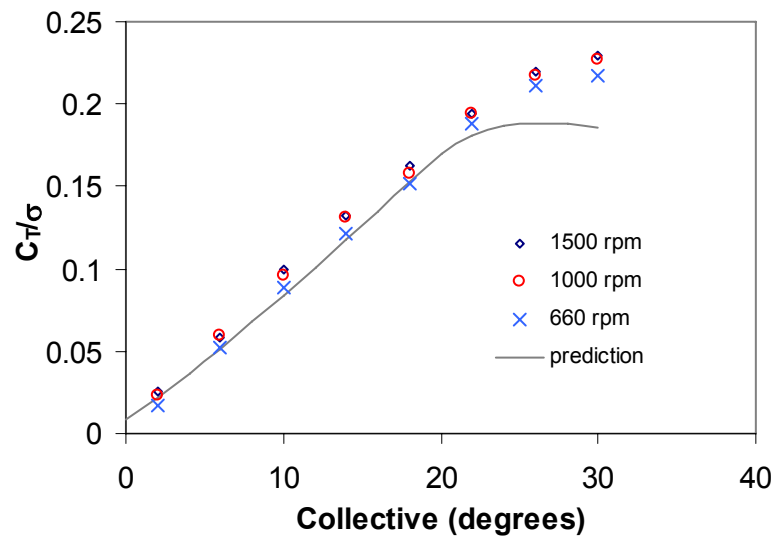
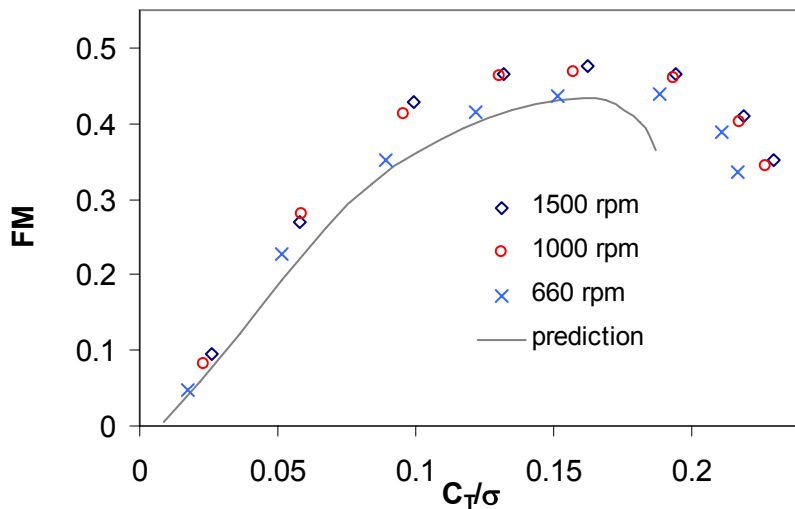


**Figure 60:  $C_T/\sigma$  vs. collective for different RPMs and prediction**

In the experiment, the thrust coefficient increases linearly with increasing collective angle up to  $22^\circ$ . The model predicts the thrust coefficient will no longer increase at a constant rate beyond  $21^\circ$  collective, less than a 5% difference from the experiment. The model, however, predicts a maximum thrust coefficient that is 15% less than the experimental data at a similar Reynolds number. The Flotor operating as a conventional rotor achieved higher thrust coefficients at higher collectives than predicted by the BEMT model. Similar findings were discovered by Bohorquez [4] with a combined CFD and BEMT model. He showed experimentally that a MAV

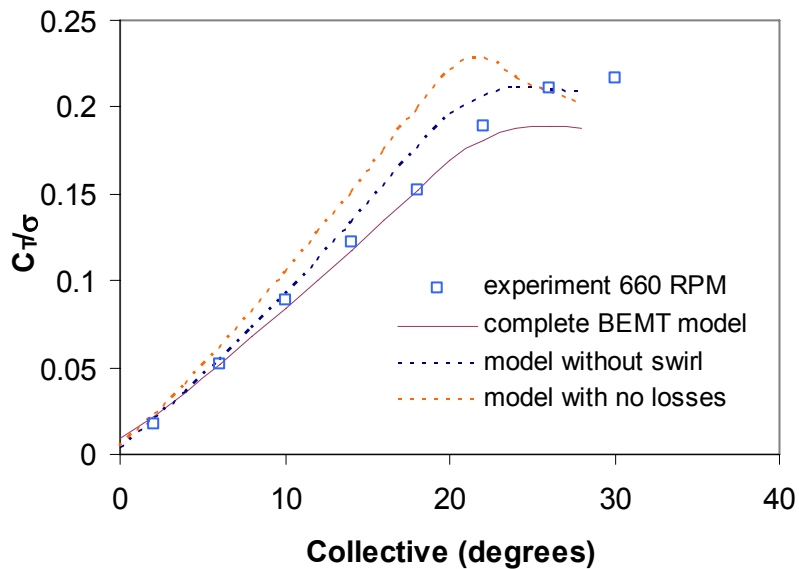
rotor stalled more gradually and reached thrust coefficients up to 10% higher than predicted by a BEMT model utilizing CFD generated airfoil data.

Figure 61 shows the experimental data and the predicted trend for figure of merit versus blade loading coefficient. Compared to the data at 1000 and 1500 RPM, the model underpredicted the figure of merit. Compared to the data at 660 RPM, however, the model predicted the figure of merit well up to a blade loading coefficient of 0.17. The 660 RPM experiment showed a maximum figure of merit of 0.44 at 0.19 blade loading coefficient. The model predicted a maximum figure of merit of 0.43 at a blade loading coefficient of 0.17, which was only a 2% difference from the experiment. Above 0.17 blade loading coefficient, the model predicted a steep drop in figure of merit that did not occur in the experiment. These differences are attributed to factors that include the lower Reynolds numbers of the model data, the sharpened leading edge of the experimental blade, and the inability for the 2-D BEMT model to accurately predict rotor performance at high collective angles.



**Figure 61: FM vs.  $C_T/\sigma$  for different RPMs and prediction**

Three versions of the prediction for blade loading coefficient versus collective are shown in Figure 62 with the 660 RPM experimental data. The first prediction is the complete BEMT model, including a tip loss factor and swirling inflow. The second prediction is the BEMT model including tip losses, but neglecting the swirl velocity component of the inflow. The third prediction is the BEMT model without tip losses or a swirl velocity. The best fit for the data below 22° collective angle is the complete model, which incorporates the swirl component of the inflow and the Prandtl model for tip losses. Ignoring the swirl component of the inflow causes a 10% increase in the slope of the trend. Ignoring both the swirl velocity and tip losses in the model causes a 20 % increase in slope, a higher peak thrust prediction, and a more abrupt stall at a lower collective angle.



**Figure 62:  $C_T/\sigma$  vs. collective for experimental data and prediction with and without losses**

### 4.3 Powered Rotation with Powered Flapping

The next tests of the Flotor involved powered rotation combined with powered blade flapping at high frequencies. During the initial testing, measurements were taken of average thrust, flapping frequency, hub RPM and rotation motor electrical power. Motor electrical power data was input to the data acquisition system from a serial connection on the back of the Sorensen power supply. The rotational speeds were measured with Hall effect sensors monitoring magnets mounted on each of the two motor shafts. Thrust data was gathered with an Ohaus Explorer digital balance. All of these data, except for the thrust, were collected with the National Instruments hardware and software at a sample rate of 1000 points/second and then averaged over a period of two seconds. The thrust was fed through a low pass filter and averaged over a period of five seconds using the force averaging feature of the digital balance. Mechanical torque data was not yet available during these tests.

The first blades tested were flat rectangular aluminum plates with a thickness ratio of 3%. They had a chord of 2 cm and a span of 6.2 cm. The total rotor radius was 8.95 cm, which sweeps a total rotor area of  $25.2 \text{ cm}^2$  with a solidity of 0.14. The blades were rotated at 660 RPM and a tip speed of 6.2 m/s. The blade collective was varied from  $0^\circ$  to  $40^\circ$  in steps of  $4^\circ$ . The low rotational speed was chosen for two reasons. First, it closely represented the airspeed of MAV sized flying creatures. Second, it allowed higher reduced frequencies with the same absolute frequency of blade flapping. The blade flapping frequency was 4 per rotor revolution, which corresponded to an absolute frequency of 45 Hz. The reduced frequency for this test

was approximately 0.3 at the  $\frac{3}{4}$  span of the blades. The amplitude of blade flapping was  $\pm 3^\circ$ , which causes a maximum heaving velocity at the blade tips of approximately 2.6 m/s. Because of blade deformation during flapping, the angle of attack variation could not be accurately predicted.

For each RPM and collective, the blades were first rotated conventionally at the desired RPM and then flapped at the desired frequency. One data point was stored for each case. A third reading was recorded during zero rotor motion as a tare test. Any residual values from the tare test were subtracted from the values gathered while the rotor was in motion. Each data point presented in the following figure represents an average of four data points gathered under the same conditions.

The test results are shown in Figure 63. With steady rotation, the blade loading coefficient reached a maximum of 0.16 at  $36^\circ$  collective, but the thrust did not increase much beyond  $28^\circ$  collective, where the value was 0.15. At every collective angle, the blades produced greater thrust with 4/rev flapping than they did with steady rotation. Like the results in the free rotation tests, the flexible blades in this test are producing extra thrust due to flapping at all collectives. The additional thrust at collectives beyond  $24^\circ$  shows evidence of delayed stall. The thrust curve during steady rotation levels off at collectives above  $24^\circ$ . The thrust curve for the 4 per revolution flapping case, however, maintains an almost linear slope up to  $34^\circ$  collective. This produces a maximum blade loading coefficient of 0.20 at  $36^\circ$  collective, a 20% maximum thrust increase over the steady rotation case.

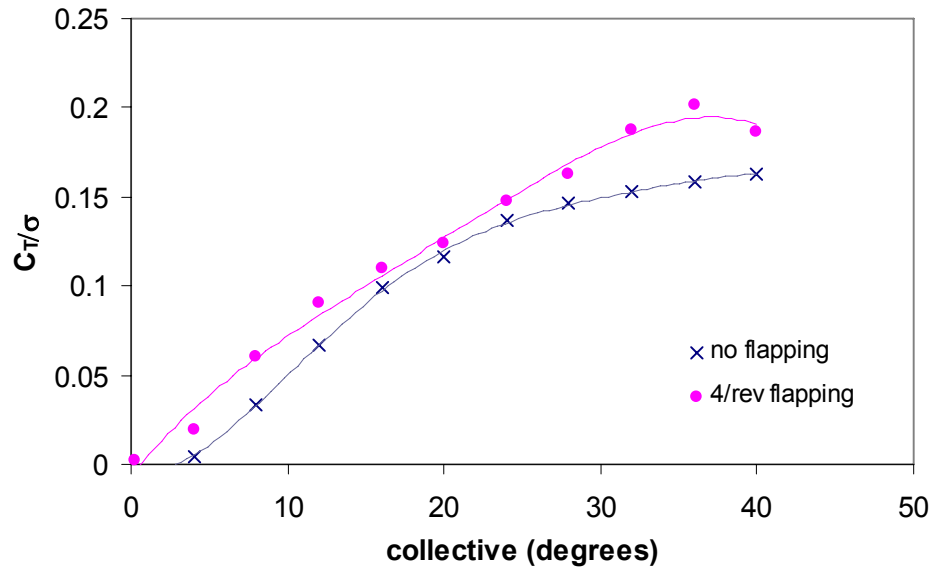


**Figure 63: Blade loading coefficient vs. collective with 660 RPM rotation and 4/rev flapping**

In order to isolate flexible blade phenomena such as rotational lift or purely rigid blade mechanisms such as dynamic stall, the remainder of the testing utilized a more rigid blade design. The blades were the same cambered aluminum plates with sharpened leading edge that were tested in the conventional rotation experiment. They have a much higher area moment of inertia than a flat plate, making them more resistant to bending and torsion than the flat plate blades in the previous test. In the remainder of the tests, the blades were rotated at 660 and 1000 RPM and the collective angle was varied from 0° to 36° in steps of 2° or 4° degrees. The blades were tested with steady rotation and with rotation plus a flapping frequency between 2 and 8 flaps per rotor revolution. The matrix of test conditions is shown in Table 1.

		Flap frequency and (amplitude)				
		None (0°)	2/rev (3°)	4/rev (1.5°)	6/rev (1°)	8/rev (0.75°)
Rotor	660 RPM	X	X	X	X	X
Speed	1000 RPM	X	X	X	X	

**Table 1: Test matrix for rotating and flapping cambered plate blades**

Since the blades in the following tests were relatively stiff, their angle of incidence variation could be estimated with rigid blade element kinematic models described in Chapter 3. The blade angle of incidence is approximately  $\phi_{\max} = \pm \tan^{-1} \frac{\omega_F \sin \beta_{\max}}{\Omega}$ . A goal was to keep the angle of incidence variation at a constant value, whether the blades were flapping at 2/rev or 8/rev. Limiting the maximum angle of incidence during flapping keeps the blades from grossly exceeding stall angle of attack values while at low collectives. The only time the blades should flap beyond their stall angle of attack is when they are set at higher collective angles of above 20°.

The maximum angle of incidence depends on flapping amplitude, flapping frequency, and rotation speed. Since the rotation speed and flapping frequencies for these tests are already constrained, the desired flapping angle can be calculated. Since the flapping will be small angles in these tests, it can be assumed that:

$$\sin \beta_{\max} \cong \beta_{\max}$$

$$\tan^{-1} \frac{\omega_F \beta_{\max}}{\Omega} \cong \frac{\omega_F \beta_{\max}}{\Omega}$$

therefore,  $\beta_{\max} \cong \frac{\omega_F}{\Omega} \phi_{\max}$

Figure 64 shows the relationship between flapping angle and flapping frequency for three different maximum angles of incidence. The goal for angle of incidence variation for these tests was chosen as approximately  $\pm 6^\circ$ . The four points on the line for  $6^\circ$  angle of incidence correspond to the four flapping frequencies presented in the next set of tests. The flapping amplitude,  $\beta_{\max}$  is varied by altering the crank radius of the flywheel on the flapping motor. The crank radius remained the same for the tests of 660 and 1000 RPM at the same number of flaps per rotor revolution. The crank radius was altered for each test of a different number of flaps per revolution. It will be shown later that the actual flapping amplitude may have differed from the calculated values due to factors such as part tolerances and inertial effects of the flapping mechanism at high frequencies. Dynamic measurement of the flapping amplitude will be described with the results.

In the remainder of Flotor tests, measurements were taken of average thrust, average rotor torque, flapping motor RPM, rotation motor RPM and rotation motor electrical power. All data were again gathered and averaged with the data acquisition system except for the thrust, which was averaged with the digital balance. Data were gathered during each of the three conditions of conventional rotation, rotation plus flapping, and zero motion. Each data point shown for each test condition is an

average of at least three data samples gathered under the same conditions.

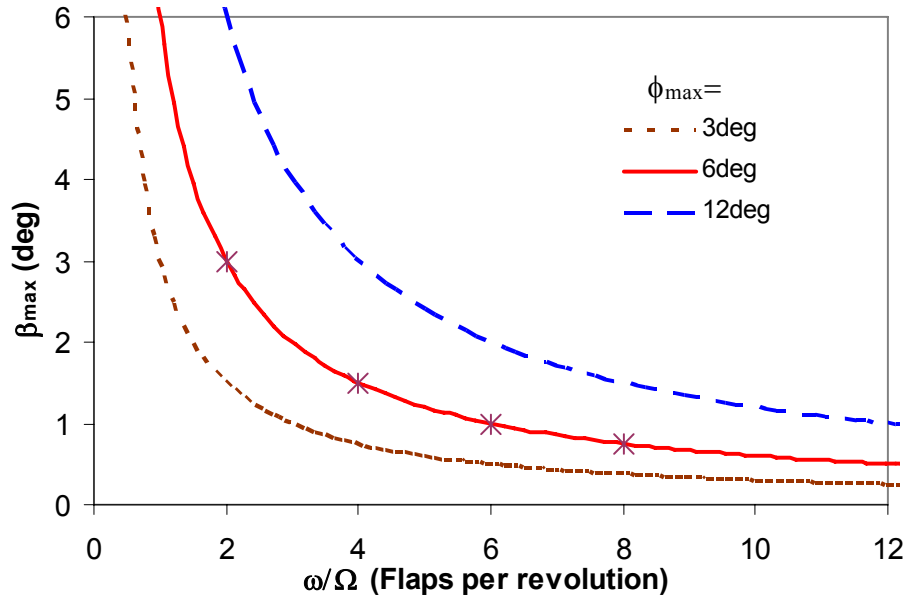


**Figure 64: Flapping amplitude vs. flapping frequency ratio for constant values of angle of incidence**

The data for each RPM is presented in terms of blade loading coefficient versus collective, torque coefficient versus blade loading coefficient, and figure of merit versus blade loading coefficient. The figure of merit is more for informational purposes, since it does not include the power input to the flapping motor. Since the blade loading is directly proportional to the thrust, sometimes a change in blade loading coefficient will be described as a change in thrust. Similarly, a change in torque coefficient is sometimes referred to as a change in torque.

In the three samples of the same test condition, the standard deviation is typically 1% for thrust, 3% for torque and 2% for RPM. These errors will propagate to an expected error of approximately 4% in thrust coefficient and 7% in power coefficient, both of which are used in the calculation of figure of merit. The figure of

merit will have an expected error of approximately 8%, which is the reason the figure of merit data had the most scatter. The following data was previously presented by Fitchett and Chopra [63], with the exception of the tests at 1000 RPM with 6 per revolution flapping and 660 RPM with 8 per revolution flapping.

The first test incorporated 2/rev flapping frequency at an amplitude of  $3^\circ$ . The blades were rotated at 660 and 1000 RPM over a range of blade collectives. The reduced frequency at the  $\frac{3}{4}$  blade span during flapping and rotation was approximately 0.15. The data with flapping and without flapping has been plotted simultaneously with different symbols. The 660 RPM data for this test is shown in Figure 65 and the 1000 RPM data is shown in Figure 66. The blade loading coefficient for 660 RPM reaches a maximum of 0.21 at  $30^\circ$  collective with no difference between the flapping and non-flapping case. The blade loading coefficient in the 1000 RPM case reaches a maximum of 0.22 at  $32^\circ$  collective for both the flapping and non flapping case. At high collective angles of  $34^\circ$  and  $36^\circ$ , the 1000 RPM 2/rev flapping case shows an increase in thrust of about 5% compared to the non-flapping case, but this does not reach beyond the maximum thrust of either case.

The torque coefficients for 660 and 1000 RPM with steady rotation are within 5% of each other at every collective angle. The only differences occur with flapping at high collectives. Even though the 1000 RPM case achieves slightly increased thrust with flapping at the two highest collective angles, the torque at those points is almost identical to the torque without flapping. For flapping and steady rotation, the figure of merit reaches a maximum of 0.46 at 1000 RPM and 0.43 at 660 RPM. In general, there is no appreciable difference or benefit due to 2/rev blade flapping.

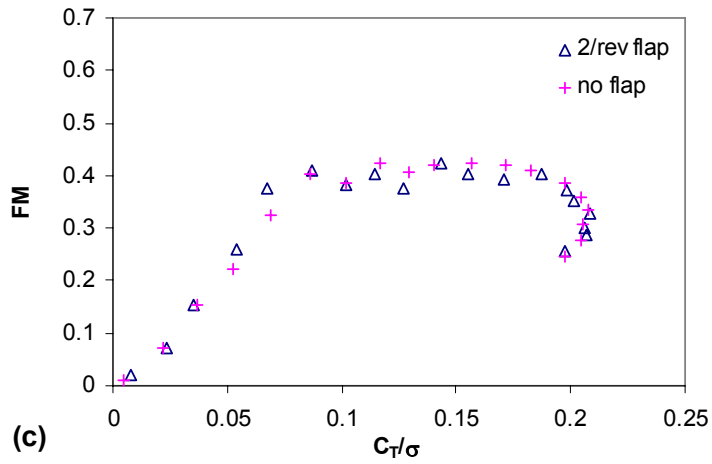
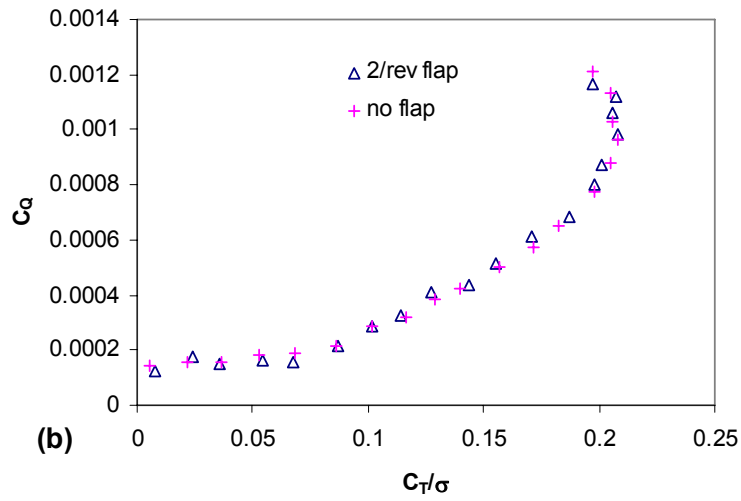
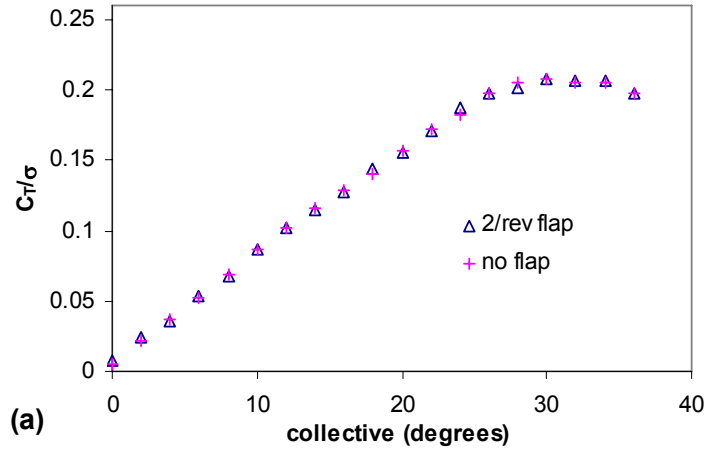


**Figure 65: 660 RPM 2/rev flap results**  
 (a)  $C_T/\sigma$  vs. collective, (b)  $C_Q$  vs.  $C_T/\sigma$  (c) FM vs.  $C_T/\sigma$

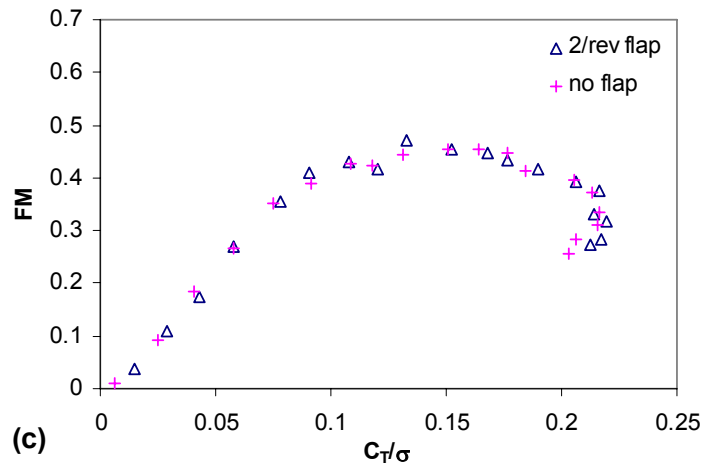
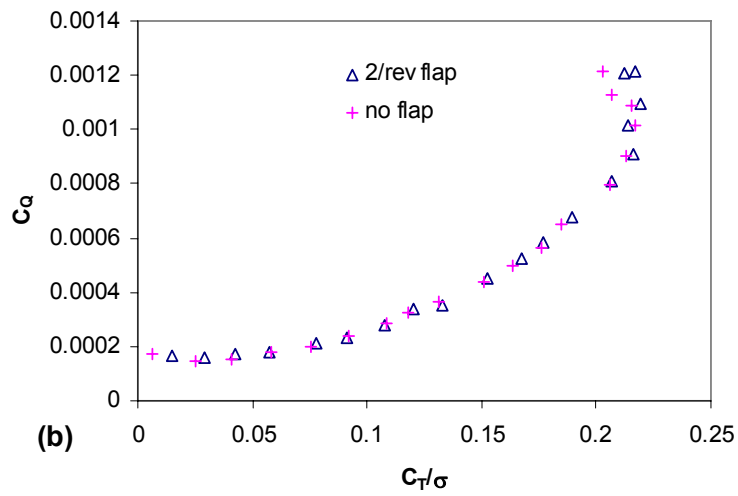
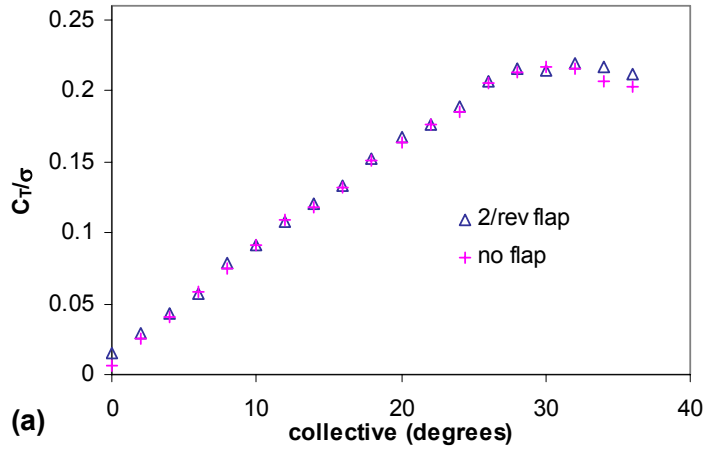


**Figure 66: 1000 RPM 2/rev flap results**  
**(a)  $C_T/\sigma$  vs. collective, (b)  $C_Q$  vs.  $C_T/\sigma$  (c) FM vs.  $C_T/\sigma$**

The next test was conducted with the same rotational speeds, but the flapping frequency was increased to 4/rev at an amplitude of  $1.5^\circ$ . During blade flapping, the reduced frequency was 0.3 at  $\frac{3}{4}$  rotor radius. The 660 RPM data are shown in Figure 67 and the 1000 RPM data are shown in Figure 68. Above  $26^\circ$  collective and below  $8^\circ$  collective, there was an increase in thrust with 4/rev flapping. With flapping, the maximum thrust increased by 6% at 660 RPM and  $32^\circ$  collective and similarly by 5% at 1000 RPM and  $30^\circ$  collective. Beginning to show here is evidence of delayed stall at collective angles above  $24^\circ$ . During the cases with 4/rev flapping, the blades were actually stalling at slightly higher collective angles than in the cases without flapping. The linear slope of the thrust versus collective plot extends to collective angles about  $4^\circ$  higher.

The increased maximum figure of merit for the 4/rev flapping cases is not only attributed to the increased thrust, but also to the reduction of torque necessary to spin the rotor. With flapping, the torque was reduced by 10% when operating at maximum FM, which occurred at a  $C_T/\sigma$  between 0.1 and 0.15. At moderate collectives, the torque reduction was evidence that the blades were producing some of their own force in the direction of rotation. At collective angles above  $30^\circ$ , the torque during flapping increased by 4 - 6%, showing signs of increased drag on the blades. Okamoto and Azuma [37] also measured similar drag increases during dynamic stall of heaving wings at similar Reynolds number and reduced frequency.

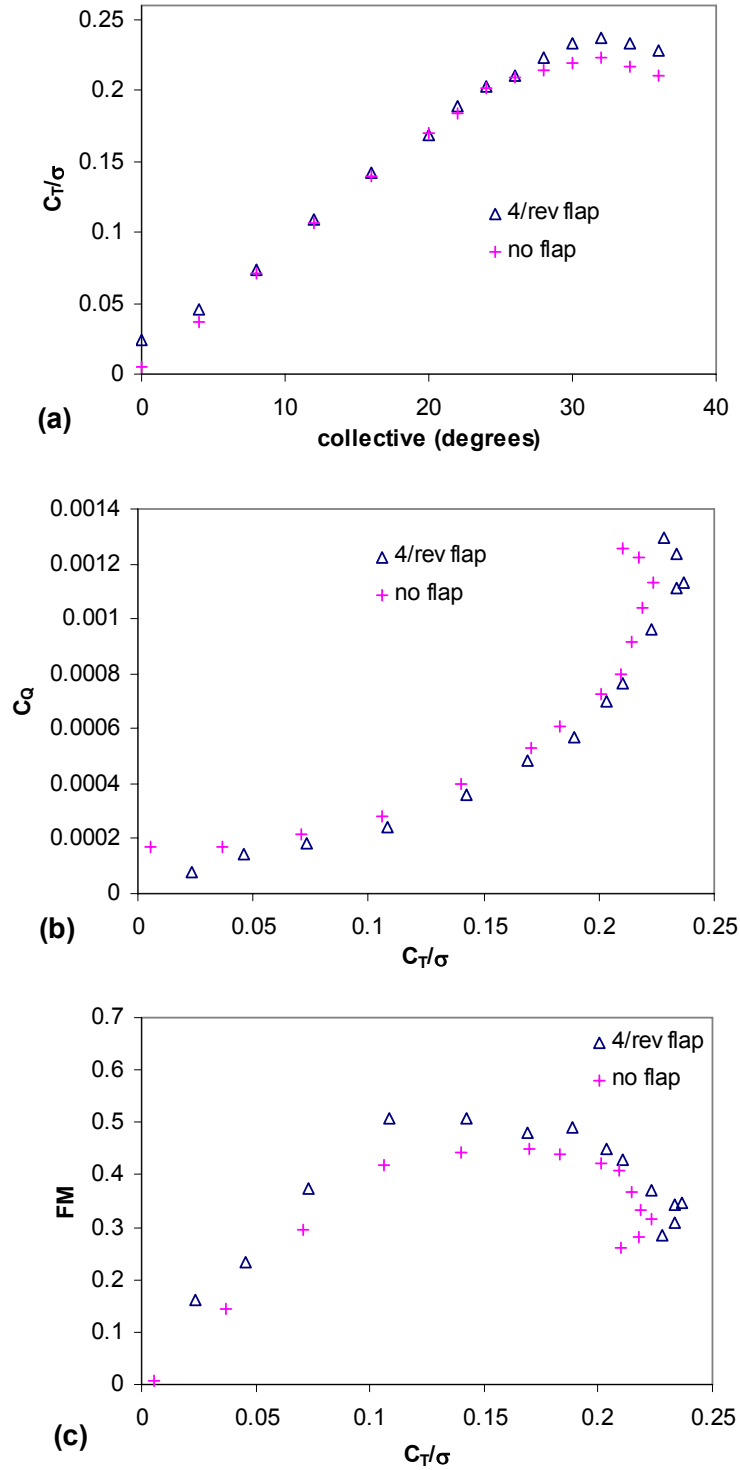


**Figure 67: 660 RPM 4/rev flap results**  
**(a)  $C_T/\sigma$  vs. collective, (b)  $C_Q$  vs.  $C_T/\sigma$  (c) FM vs.  $C_T/\sigma$**

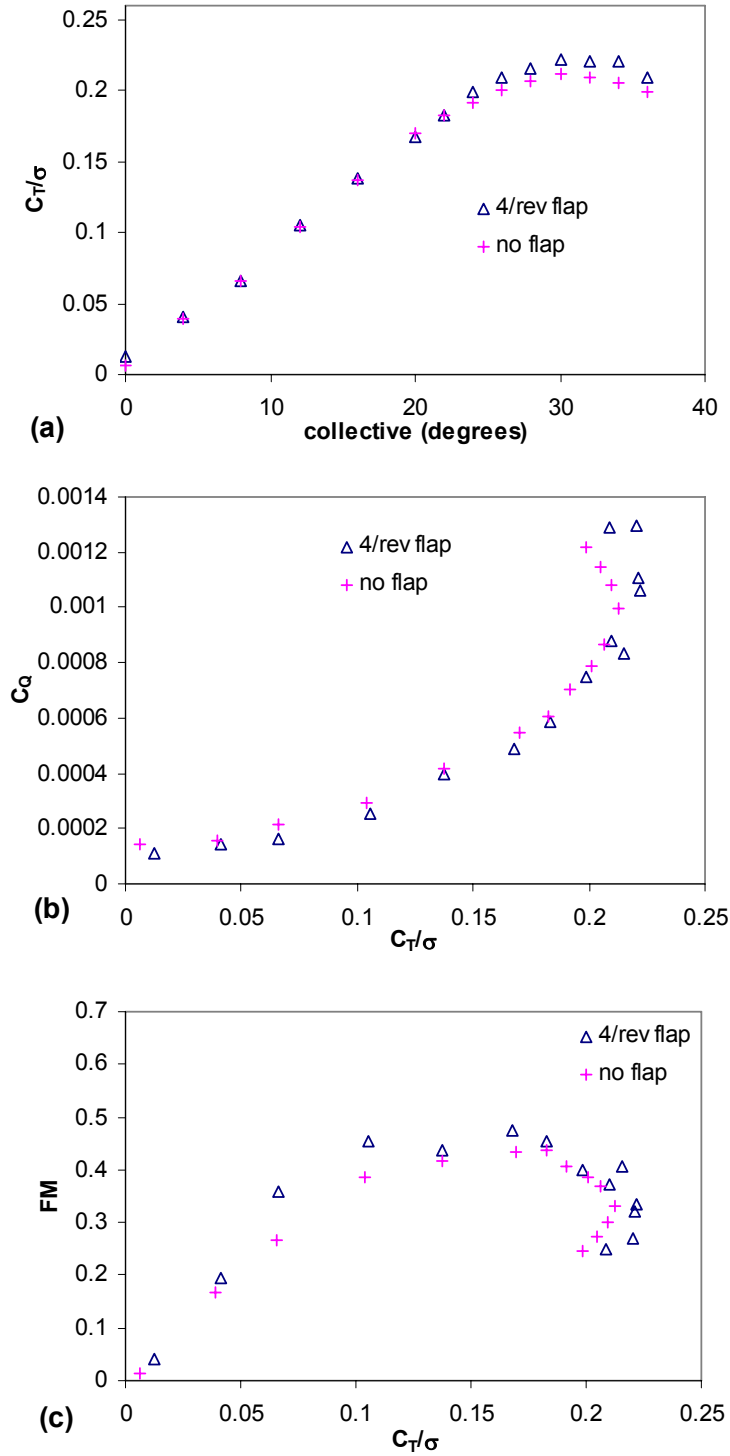


**Figure 68: 1000 RPM 4/rev flap results**  
 (a)  $C_T/\sigma$  vs. collective, (b)  $C_Q$  vs.  $C_T/\sigma$  (c) FM vs.  $C_T/\sigma$

The next test was conducted at 660 RPM with 6/rev flapping at a target flapping amplitude of  $1^\circ$ . It should be noted that the actual flapping amplitude was nearly  $2^\circ$  during this test due to tolerances in the flapping mechanism. Reasons for the discrepancy and a method for measuring flapping angle will be explained in detail after all of the results are presented. Nonetheless, the 6/rev reduced frequency met the goal of 0.45 since it does not depend on flapping amplitude. The data for this test are in Figure 69.

The thrust coefficient at all collectives increased with 6/rev flapping compared with conventional rotation. In this case, it is apparent that delayed stall was occurring, which allowed the rotor with 6/rev flapping to achieve average maximum thrust coefficients 15% higher than conventional rotation at  $30^\circ$  collective. The flapping blades were again producing a force in the direction of rotation, evidenced by an obvious reduction in the shaft torque below  $30^\circ$  collective. With 6/rev flapping, the torque was reduced by at least 30% at collective angles less than  $16^\circ$  and the torque was reduced by 10% while the rotor operated at maximum figure of merit. Torque was equal to the conventional rotation case when operating at maximum thrust. The torque data with 6/rev flapping showed a 3% increase at collective angles above  $30^\circ$ .

The next results in Figure 70 are from the test with 1000 RPM rotation and 6/rev blade flapping at a target amplitude of  $1^\circ$ . The reduced frequency was 0.45 at  $\frac{3}{4}$  rotor radius. The error of flapping amplitude in this case was within 30%, which is much improved compared to previous test. The data again show an increase in thrust with flapping at collectives below  $8^\circ$ . At  $0^\circ$  collective, the blade loading coefficient

with flapping is 0.026 compared to 0.007 with conventional rotation.

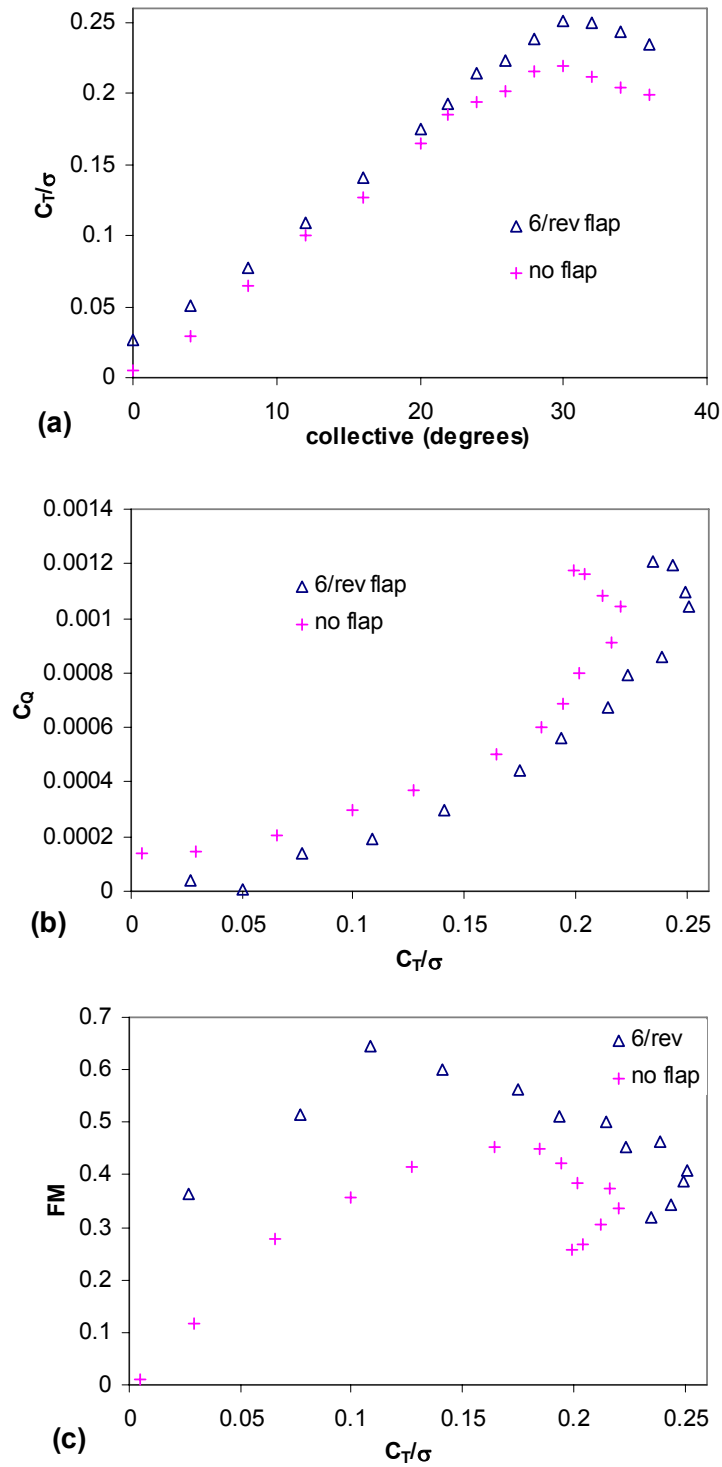


**Figure 69: 660 RPM 6/rev flap results**  
**(a)  $C_T/\sigma$  vs. collective, (b)  $C_Q$  vs.  $C_T/\sigma$  (c) FM vs.  $C_T/\sigma$**

The thrust data again also shows evidence of dynamic stall occurring at collective angles above 24°. With flapping, the linear slope of the blade loading coefficient data extends 4-6° higher than conventional rotation before the thrust data show signs of blade stall. The maximum blade loading coefficient with steady rotation is 0.216 at 30° collective. With flapping, the maximum blade loading coefficient increases by 13% to 0.243 at 34° and 36° collective.

The torque data shows obvious effects of delayed stall at high collective angles. With 6/rev flapping above 28° collective, the torque shows an 8% to 13% increase compared to conventional rotation. The torque decrease at lower collective angles in this test was not as significant as was seen in the previous test of higher amplitude 6/rev flapping. The decrease in torque in the previous tests at moderate collectives seems more dependent on flapping amplitude than it is on flapping frequency. Some of this phenomenon can be explained quasi-steadily. On a blade element at radius  $y$ , the lift vector  $dL$  tilts forward by the angle of incidence  $\phi$  during the downstroke and the upstroke, producing a blade element “anti-torque” of  $ydL\sin\phi$ . If the angle of incidence is increased by increasing the flapping amplitude, then the lift vector will produce greater anti torque. According to the data, this quasi-steady explanation is either only valid at higher absolute flapping amplitudes or it starts becoming invalid at high flapping frequencies.

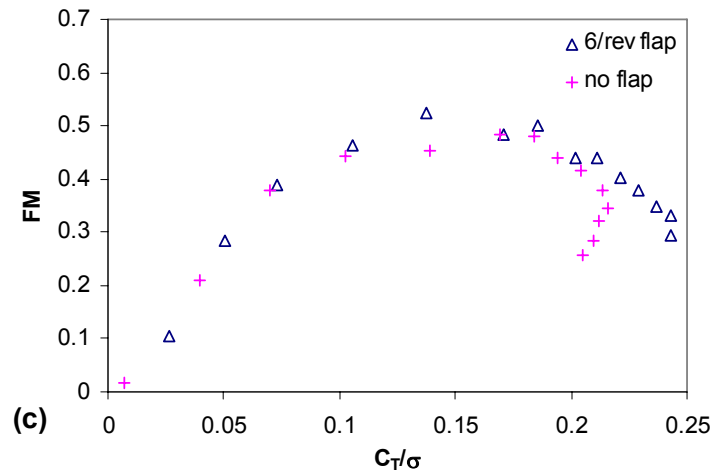
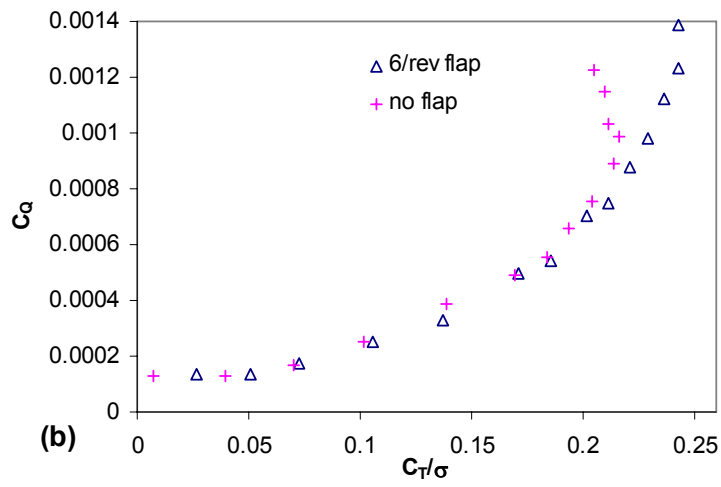
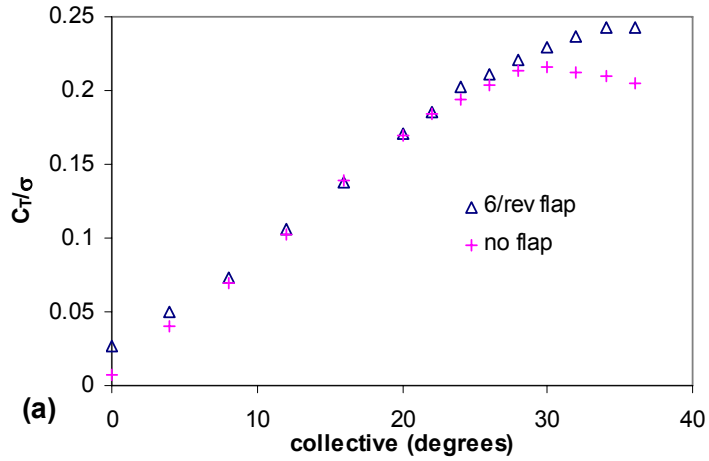


**Figure 70: 1000 RPM 6/rev flap results**  
 (a)  $C_T/\sigma$  vs. collective, (b)  $C_Q$  vs.  $C_T/\sigma$  (c) FM vs.  $C_T/\sigma$

The final test completed in this series of rigid blade tests involved rotation at 660 RPM and blade flapping at 8 per revolution. The reduced frequency was 0.6 at  $\frac{3}{4}$  blade span. The flapping magnitude target was  $0.75^\circ$ , which was found to be smaller than the minimum possible flapping amplitude of the Flotor at this frequency. The minimum flapping amplitude at high frequencies is apparently limited by the tolerances and backlash of the components. The actual flapping amplitude was slightly greater than  $1^\circ$ , which was achieved with a flapping motor crank radius of  $0.007'' \pm 0.001''$ . The test results are shown in Figure 71.

The data below  $8^\circ$  collective with 8/rev flapping again shows an increase in thrust compared to conventional rotation, but it is much less obvious than the previous 4/rev or 6/rev tests. At  $0^\circ$  collective, the blade loading coefficient with flapping is 0.015 compared to the steady rotation value of 0.010. The thrust increase at high collective angles is more familiar. With 8/rev flapping, the maximum blade loading coefficient is 0.240 at  $34^\circ$  collective, which is a 13% increase compared to the conventional rotation value of 0.213 at  $30^\circ$  collective. The torque at low thrust values with flapping again shows a slight decrease compared to conventional rotation. The torque at high thrust values again shows evidence of dynamic stall. With flapping, the torque values at  $32^\circ$ ,  $34^\circ$ , and  $36^\circ$  collective increase by 5%, 10%, and 15%, respectively, compared to conventional rotation.

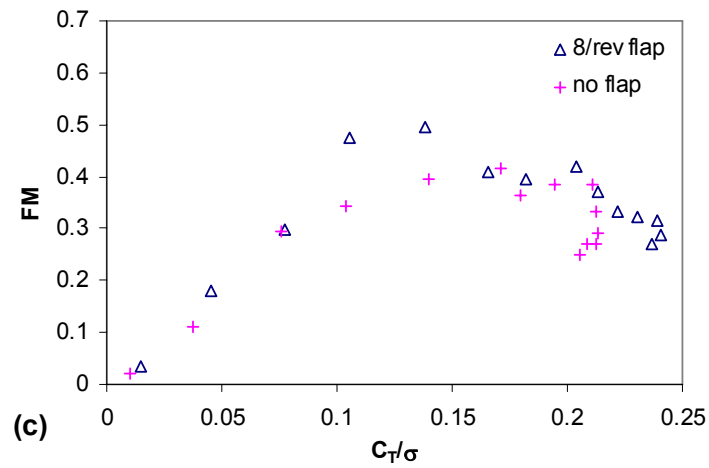
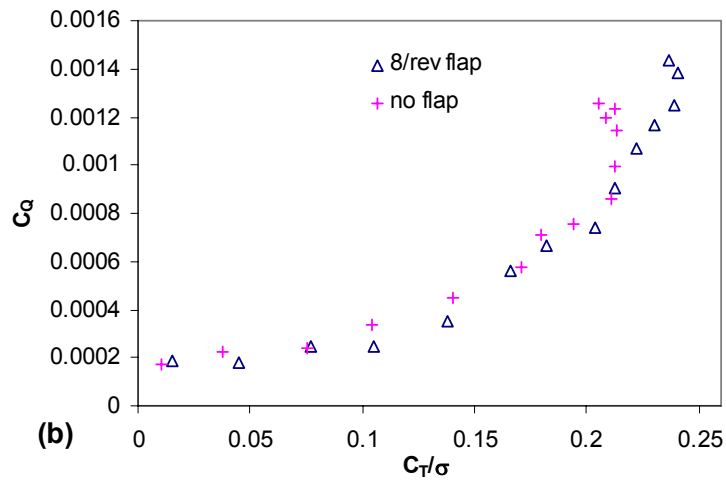
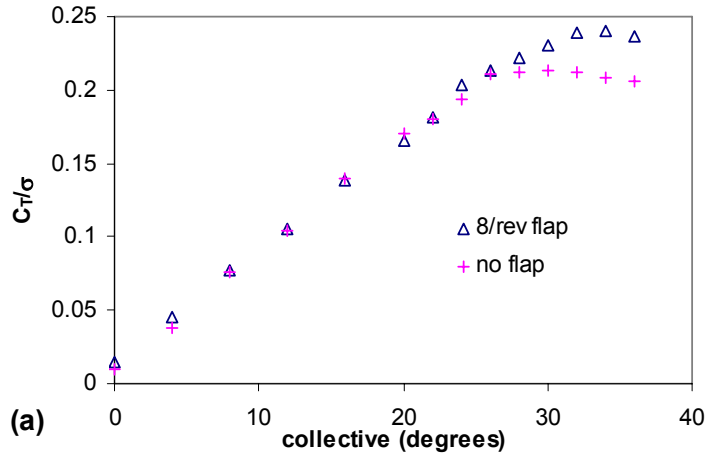


**Figure 71: 660 RPM 8/rev flap results**  
 (a)  $C_T/\sigma$  vs. collective, (b)  $C_Q$  vs.  $C_T/\sigma$  (c) FM vs.  $C_T/\sigma$

In the flapping results, especially at 6/rev, an interesting thrust increase occurs near  $0^\circ$  collective. In Figure 69(a), at  $0^\circ$  collective, the rotor produced a blade loading coefficient with 6/rev flapping of .027 compared to .005 without flapping. In Figure 70(a), at  $0^\circ$  collective, the rotor produced a blade loading coefficient with 6/rev flapping of .025 compared to .007 without flapping. This thrust increase was also apparent in the 4/rev tests, albeit not as much. It can be explained by purely steady phenomena due to the variation of lift and drag vectors with angle of attack. Recalling the lift and drag curves of a cambered plate airfoil from Figure 33, the lift curve slope is 9 times greater above  $-4^\circ$  angle of attack than below. The drag increases faster at positive angles of attack compared with negative angles of attack. For the purpose of this example, assume that a blade section is at  $0^\circ$  collective and undergoes an angle of attack variation of  $\pm 10^\circ$  due to flapping. A detailed view of this portion of the lift and drag curves is in Figure 72 along with the maximum values of lift and drag coefficient due to  $10^\circ$  angle of attack variation.

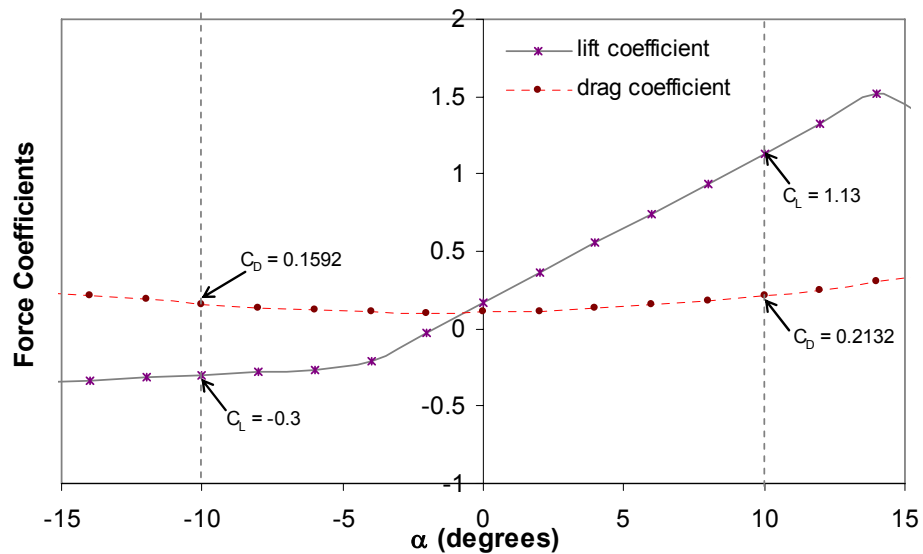


**Figure 72: Lift and drag vs. angle of attack for cambered plate including maximum and minimum values for  $\pm 10^\circ$   $\alpha$  variation**

When the blade is flapping downwards, the angle of attack reaches a maximum of  $10^\circ$  and the drag coefficient reaches a maximum of 0.213. The drag vector on the downstroke contributes to the vertical force of the rotor, as shown previously in Figure 34. The portion of the drag coefficient acting upwards during downward flapping is  $0.213 \sin 10^\circ = 0.037$  and the vertical portion of drag during upward flapping is  $0.159 \sin(-10^\circ) = -0.028$ . Since the drag curve is not symmetric about  $0^\circ$  angle of attack, the drag averages to a net upward force coefficient of 0.0045 while flapping at  $0^\circ$  collective.

The vertical component of lift coefficient during downward flapping is  $1.13 \cos(10^\circ) = 1.11$  and during upward flapping is  $-0.3 \cos(-10^\circ) = -0.295$ . Also because the lift curve is not symmetric about  $0^\circ$  angle of attack, the lift produces a net force upwards during blade flapping. The lift will produce an average vertical force coefficient of 0.41 during flapping, which is more than double the steady lift coefficient of 0.17 at  $0^\circ$  angle of attack. The difference in thrust seen while flapping at low collective angles is a quasi-steady effect that is primarily due to the properties of the asymmetric lift curve slope of highly cambered blades and secondarily due to the vertical contribution of the drag.

As mentioned earlier, the results for 660 RPM 6/rev flapping were drastically different from the previous 4/rev results because the blade flapping amplitude goal was being overshoot. The backlash and tolerances of the parts were allowing the inertia of the blades to carry them to greater angles than intended. The tolerances of the parts were within 0.001" and the bearings in the load path are ABEC-5 rated. At

higher flapping frequencies, however, the driving pin in the flapping motor flywheel is offset by less than 0.01", which means there is at least 10% error built into the flapping mechanism. The backlash error percentage increases as the flapping amplitude decreases.

The motion of the test setup was experimentally investigated further and corrected after the 660 RPM 6/rev test. Prior to this point, the flapping amplitude was measured by slowly rotating the flapping motor and taking measurements of the blade angle at its peak values, which is equivalent to measuring the angles at very low flapping frequencies. In order to measure the flapping at higher target frequencies, the motion was photographically analyzed. A Canon A530 digital camera was utilized in extended exposure mode to capture the flapping amplitude at high frequencies. The camera was secured on a level surface at the same height as the rotor plane and the shutter was set to open for at least two seconds to capture the maximum peak to peak blade flapping amplitude. The photographs were then analyzed graphically with Engauge Digitizer, which allows accurate digital measurement of photographic data or other images [64]. Figure 73 is a photo of the Flotor flapping at about 60 Hz with a target amplitude of 2° peak to peak. The actual measured peak to peak amplitude in this photo is closer to 5°. It was found that, at the 2 and 4/rev flapping frequencies, the flapping amplitude was reaching its targets within 30%, but the 6/rev flapping frequency was more than doubling the target amplitude. This large uncertainty with the current mechanism was difficult to avoid due to the tolerances already described. For the remainder of the tests, this overshoot was corrected by reducing the crank radius of the offset pin on the flywheel

accordingly. By the final test, the pin was offset by only 0.007”.



**Figure 73: Flotor blade with 5° peak to peak flapping**

To demonstrate the full effects of unsteady aerodynamics on the average rotor forces, the analytical BEMT model is again employed. The model calculates the purely steady aerodynamic forces, so it can be used to observe which phenomena in the experiment are due to quasi-steady, two dimensional effects. The thrust data for the quasi-steady model are shown in Figure 74.

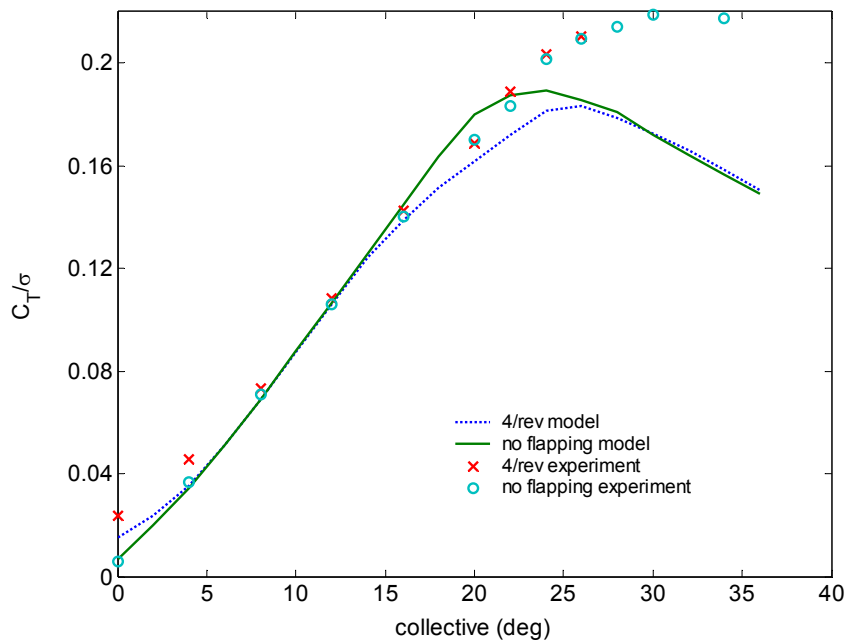


**Figure 74:  $C_T/\sigma$  vs. collective (quasi steady prediction for 4/rev flapping)**

The quasi-steady model predicts the increase in thrust coefficient at collective angles below  $5^\circ$ . At  $0^\circ$  collective, the model predicts that the blade loading coefficient during flapping will be 0.015 compared with 0.007 for steady rotation. Experimental results showed blade loading coefficients of about 0.25 with 6/rev flapping at  $0^\circ$  collective. This phenomena is predicted by steady aerodynamics. According to the quasi-steady model, the increased thrust at  $0^\circ$  collective will increase with increasing flapping amplitude. The quasi-steady prediction does not predict well the thrust of the flapping rotor above  $15^\circ$  collective angle. The variation of angle of attack is bringing the quasi-steady model beyond stall, so the average lift decreases. This is where the unsteady effects are seen most in the experimental data. If it were not for delayed stall above  $15^\circ$  collective, the thrust with 4/rev flapping would actually be decreased compared to conventional rotation.

The quasi steady model of torque versus collective is shown in Figure 75. The features of the torque prediction at low to moderate collective angles match very well with the experimental data trends. At collectives below  $5^\circ$  with 4/rev flapping, there is less torque required than conventional rotation. At collectives between  $5^\circ$  and  $15^\circ$  with 4/rev flapping, there is less torque required to produce the same amount of thrust as conventional rotation. Above  $25^\circ$ , the quasi-steady model predicts the same amount of torque with less thrust for the 4/rev flapping case. The experimental data, however, shows more torque and more thrust at the highest collective angles with flapping. The quasi-steady prediction is adequate, except at high collectives with high frequency flapping. This is the region where the unsteady effects dominate the

forces on the rotor.

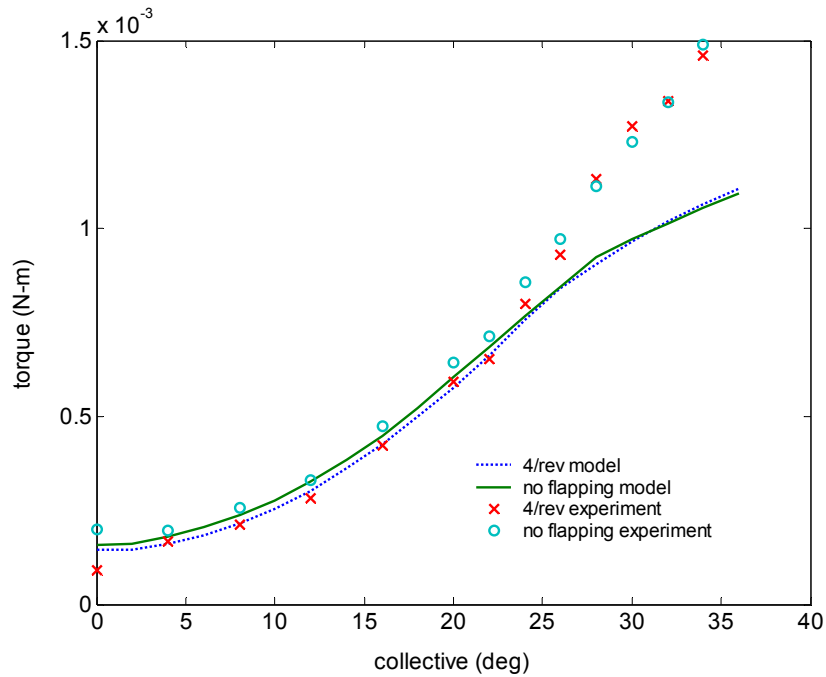


**Figure 75: Torque vs. collective (quasi-steady prediction for 4/rev flapping)**

## 5 Summary and Concluding Remarks

The goal of this study was to introduce and examine the effects of biologically inspired motion on current hover capable technology. After studying the methods used by nature for efficient flight, avian based kinematics were emulated into a simple flapping motion that could be applied to a current MAV rotor. It was hypothesized and proven that this combination of rotary and flapping motion could provide hover capable thrust without the necessity for powered shaft rotation. This thesis described the design, fabrication and testing of a hover capable micro air vehicle rotor capable of being powered only by avian based blade flapping.

## 5.1 Contributions and Conclusions

The Flotor research test bed was designed and manufactured for conventional and innovative flapping MAV rotor experiments. This experience demonstrated the importance of careful part and assembly design. Design iterations were more quickly performed on a 3-D computer model so that only one complete hardware assembly was constructed. A digital 3-D catalog of each part of the assembly is available to be used by any interested researcher. The Flotor was capable of operating in each of its three hover capable motions: powered blade flapping with passive (unpowered) hub rotation, conventional powered rotation, and powered rotation with powered flapping. A blade element momentum analysis was conducted for the cases of powered rotation with and without blade flapping.

### 5.1.1 Flapping blades with passive hub rotation

The first tests of the Flotor proved that flexible blades with avian based blade flapping could cause the blades to rotate with zero torque input to the rotor shaft. These were perhaps the first experiments of a torqueless MAV flapping rotor with no motor to power the rotor shaft. The first tests were conducted with two sets of flexible blades, one of which emulated the shape a bat's wings. The results from those tests of flapping with passive rotation led to the following conclusions:

1. The hub rotation speed increased at a greater rate than the blade flapping frequency. The hub rotation reached the fastest steady values at collective angles of  $15^{\circ}$ - $20^{\circ}$ .
2. At positive collective angles, both the blade flapping and the hub rotation

contributed to the vertical thrust. The fraction of the thrust attributed to blade flapping grew with increased collective angle and increased blade flapping frequency. The greatest thrust was a certain combination of translational lift due to hub rotation plus vertical force from flexible blade flapping at a high collective angle.

3. Maximum thrusts and blade loadings of  $10 \text{ N/m}^2$  were close to those of similarly sized flying creatures, but they are far below the values for current MAVs.

### 5.1.2 Conventional rotation

The second set of experiments reinforced the limited data available for conventional MAV rotor performance. It also compared aerodynamic efficiency with total propulsion system efficiency in terms of ideal aerodynamic power and actual electrical power. The Flotor was tested with conventional powered shaft rotation and two sets of cambered plate blades, one with a sharpened leading edge. The conventional rotation data was used to verify a BEMT analysis. Prandtl tip losses and a swirl velocity derived from conventional propeller theory were both incorporated into the BEMT model. The following observations were apparent:

1. The operating conditions for maximum aerodynamic efficiency are not the same as the conditions for maximum propulsion system efficiency. The maximum system efficiency occurred at higher collectives and thrust levels than those for maximum aerodynamic efficiency. Matching the propulsion system to the rotor is more important than the maximum efficiency of either

component.

2. Limited to a maximum electrical power, the system's maximum thrust remained relatively constant between  $10^\circ$  and  $20^\circ$  collective angle. The maximum thrust at  $20^\circ$  collective required lower tip speeds and was objectively quieter than at  $10^\circ$  collective at the same maximum thrust.
3. The present experimental rotor data fits very well with previously published data [26]. Because of the lower tip speeds of the current study, there were some detrimental effects of reduced Reynolds number, such as decreased maximum thrust coefficients and a figure of merit that does not exceed 0.5. In the Reynolds number range of 10,000 - 40,000, doubling the Reynolds number made possible an 8% increase in maximum figure of merit.
4. For normal operating conditions below  $21^\circ$  collective, the BEMT analysis predicted the rotor performance and maximum figure of merit very well. Above  $21^\circ$  collective, however, the analysis predicted an earlier rotor stall than shown by the experiments. The experimental rotor achieved higher thrust at higher collective angles than predicted by the BEMT analysis. This observation agreed with previously published comparisons.

### 5.1.3 Powered hub rotation with powered blade flapping

The final set of results was from obtained powered hub rotation plus powered blade flapping. One test was accomplished with flexible flat plate blades flapping at a frequency of 4/rev. Relatively rigid cambered plates were tested over a range of flapping frequencies up to 8 per rotor revolution, or a reduced frequency of 0.6. All

results were simultaneously compared to results of conventional rotation. The BEMT analysis developed earlier was used to explain some features of the results. The results showed the following:

1. The flapping flexible flat plate blades produced a thrust benefit at every collective angle. At high collectives, the flapping blades showed a large benefit, increasing the maximum thrust by 20% due to delayed stall.
2. Benefits of rigid cambered blade flapping at frequencies greater than 2/rev included increased maximum thrust coefficients by up to 15% and decreased torque required at moderate thrust. There was a thrust produced with flapping near  $0^\circ$  collective due to the asymmetric lift and drag curves of the highly cambered blades. The maximum blade loading coefficient of 0.251 for the cambered plate blades with 6/rev flapping was possibly the highest recorded for a rotary wing MAV.
3. At the high flapping amplitudes during 6/rev flapping at collective angles less than  $16^\circ$ , shaft torque was reduced by an average of more than 30%.
4. The quasi-steady BEMT analysis fit the experimental data well below  $15^\circ$  collective, with and without blade flapping. The model accurately predicted a reduced torque with blade flapping at moderate collectives and an increase in thrust at  $0^\circ$  collective. Above  $15^\circ$  collective, however, the model could not predict even the average loads measured in the experiments.

## 5.2 Future Work Recommendations

A conventionally powered rotor implementing an additional actuation source

for blade flapping is too complicated for a flying vehicle. In addition, blade flapping to achieve additional thrust from delayed stall requires high collective angles and impairs rotor efficiency due to the increased shaft torque required. Instead, flexible blade flapping at larger amplitudes should be implemented in order to eliminate the torque required during normal operating conditions.

Modeling of a flapping rotor with BEMT and steady aerodynamics has been adequate for initial modeling of the aerodynamics of this type of motion. A simple elastic blade model should be incorporated to estimate the blade aerodynamic angles. CFD and flow visualization may be necessary to estimate the behavior of the time varying inflow.

To determine feasibility of a torqueless rotor flying vehicle, the aerodynamic performance must first be improved in a number of areas. The flexible blade design used in the torqueless configuration needs to be explored. The blade aerodynamic properties should incorporate twist, camber, anhedral, and taper. They need to be aeroelastically tailored to provide a balance of vertical force for thrust and horizontal force to power the rotation of the rotor. During the downstroke, the blade should provide a large vertical force plus all of the horizontal force necessary to power rotation of the rotor. The beginning of the downstroke may consume the vast majority of the power of the flapping motion. During the upstroke, the blade should harness the momentum of the rotor and utilize airspeed to produce lift. The lift will assist in accelerating the blade upward at the end of the downstroke and beginning of the upstroke. These motions are modeled after a bird in forward flight. The motions and aerodynamics can be examined with the current Flotor test bed.

It has proven almost impossible with the current instruments and configuration to measure instantaneous aerodynamic forces on the blades of the Flotor because reciprocating forces of the moving parts can be orders of magnitude higher than the aerodynamic forces. Different methods for finding the aerodynamic forces should be explored. The aerodynamic forces could be increased and the reciprocating mass forces could be decreased by operating the flotor blades at a slower flapping frequency in a more viscous fluid. The fluid forces would become the dominant forces on the mechanism and the fluid flow could be easily visualized and studied. Possible fluids include water or oil of varying viscosities. Similar methods have been successfully used by many researchers studying insect flapping wing aerodynamics.

Once the aerodynamics and blade structure is optimized, it must then be determined if a flapping rotor system can be designed light enough for a flying vehicle. Powered rotary motion is not necessary for blade flapping, so the idea of a motor comprised of dense copper and ferrous materials should be abandoned. Instead of a system that converts rotary to linear motion as on the current Flotor, a blade flapping mechanism should be designed to operate at resonance. Alternative systems for high frequency periodic actuation should be investigated, such as chemical muscles or smart materials. On this scale, utilizing a lightweight and efficient periodic actuation source coupled with a flapping mechanism operating at resonance should require drastically less power than a conventional electric motor. As size decreases, this type of system may prove more efficient than the conventional scaled down helicopter rotors that are currently utilized for MAVs.

## Bibliography

---

- [1] Seiko Epson Corporation. "Epson Develops World's Smallest Flying Robot", [http://www.epson.co.jp/e/newsroom/news\\_2003\\_11\\_18\\_2.htm](http://www.epson.co.jp/e/newsroom/news_2003_11_18_2.htm) . November 17, 2003.
- [2] BAE Systems. Information and Electronic Warfare Systems. Co-developed by Lockheed Martin. [www.eis.na.baesystems.com/brochures/pdfs/01\\_d49\\_001.pdf](http://www.eis.na.baesystems.com/brochures/pdfs/01_d49_001.pdf)
- [3] Grasmeyer, J.M. and Keennon, M.T., "Development of the Black Widow Micro Air Vehicle", 39<sup>th</sup> AIAA Aerospace Sciences Meeting & Exhibit. Reno, NV. January 2001.
- [4] Bohorquez, F., "Rotor Hover Performance and System Design of an Efficient Coaxial Rotary Wing Micro Air Vehicle", Ph.D. dissertation, directed by Darryll Pines. Dept. of Aerospace Engineering. University of Maryland. College Park, MD. 2007.
- [5] Precision Heli R/C Helicopters. <http://www.precisionheli.com/> 2007.
- [6] Ramasamy, M., Johnson, Bradley, Leishman, J.G., "Toward Understanding the Aerodynamic Efficiency of a Hovering Micro Rotor", American Helicopter Society International Specialists Meeting on Unmanned Rotorcraft. January 23-25, 2007. Chandler, AZ.
- [7] Lipera, L., Colbourne, J.D., Tischler, M.B., Mansur, M.H., Rotkowitz, M.C., Patangui, P., "The Micro Craft iSTAR Micro Air Vehicle: Control System Design and Testing", American Helicopter Society 57<sup>th</sup> Annual Forum. Washington, D.C., May 9-11, 2001.
- [8] Sirohi, J., Tishchenko, M., Chopra I., "Design and Testing of a Micro-Aerial Vehicle with a Single Rotor and Turning Vanes," AHS 61<sup>st</sup> Annual Forum. Grapevine, TX., 1-3 June 2005.
- [9] Hrishikeshavan, V., Sirohi, J., Tishchenko, M., and Chopra, I., "Design and Stability of a Shrouded Rotor Micro Air Vehicle with Anti-torque Vanes". American Helicopter Society International Specialists' Meeting on Unmanned Rotorcraft. Chandler, Arizona, January 2007.
- [10] Gupta, N.K., Copp, P., and Chopra, I., "Development of a Test-bed for Closed-loop MAV Flight Control", American Helicopter Society International Specialists' Meeting on Unmanned Rotorcraft. Chandler, Arizona, January 2007.
- [11] Fleming, J., Jones, T., Gelhausen, P., and Enns, D., "Improving Control System Effectiveness for Ducted fan VTOL UAVs Operating In Crosswinds", 2nd AIAA

---

"Unmanned Unlimited" Systems, Technologies, and Operations—Aerospace. San Diego, California, September 2003.

[12] Keennon, M.T., and Grasmeyer, J.M., "Development of the Black Widow and Microbat MAVs and a Vision of the Future of MAV Design", AIAA/ICAS International Air and Space Symposium and Exposition: The Next 100 Years. July 14-17, 2003. Dayton, Ohio.

[13] Singh, Beerinder and Chopra, Inderjit, "Wing Design and Optimization for a Flapping Wing Micro Air Vehicle", American Helicopter Society 60<sup>th</sup> Annual Forum. Baltimore, MD. June 7-10, 2004.

[14] Kornbluh, R., "Project Mentor: Biologically Inspired Platform", Keynote Presentation. 8th AIAA/CEAS Aeroacoustics Conference, 17–19 June 2002. Breckenridge, CO.

[15] Weis-fogh, T., "Quick Estimates of Flight Fitness in Hovering Animals, Including Novel Mechanisms for Lift Production", *Journal of Experimental Biology*, Vol. 59, No. 1. 1973. pp. 169-230.

[16] Laitone, E.V., "Wind tunnel tests of wings at Reynolds numbers below 70000," *Experiments in Fluids*. Vol. 23, 1997. pp 405-409.

[17] Schmitz, F.W., "Aerodynamics of the Model Airplane. Part I. Airfoil Measurements", 1941. Translation by Redstone Scientific Information Center. Redstone Arsenal, Alabama. 1967. Document ID: 19700029685. Accession ID: 70N39001.

[18] Sunada, S., Yasuda, T., Yasuda, K., and Kawachi, K., "Comparison of Wing Characteristics at an Ultralow Reynolds Number", *Journal of Aircraft*. Vol. 39, No. 2, March-April 2002. pp. 331-338.

[19] Selig M.S., Donovan J.F., Fraser D.B., *Summary of Low Speed Airfoil Data*, Vol. 1-4, Soar Tech Publications, Virginia Beach, VA, 1989-2004.

[20] Mueller, T.J., "Aerodynamic Measurements at Low Reynolds Numbers for Fixed Wing Micro-Air Vehicles", RTO AVT/VKI Special Course on Development and Operation of UAVs for Military and Civil Applications. September 13-17, 1999. VKI, Belgium

[21] Mueller, T.J. and Pelletier, A., "Low Reynolds Number Aerodynamics of Low-Aspect-Ratio, Thin/Flat/Cambered-Plate Wings", *Journal of Aircraft*, Vol. 37, No. 5, September–October 2000. pp. 825-832.

- 
- [22] Pines, D.J. and Bohorquez, F., “Challenges Facing Future Micro-Air-Vehicle Development”, *Journal of Aircraft*, Vol. 43, No. 2, March–April 2006. pp. 290-305.
- [23] Simons, Martin, *Model Aircraft Aerodynamics*, 4<sup>th</sup> Edition. Nexus Special Interests Publishing. 1999.
- [24] One, Adam, “Trainer Design”, <http://adamone.rchomepage.com/design.htm>
- [25] Jones, R.T., *Wing Theory*. Princeton University Press. Princeton, NJ. 1990.
- [26] Hein, B. and Chopra, I., “Hover Performance of a Micro Air Vehicle: Rotors at Low Reynolds Number”, American Helicopter Society International Specialists’ Meeting on Unmanned Rotorcraft. Jan. 18-20, 2005. Chandler, AZ.
- [27] Ellington, C. P., VandenBerg, C., Willmott, A. P. and Thomas, A. L. R., “Leading-edge Vortices in Insect Flight”, *Nature*, 1996, vol. 384, pp. 626-630.
- [28] Ellington, C.P., “The Aerodynamics of Hovering Insect Flight”, *Philosophical Transactions of the Royal Society of London Series B*, Vol. 305, No. 1122, Feb. 1984. pp. 1-181.
- [29] Dickinson, M. H. and Götz, K. G., “The Wake Dynamics and Flight Forces of the Fruit Fly *Drosophila Melanogaster*”, *Journal of Experimental Biology*, 1996. vol. 199. pp. 2085-2104.
- [30] Fry, S.N., Sayaman, R., and Dickinson, M.H., “The Aerodynamics of Hovering Flight in *Drosophila*”, *Journal of Experimental Biology*. 2005. Vol. 208. pp. 2303-2318.
- [31] Birch, J.M., Dickinson, W.B., and Dickinson, M.H., “Force Production and Flow Structure of the Leading Edge Vortex on Flapping Wings at High and Low Reynolds Numbers”, *The Journal of Experimental Biology*. 2004. Vol. 207. pp. 1063-1072.
- [32] Singh, B., Ramasamy, M., Chopra, I., Leishman, G.J., “Insect-Based Flapping Wings for Micro Hovering Air Vehicles: Experimental Investigations”, American Helicopter Society International Specialists Meeting on Unmanned Rotorcraft. Chandler, Arizona. January, 2005.
- [33] Ellington, C. P. and Usherwood, J. R., “Lift and Drag Characteristics of Rotary and Flapping Wings,” *Fixed and Flapping Wing Aerodynamics for Micro Air Vehicle Applications*, edited by T. J. Mueller. AIAA Progress in Aeronautics and Astronautics Vol. 195. AIAA. Reston, VA. 2001. pp. 231–248.

- 
- [34] Usherwood, J.R. and Ellington, C.P., “The Aerodynamics of Revolving Wings I. Model Hawkmoth Wings”, *Journal of Experimental Biology*. 2002. Vol. 205. pp. 1547-1564.
- [35] Usherwood, J.R. and Ellington, C.P., “The Aerodynamics of Revolving Wings II. Propeller Force Coefficients From Mayfly to Quail”, *Journal of Experimental Biology*. 2002. Vol. 205. pp. 1565-1576.
- [36] Altshuler, D.L., Dudley, Robert, and Ellington, C.P., “Aerodynamic Forces of Revolving Hummingbird Wings and Wing Models”, *Journal of Zoology*. 2004. Vol. 264, pp. 327-332.
- [37] Okamoto, M. and Azuma, A., “Experimental Study on Aerodynamic Characteristics of Unsteady Wings at Low Reynolds Number”, *AIAA Journal*, Vol. 43, No. 12. Dec. 2005. pp. 2526-2536.
- [38] Knoller, R., “Die Gesetze des Luftwiderstandes”, *Flug- und Motortechnik (Wien)*. 1909. Vol 3, No. 21. pp. 1–7.
- [39] Betz, A., “Ein Beitrag zur Erklärung des Segelfluges”, *Zeitschrift für Flugtechnik und Motorluftschiffahrt*, 1912. Vol. 3, pp. 269–272.
- [40] Katzmayr, R. “Effect of Periodic Changes in Angle of Attack on Behavior of Airfoils”, NACA Technical Memorandum #147. 1922.
- [41] Kellogg, J., Bovais, C., Foch, R., Cylinder, D., Ramamurti, W.S., Gardener, J., Srull, D., Piper, G., Vaiana, P., Kahn, A., “Development and Testing of Unconventional Micro Air Vehicle Configurations”, AIAA Unmanned Unlimited Systems, Technologies, and Operations. 15-18 September, 2003. San Diego, CA.
- [42] Van Holten, T., Heiligers, M., van de Waal, G.J., “The Ornicopter: A Single Rotor Without Reaction Torque, Basic Principles”, 24<sup>th</sup> International Congress of the Aeronautical Sciences. 29 August – 3 September, 2004. Yokohama, Japan.
- [43] Bohorquez, F. and Pines, D.J., “Design and Development of a Biomimetic Device for Micro Air Vehicles”, 9<sup>th</sup> Annual SPIE Smart Materials and Structures Symposium. March 17-21, 2002. San Diego, CA.
- [44] Norberg, U.M., “Allometry of Bat Wings and Legs and Comparison with Bird Wings”, *Philosophical Transactions of the Royal Society of London. Series B, Biological Sciences*. Vol. 292, No. 1061, June, 1981. pp. 359-398.
- [45] Norberg, U.M., *Vertebrate Flight: mechanics, physiology, morphology, ecology and evolution*. Springer. New York. 1990.

- 
- [46] Shyy, Wei, Berg, Mats, and Ljungqvist, Daniel, “Flapping and flexible wings for biological and micro air vehicles”, *Progress in Aerospace Sciences*, Vol. 35, 1999. pp. 455-505.
- [47] Rayner, J.M.V., “A new approach to animal flight mechanics”, *Journal of Experimental Biology*, Vol. 80, 1979. pp. 17-54.
- [48] Greenewalt, C.H., “Dimensional Relationships for Flying Animals”, *Smithsonian Miscellaneous Collection*, Vol. 144, 1962. pp. 1-46.
- [49] Greenewalt, C.H., “The Flight of Birds: The Significant Dimensions, Their Departure from the Requirements for Dimensional Similarity, and the Effect on Flight Aerodynamics of That Departure”, *Transactions of the American Philosophical Society*, New Ser., Vol. 65, No. 4. 1975. pp. 1-67.
- [50] Davis, R. and Cockrum, E., “Experimentally determined weight lifting capacity in individuals of five species of bats”, *Journal of Mammalogy*, Vol. 45, 1964. pp. 643-644.
- [51] Pennycuik, C.J., “Mechanical constraints on the evolution of flight”, *Memoirs of the California Academy of Sciences*, Vol. 8, 1986. pp. 83 - 98.
- [52] Rayner, J.M.V., “Form and function in avian flight”. *Current Ornithology*, Vol. 5, 1988. pp. 1-66.
- [53] Leishman, G.J., *Principles of Helicopter Aerodynamics*, Cambridge University Press, New York. 2000.
- [54] Spedding, G.R., Rosen, M., Hedenström, A., “A family of vortex wakes generated by a thrush nightingale in free flight in a wind tunnel over its entire natural range of flight speeds”, *The Journal of Experimental Biology*, Vol. 206, 2003. pp. 2313-2344
- [55] Perkins, N.C. and Dowling, D.R., “ME 240: Introduction to Dynamics and Vibrations”. [http://www.engin.umich.edu/class/me240/Matlab/Piston/p3\\_175.html](http://www.engin.umich.edu/class/me240/Matlab/Piston/p3_175.html) University of Michigan. 2000.
- [56] Johnson, Wayne, *Helicopter Theory*, Dover Publications, New York. 1994.
- [57] Glauert, H., *The Elements of Aerofoil and Airscrew Theory (Cambridge Science Classics)*, Second Edition, Cambridge University Press. 1983.

- 
- [58] Auld, D.J. and Srinivas, K., “Aerodynamics for Students: Part 6. Propulsion”, <http://www.aeromech.usyd.edu.au/aero/propeller/index.html>. The University of Sydney. Australia. 1995.
- [59] Betz, A. and Prandtl, L., “Schraubenpropeller mit geringstem Energieverlust”, *Nachr. Ges. Wiss. Göttingen* 1919. pp. 193 -213.
- [60] Goldstein, L. “On the Vortex theory of Screw Propellers”, *Proc of the Royal Soc.*, Series A 123. p. 440.
- [61] Lock, C.N.H., “The Application of Goldstein’s Theory to the Practical Design of Airscrews”, British Aeronautical Research Council R&M No. 1377. 1930.
- [62] Faulhaber Group. DC Micromotor and Precision Gearhead data sheets. [www.micromo.com](http://www.micromo.com)
- [63] Fitchett, Brandon, and Chopra, Inderjit, “A Biologically Inspired Flapping Rotor for Micro Air Vehicles”, AHS International Specialists’ Meeting on Unmanned Rotorcraft. 23-25 January, 2007. Chandler, Arizona.
- [64] Mitchell, Mark, *Engauge Digitizer* software. <http://digitizer.sourceforge.net/>